THE APPLICATION OF INTERFEROMETRIC ELECTRON MICROSCOPY FOR NANOMAGNETIC IMAGING

by

ALICE T. GREENBERG

A DISSERTATION

Presented to the Department of Physics
and the Graduate School of the University of Oregon
in partial fulfillment of the requirements
for the degree of
Doctor of Philosophy

December 2020

DISSERTATION APPROVAL PAGE

Student: Alice T. Greenberg

Title: The Application of Interferometric Electron Microscopy for Nanomagnetic Imaging

This dissertation has been accepted and approved in partial fulfillment of the requirements for the Doctor of Philosophy degree in the Department of Physics by:

Benjamín Aleman	Chairperson
Benjamin McMorran	Advisor
Raghuveer Parthasarathy	Core Member
Melissa Santala	Core Member
Mark Lonergon	Institutional Representative

and

Kate Mondloch	Interim Vice Provost and Dean of the Graduate School

Original approval signatures are on file with the University of Oregon Graduate School.

Degree awarded December 2020

DISSERTATION ABSTRACT

Alice T. Greenberg

Doctor of Philosophy

Department of Physics

December 2020

Title: The Application of Interferometric Electron Microscopy for Nanomagnetic Imaging

The study of micromagnetics both yields important applications, like computer hard disks which enabled the creation of the internet, and continues to reveal surprising phenomena and open new scientific questions, like the search for the magnetic hopfion [1], a 3D topological soliton. An important trend in micromagnetics research is studying topological magnetic structures, with particular interest in their potential as nanoscale information carriers. For instance, the magnetic skyrmion, a topological soliton, can be as small as 1 nm and may enable new forms of data storage and computing due to its high mobility and topological protection [2]–[4]. However, this is pushing the resolution of imaging techniques. One of the few methods that can image magnetic materials at this scale is transmission electron microscopy (TEM).

Here I will present the use of transmission electron microscopy to study nanoscale topological magnetic domains under an applied magnetic field in a novel thin film material in which both the dipole interaction and the Dzyaloshinskii-Moriya interaction determine the magnetic structure [5]. I demonstrate the first application of scanning TEM holography, a recently developed phase measurement technique, implemented with a diffraction grating to image magnetic materials. Lastly, I propose how this technique

could be used to perform the first experimental observation of a magnetic hopfion and show initial results.

CURRICULUM VITAE

NAME OF AUTHOR: Alice T. Greenberg

GRADUATE AND UNDERGRADUATE SCHOOLS ATTENDED:

University of Oregon, Eugene
University of California Santa Barbara

DEGREES AWARDED:

Doctor of Philosophy, Physics, 2020, University of Oregon
Bachelor of Science, Physics with a minor in Astronomy and Planetary Science, 2014, University of California Santa Barbara

AREAS OF SPECIAL INTEREST:

Electron Microscopy
- Phase Imaging
- 4D Microscopy

Micromagnetism

PROFESSIONAL EXPERIENCE:

Graduate Research Fellow, University of Oregon, 2017-2018, 2020

Graduate Teaching Fellow, University of Oregon, 2015-2016, 2019

Graduate Teaching Fellow, UO Masters Industrial Internship Program, Summer 2016

Graduate Teaching Fellow, UO Science Literacy Program, Summer 2016

GRANTS, AWARDS, AND HONORS:

Student Travel Grant, Annual Conference on Magnetism and Magnetic Materials, 2019

M&M Student Scholar Award, Microscopy & Microanalysis 2019, 2019

Teaching Award, University of Oregon Physics Department, 2019

Poster Award, Advances in Structural and Chemical Imaging, 2017

PUBLICATIONS:

A. Greenberg, H. DeVyldere, J. Pierce, and B. McMorran, “Investigation of mechanical torque applied by electron vortex beams in a liquid cell,” in *Proc. SPIE*, Sep. 2018, vol. 10723, p. 107231O.

A. Greenberg, F. Yasin, C. Johnson, and B. McMorran, “Lorentz Implementation of STEM Holography,” *Microsc Microanal*, vol. 25, no. S2, pp. 96–97, Aug. 2019.

C. W. Johnson *et al.*, “Exact design of complex amplitude holograms for producing arbitrary scalar fields,” *Opt. Express*, vol. 28, no. 12, pp. 17334–17346, Jun. 2020.

TABLE OF CONTENTS

Chapter Page

LIST OF FIGURES

Figure Page

Figure Page

CHAPTER I

INTRODUCTION

Magnetism is ubiquitous in modern life. It is responsible for the function of magnetic key cards and credit cards. It enables electric generators and motors, the key to increasingly popular electric cars. Computer hard disks, which store information in a material's internal magnetic field, enabled the creation of the internet and are still how massive amounts of data are stored worldwide. The digitization of modern life has led to an ever-growing mountain of data. While solid state drives are more efficient, hard disk drives are cheaper and their use in data centers continues to grow [6]. The International Data Corporation reported that all data created, captured or replicated globally reached 18 zettabytes in 2018 and predicts that in 2025 all internet-connected devices will generate 79.4 zettabytes of data in that year alone [7], [8]. Toshiba noted that "the expectation had been that, while the proportion of data stored on flash and SSD increased, there would be a drop in the quantity of data stored on hard drives and magnetic tape. However, it is clear today that all three technologies continue to grow simply because there is so much data to be stored" [9]. One of the ways to increase magnetic memory efficiency and capacity under research is using smaller forms of magnetic memory, such as nanoscale topological magnetic domains or spintronic devices. However, magnetism at the nanoscale can heavily depend on the material's local structure, making careful characterization at that length scale and below vital.

Transmission electron microscopy can be used to study the magnetic structure of a material with 5-10 nm resolution typically [10], although 2-10 Ångstrom resolution is becoming more common [11]–[18]. There are several other techniques that can image magnetic domains at the 10s or 100s of nanometers scale [10], [19], [20], but only one in addition to TEM, spin polarized scanning tunneling microscopy, can also reach the few nanometer to Ångstrom scale [21]. This technique measures the magnetic structure and topography of the surface. In comparison, TEM quantitatively measures the electrostatic and magnetostatic potentials of a sample by measuring the phase these potentials impart on the electron beam. In standard operation TEM measures the integrated signal through the sample, but it can also be used to measure the 3D electrostatic and magnetostatic potentials by tilting the sample. In addition, the TEM can be used to study responses of magnetic materials to an applied magnetic field, applied current, or changing temperature, which is crucial to understanding how they may behave in real-world devices.

The most straightforward method to study magnetic structure in a TEM is called Lorentz TEM (LTEM). In this thesis, I will first present an LTEM study of magnetic domains in a perpendicularly magnetized novel thin film material responding to an applied field. This experiment revealed domain spacing doubling under a weak applied field and domain pattern rotation under higher applied fields. These results highlight the importance of LTEM and its ability to drive theoretical development, as neither phenomenon was expected. They also demonstrate the importance of combining LTEM studies with other magnetic imaging techniques, as LTEM can only reveal the in-plane components of the magnetization.

While LTEM is a powerful tool for quickly and easily studying magnetic domains, it is an indirect measurement of the magnetic phase. Two direct phase measurement techniques, differential phase contrast and off-axis electron holography, are also frequently used to image magnetic materials in a TEM. Differential phase contrast measures the phase gradient across the sample [13], [22], [23]. A promising new microscope design employing differential phase contrast has enabled sub-Ångstrom resolution in a magnetic-field free environment, though they have not yet demonstrated a magnetic measurement [24]. In contrast, off-axis electron holography measures the phase of the sample [25]–[27], meaning it is sensitive to the electric and magnetic *potentials* rather than the electric and magnetic *fields* as with DPC and LTEM. However magnetic imaging in TEM holography mode has not broken 5 Å resolution [15], [18]. A new technique, scanning TEM holography (STEMH) [28]–[34], is a probe-based technique that allows over-sampling like DPC while also directly measuring the phase. STEMH could therefore be the perfect technique to study magnetic structure in this new generation of TEM with Ångstrom resolution in a magnetic field free environment.

Here, I present the implementation of STEMH to study magnetic structure. Two materials were imaged: patterned microstructures of Permalloy, a magnetic nickel-iron alloy, and topological magnetic domains in a perpendicularly magnetized multilayer thin film composed of iron and gadolinium. The results are compared to LTEM measurements. One of the complications that can arise in a STEMH experiment is ambiguity in the source of the measured phase. How that concern impacts the presented results is discussed. Additions to the STEMH experimental procedure that would eliminate this ambiguity are proposed.

Lastly, I will present how STEMH could be used in concert with other techniques to study the 3D structure of a topological magnetic domain, and potentially confirm the first experimental observation of a magnetic hopfion, a topological soliton characterized by a non-zero Hopf index. As mentioned above, TEM measures the integrated signal through the sample. Often the magnetization through a thin film is assumed to be uniform through the thickness. However, this is not the case for many materials [5], [35]–[37]. In particular, micromagnetic calculations of dipole skyrmions, topological circular magnetic domains, show that the magnetization varies through the film but this has not been confirmed experimentally [38]–[42]. Here I present simulated STEMH measurements of a skyrmion that is uniform through the film thickness and of a skyrmion that varies through the thickness as calculated. The simulations show that if these materials are tilted, the measured phases have distinctive features as the tilt angle increases, demonstrating that such a STEMH experiment could confirm the calculated structure of the dipole skyrmion. This structure has a non-zero Hopf index, meaning this would be the first observation of a magnetic hopfion.

Background

Louis de Broglie theorized that electrons act as waves in 1924. Shortly after, in 1932, Max Knoll and Ernst Ruska created the first electron microscope [43]. Within a year it had beaten the resolution possible with visible light [44]. Dennis Gabor invented holography in 1948 originally with the context of providing phase contrast in electron microscopy [45]. Atomic resolution electron microscopy was achieved in 1970 [46]. Electron microscopy, with the power to image materials at the nm to Ångstrom scale, has

become a vital tool in a wide range of research fields, from the semiconductor industry [47], to biomedical research such as the recent imaging of the COVID-19 virus [48].

In addition to its resolution, one of the other powerful aspects of electron microscopy is the ability to image magnetic fields. First developed by Hale [49] and Boersch and Raith [50] in 1959, Lorentz transmission electron microscopy (LTEM) has been widely used to study magnetic domain structure and magnetization reversal mechanisms in magnetic thin films and microstructures. Magnetic domain structure depends on the local microstructure and composition; LTEM provides the ability to study all three at nanometer resolution [10], [51], [52].

Consider a thin film in which the magnetic field points up, down, and then up again across the film with domain walls where the magnetic field lies in the plane of the film, as in Figure 1. If we consider the electron beam interacting with this sample classically, we can see that only where the magnetic field lies in the plane of the film will it influence the electrons, as shown in Figure 1a. This is because the electrons interact with the sample via the Lorentz force $\vec{F} = -e\left(\vec{E} + \vec{v} \times \vec{B}\right)$, where e is the electron charge, $\vec{E}$ is the electric field of the sample, v is the electron velocity, and $\vec{B}$ is the sample's magnetic field. Because the electrons are traveling perpendicular to the film, the cross product $\vec{v} \times \vec{B}$ is nonzero only when $\vec{B}$ points along the thin film. If the electron passes through that region of the film, it is deflected.

While this classical picture is intuitive, it does not fully describe the electron beam-sample interaction. Each electron is in fact a plane wave, as shown in Figure 1b. When this wave interacts with the magnetic sample, it picks up a phase shift from the component of the magnetic vector potential parallel to the optic axis:

$$\phi_m(\vec{r}_\perp) = \frac{-e}{\hbar}\int A_z dz\,. \tag{1.1}$$

This phase shift deforms the electron wavefront, as shown in Figure 1b. From this phase shift, the magnetic field can be calculated:

$$\nabla_\perp(\phi_m) = -\frac{et}{\hbar}\,\vec{B}(\vec{r}_\perp) \times \hat{e}_z. \tag{1.2}$$

Therefore, the goal of magnetic TEM imaging is to measure the phase shift imparted on the electron wave.

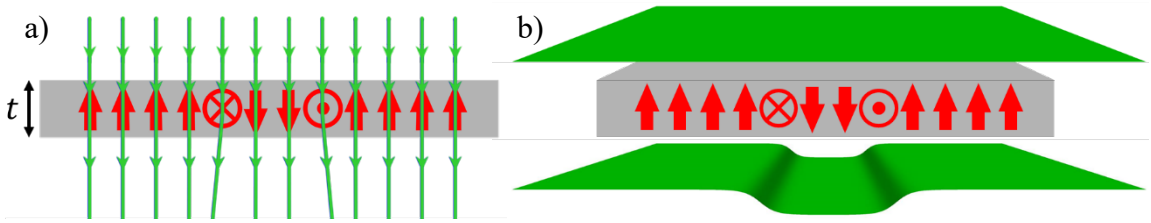

Figure 1: Electron Beam Interaction with a Magnetic Thin Film
Electron beam interacting with a magnetic thin film of thickness t from a) the classical picture and b) the quantum mechanical picture. The magnetic field of the thin film is indicated by red markers. In a) electron paths are indicated by green lines. In b) the electron wavefront is in green. This figure incorporates part of Figure 1 in "Determination of domain wall chirality using in situ Lorentz transmission electron microscopy" by Chess et al. in AIP Advances, used under CC BY.

In typical operation of conventional TEM, the sample sits within the objective lens, which is a magnetic field typically around 2 T. For many magnetic materials this field saturates the magnetization in the direction of that field, and the magnetic structure being imaged is destroyed. In LTEM, the objective lens is turned off so the sample is in a magnetic-field-free environment. A lens below the sample, called the Lorentz lens, forms the image of the sample instead of the objective lens.

In order to see the magnetic structure, the image of the sample must be defocused. This can be visualized if we return to the classical picture of the electron beam interacting with the sample, as in Figure 2. If the sample plane is being imaged, the electron beams

have not deflected yet and there is no contrast. If instead a plane below the sample is imaged, the deflected paths cause an excess of electrons in one region and a dearth of electrons next to it. This creates contrast at domain walls in the material.

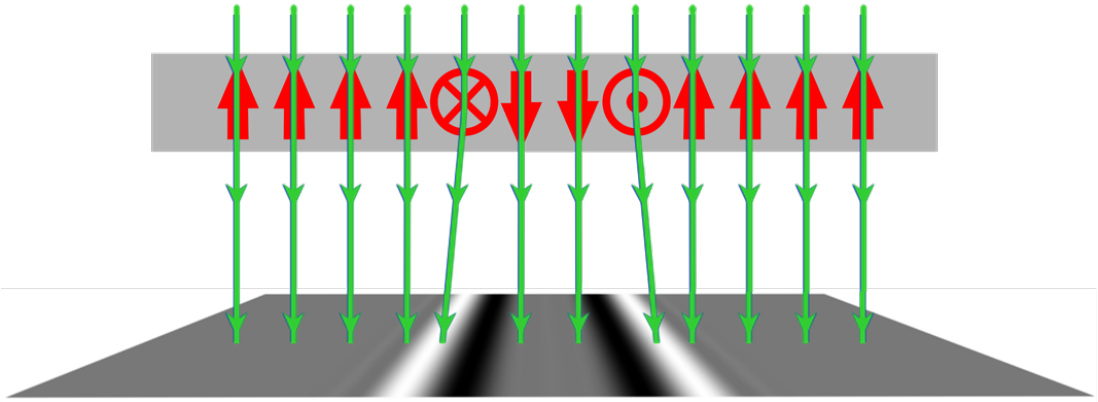

Figure 2: Contrast Formation in Lorentz TEM
This figure incorporates part of Figure 1 in "Determination of domain wall chirality using in situ Lorentz transmission electron microscopy" by Chess et al. in AIP Advances, used under CC BY.

Again, the classical picture provides useful intuition but is not quantitative. To consider this quantitatively, we must return to the quantum mechanical picture. Above the sample the electron is a plane wave, mathematically described as

$$\Psi_0(\vec{x}) = e^{2\pi i k_z z}. \tag{1.3}$$

After interacting with a weak phase object, the electron acquires a phase from the magnetic structure ϕ_m and the wavefunction becomes

$$\Psi_f(\vec{x}) = e^{2\pi i k_z z} e^{i\phi_m}. \tag{1.4}$$

Here we have assumed the thin film is uniform so the electrostatic phase is uniform and can be ignored in this calculation. The wavefunction at the detector is the convolution of the wavefunction after the sample and the microscope's point spread function, which

accounts for the microscope's optical aberrations and the defocus used. The image collected is the absolute value of this wavefunction squared, or

$$I(\vec{r}_\perp, \Delta f) = \left|\Psi_f(\vec{r}_\perp) \otimes h(\vec{r}_\perp, \Delta f)\right|^2, \tag{1.5}$$

where $\vec{r}_\perp$ is the coordinate vector in the plane of the image, Δf is the defocus, and h is the point spread function. Typically, to calculate the magnetic phase, an overfocused, underfocused, and focused image are taken. From the three, the transport of intensity equation (TIE) gives

$$\nabla_\perp^2 \phi_m = -\frac{2\pi}{I_0 \lambda} \frac{I(\vec{r}_\perp, \Delta f) - I(\vec{r}_\perp, -\Delta f)}{2\Delta f} \tag{1.6}$$

where I_0 is the in-focus image, $I(\vec{r}_\perp, \Delta f)$ is the overfocused image, and $I(\vec{r}_\perp, -\Delta f)$ is the underfocused image [53]. If the sample has uniform thickness and few features present in the in-focus image (I_0 is constant), the equation above can be simplified to

$$\nabla_\perp^2 \phi_m = \frac{2\pi}{\lambda \Delta f}\left(1 - \frac{I(r_\perp, \Delta f)}{I_0}\right) \tag{1.7}$$

and the phase can be calculated from a single defocused image [38]. This relation can be used to recover the phase from a single defocused image, an analysis method called the single image transport of intensity equation (SITIE).

In the next chapter, I will present domain wall evolution in response to an applied magnetic field studied via Lorentz TEM using SITIE analysis.

CHAPTER II

THE EVOLUTION OF MAGNETIC SPIN TEXTURES IN BROKEN-SYMMETRY FILMS UNDER AN APPLIED MAGNETIC FIELD

Introduction

Chiral spin structures in nanomagnetic systems are a timely research topic. These topologically-nontrivial magnetic structures challenge current analytical models and are potentially useful as spintronic information carriers due to their topological stability and high speed displacement under low threshold currents [54]–[58]. Bloch and Néel domain walls are examples of chiral spin structures [59], [60]. In a magnetic thin film possessing perpendicular magnetic anisotropy, magnetic domains point up or down with respect to the plane of the film. In these materials, Bloch-type domain walls separating up/down domains have a wall magnetization that lies along the wall. If the magnetization lies perpendicular to the wall, it is Néel-type. Both Néel and Bloch domain walls can have two chiralities corresponding to one of two directions in which the magnetization rotates in the transition from an "up" domain to a "down" domain. In materials with high symmetry, there is no preferred domain wall chirality, and one finds a statistically balanced mixture of left-handed and right-handed domain walls [58].

Spin structures with a preferred chirality are found in magnetic systems lacking inversion symmetry [61]. One effect that can cause this is the Dzyaloshinskii-Moriya interaction (DMI) [62]–[65]. In thin films, DMI is a result of spin-orbit coupling of interfacial atoms neighboring the magnetic layer. Chiral spin structures can also be created by dipolar interactions in thin films without DMI [38]–[42]. Only very recently has the interplay between the two effects been considered [5], [35]–[37].

In domain walls dominated by dipolar interactions, the magnetization changes from Néel-type at the surfaces to Bloch-type at the center of the film thickness [39]–[42]. Adding layers that induce interfacial DMI moves the Bloch wall part off-center in the thickness of the film [5], [36], [37]. Studies suggest that systems with significant DMI and dipolar interaction contributions have very different dynamics than DMI-dominated systems [36] and enhanced stability [35]. As few theoretical and computation studies [35]–[37] and even fewer experimental measurements [5] of these systems have been published, the effect of combining dipolar interactions and DMI is still relatively unknown.

Multilayer thin films composed of iron and gadolinium support dipolar chiral spin structures [39]–[42]. The effect of adding interfacial DMI is studied by adding platinum layers. The strength of the DMI was varied by varying the number of platinum layers; three samples were studied: [(Fe(3.4A)/Gd(4A))x20/Pt(1A)]x4 (FeGd80Pt4), [(Fe(3.4A)/Gd(4A))x10/Pt(1A)]x8 (FeGd80Pt8), [(Fe(3.4A)/Gd(4A))x5/Pt(1A)]x16] (FeGd80Pt16). Full-Field Transmission Soft X-ray measurements performed by collaborators at the Advanced Light Source, which is sensitive to the average thickness perpendicular magnetization, revealed that the stripe magnetic domains rotated under an applied magnetic field (S. Montoya, unpublished observations). In addition, simultaneous anisotropic magneto resistance and Hall resistivity field-dependent measurements performed by collaborators at UCSD show a topological Hall effect-like signal. This is typically associated with the existence of topological domain structures called skyrmions in the material, though that is not the case in this thin film material. Here, Lorentz TEM is

used to further characterize the evolution of the domain wall morphology under an applied magnetic field.

Under weak applied fields (≤ 50 mT), the spatial frequency of the stripe domains appears to halve while the orientation remains the same. This does not appear in the X-ray images (S. Montoya, unpublished observations), suggesting more variation in the domain wall structure than expected. Under a finite range of higher applied field values (50 – 150 mT), the domain walls rotate and stay in the new orientation when the field is turned off. This is true when the magnetic field is applied through any amount of that rotation. When a magnetic field is then applied in the opposite direction the domain walls return to the original orientation. If the magnetic field is applied up to a value before rotation occurs, and then applied to saturation in the opposite direction, the domains do not rotate. Both the weak field frequency halving and domain rotation are the result of the asymmetric domain walls and a preferred domain wall chirality, caused by the platinum layers in the film. These observations highlight the utility of LTEM in studying novel magnetic materials and the importance of using it in conjunction with other magnetic imaging techniques sensitive to the perpendicular magnetization.

Methods

Fe/Gd/Pt films were grown on 100 nm thick silicon nitride membranes via sputter deposition by Sergio Montoya at UCSD. The films are produced by alternating deposition of iron, gadolinium, and platinum. X-ray diffraction of Fe/Gd films with no platinum layers produced in the same way indicate that the layers intermix and form an amorphous structure [40], [66]. Three samples were produced with 80 layers of iron and gadolinium and varying numbers of platinum layers: [(Fe(3.4Å)/Gd(4Å))x20/Pt(1Å)]x4

(FeGd80Pt4), [(Fe(3.4Å)/Gd(4Å))x10/Pt(1Å)]x8 (FeGd80Pt8), and [(Fe(3.4Å)/Gd(4Å))x5/Pt(1Å)]x16] (FeGd80Pt16). The sample deposition and layer structure are summarized in Figure 3. The samples were imaged using Lorentz TEM in an 80-300 kV FEI Titan TEM in the Center for Advanced Material Characterization in Oregon to observe the magnetic domains as a magnetic field was applied to the sample via weak excitation of the objective lens. The silicon nitride membranes are supported by a silicon chip with a window in the center. The area imaged was roughly in the center of the chip window, found by locating two opposite corners of the square window and then moving to the middle point between them. Before each experiment a magnetic field was applied parallel to the optic axis until the magnetization saturated and then antiparallel to the optic axis until saturation so that each measurement would be directly comparable to each other as well as to the X-ray measurements.

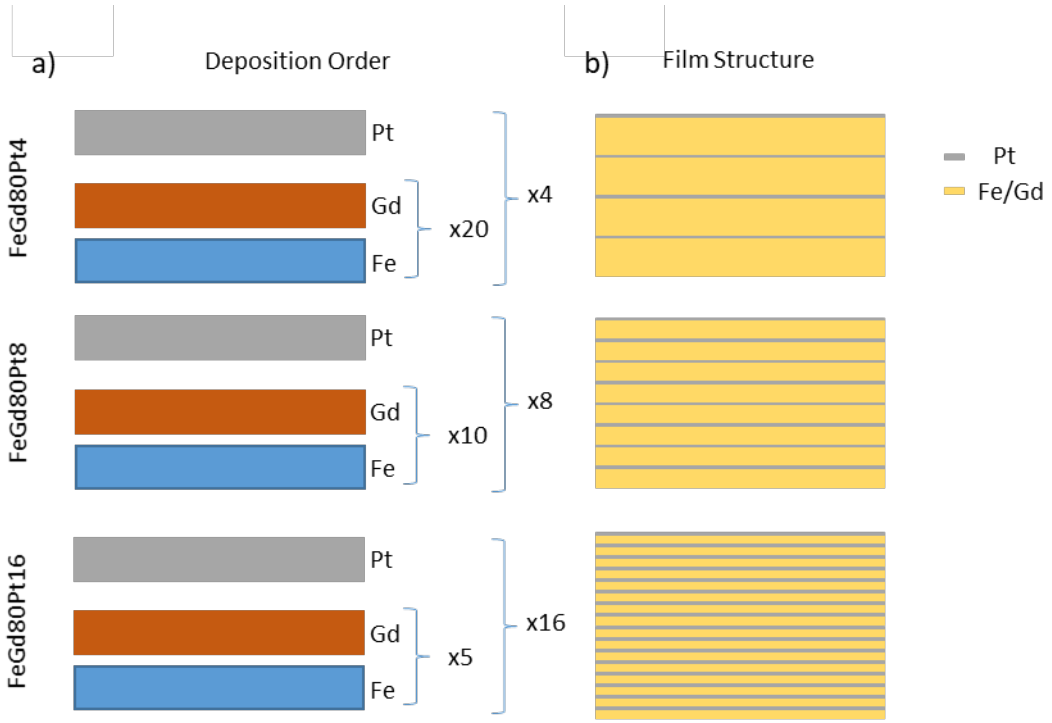

Figure 3: Fe/Gd/Pt film Growth
a) The deposition order for each film. b) The approximate structure formed where grey indicates platinum and yellow indicates intermixed iron and gadolinium.

During the experiment, the external magnetic field is changed by adjusting the current to the electromagnetic objective lens. The lens current is expressed as a percentage of its maximum applied current. Over the relevant range (± 10% maximum lens current) the field of the lens is proportional to the applied current. The field at the sample is calculated from a linear regression of measurements of the objective lens field as a function of percent power in two other FEI Titans [67], [68]. Due to hysteresis in the lens, the relationship between the lens current and the produced magnetic field depends on the direction in which the current is being changed. Measurements of this effect in a different Titan found that the magnetic field value at 0% lens current changed by 6 mT [68]. The linear regression calculation used here does not account for this variation. Characterizing the objective lens of the specific Titan used will improve future experimental precision.

LTEM is sensitive to the in-plane component of the sample's magnetic field. The films imaged form stripes of out-of-plane magnetic domains separated by in-plane magnetic domain walls. In a Bloch-type domain wall, the magnetization points along the wall. In a Néel-type domain wall, the magnetization points perpendicular to the wall. In these Fe/Gd/Pt films, the domain walls contain both Bloch and Néel components that vary through the thickness of the film. However, the Néel component produces no LTEM contrast. This can be visualized classically; if the magnetization points perpendicular to the domain wall in the plane of the film, the electrons are kicked along the wall by the Lorentz force. As each neighboring spin does the same, no contrast is formed. Therefore, LTEM images of the Fe/Gd/Pt films reveal only the Bloch-component of the domain

walls integrated through the film thickness. This creates a pattern of alternating bright and dark stripes (Figure 4).

The in-plane magnetic field is calculated from the LTEM images using the single image transport of intensity equation (SITIE) [38]. Before this can be done the images must be aligned. As the objective lens is weakly excited, it applies a magnetic field not only to the sample but also to the imaging electrons, causing the image to rotate and shift. Defects in the silicon nitride membrane appear as circular features and provide stable markers for alignment. Each set of images is aligned and cropped to the overlapping area [69]. While these defects are convenient for alignment, they create artifacts in the calculated magnetic field if not removed. In image sets where the film was saturated, the image at saturation contains only the defects. To remove them from the rest of the image set, the image at saturation is subtracted. In some of the experiments, the magnification changes slightly at saturation so the defects are not perfectly removed and leave small rings or bumps. Figure 4a includes examples of this effect in images of FeGd80Pt8. In experiments where a saturation image is not taken, an approximate background image is created by finding the defect pixels via thresholding and Gaussian smoothing the rest of the image to remove the magnetic features. That approximate background image is then subtracted to remove the silicon nitride defects. An example of this process done with images of FeGd80Pt8 is shown in Figure 4b. The in-plane magnetic field is calculated from these background-subtracted images.

Another feature of interest is the domain wall spacing and orientation. These are calculated from the Fast Fourier Transform (FFT) of the aligned, background-subtracted image. Because the domains are not perfectly straight, rather than a sharp peak in the

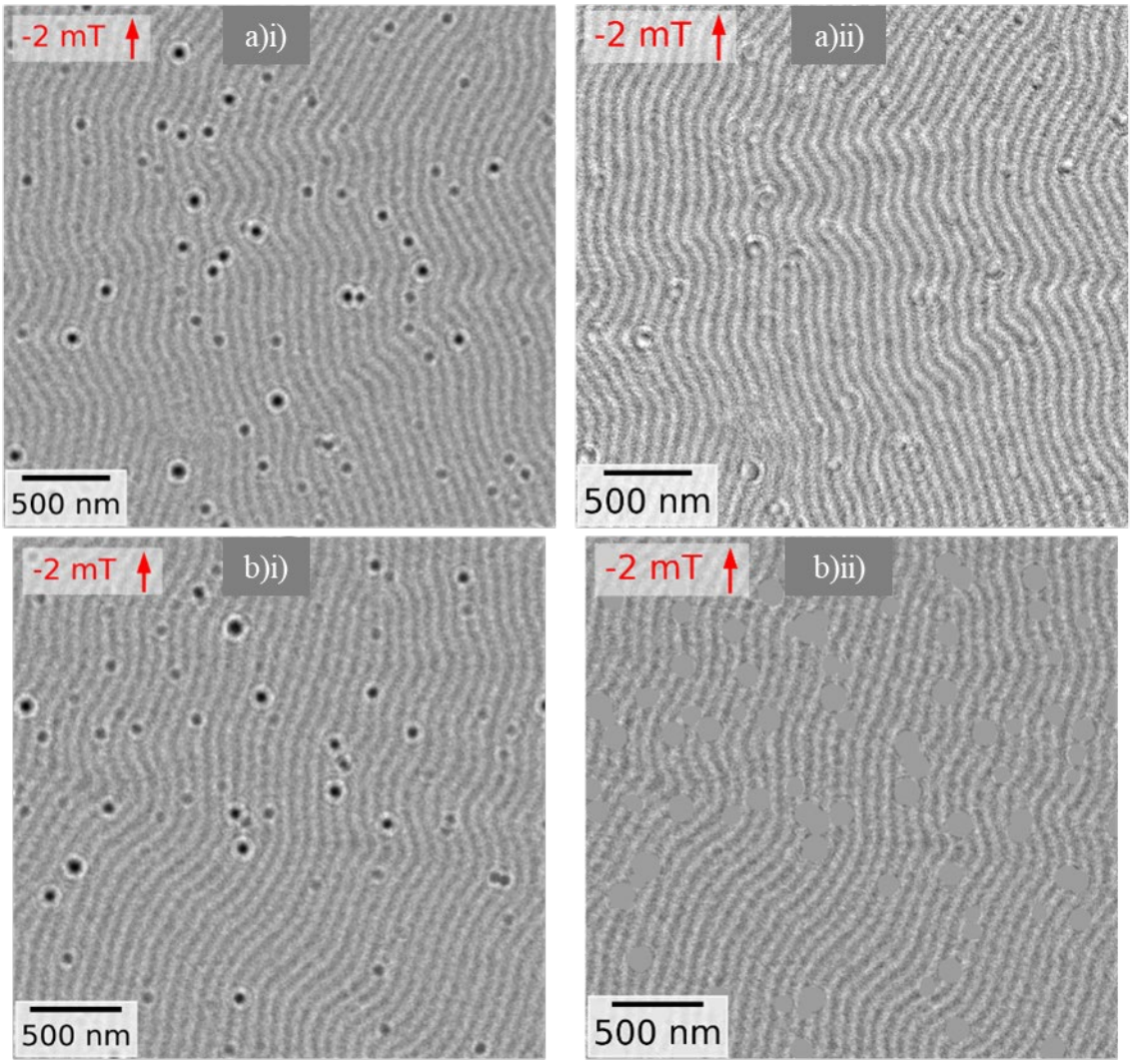

Figure 4: Examples of Background Subtraction
a) i) Underfocused LTEM image of FeGd80Pt8. Defects in supporting membrane are visible as dark circular features. ii) Same image with image at saturation subtracted. Defects are mostly removed. b) Underfocused LTEM image of FeGd80Pt8. ii) Same image with approximate background image subtracted. Defects are replaced with blank circles. Red arrows indicate the applied field is being increased.

FFT, an arc is created, as shown in Figure 5c. The pixel locations of the arc are found by thresholding the log of the FFT above 93% of its max value. For images with arcs at only one radius, corresponding to only one domain spacing in the image, the k-vector length is found by the average of the arc pixels' radii weighted by their intensity. This is converted to the real space distance by $d = W/r_k$ where W is the size of the field of view in

microns and r_k is the k-vector radius in pixels. For a given experiment these values are then averaged over the set of images containing only that k-vector. To determine the orientation, k-means clustering is used to separate the found arc pixels into two clusters [70]. This is done for images with one or two spacings present. For each cluster the angular center and standard deviation weighted by the pixel intensities on the range [0, 360°) is found using circular statistics [71], [72]. The two clusters should be 180° apart, so the orientation in the first image is defined as

$$\bar{\theta} = \frac{\theta_0 + (\theta_1 - 180°)}{2} \tag{2.1}$$

where θ_0 is the circular mean of the cluster in the top half of the FFT and θ_1 is the circular mean of the cluster in the bottom half. In each subsequent image's FFT, the 0^{th} cluster is chosen as whichever is closest to the previous image's 0^{th} cluster. The angle of the first image is set to 0 so the orientation is relative to the first image in the set.

Weak Field Evolution

LTEM images of the films show alternating bright and dark stripes, as shown in Figure 5a (arrows in the field label indicate that the field strength is being increased). Using SITIE to compute the in-plane magnetic field shows this contrast variation is the result of alternating Bloch walls, shown in Figure 5b where the in-plane magnetic field direction and magnitude are indicated by the color hue and saturation respectively. Under an external magnetic field, the spatial frequency of the stripes halves as revealed by the Fast Fourier Transform of the LTEM images, shown in Figure 5c. This effect occurs gradually. At low field values only one set of peaks appears in the FFT. As the applied field increases, every other dark stripe is swallowed by its neighboring bright stripes while the remaining dark stripes expand. In Fourier space, a lower-frequency set of

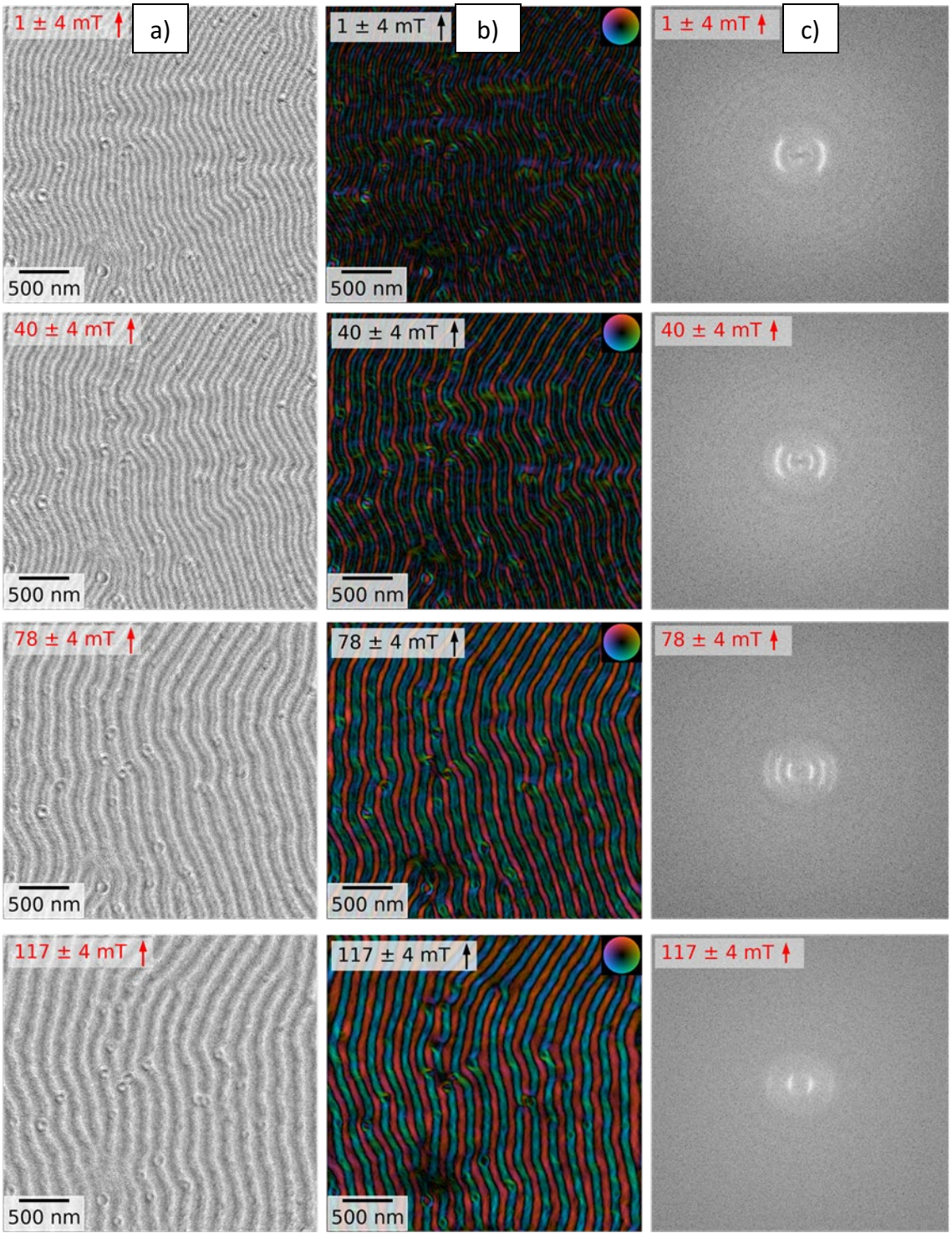

Figure 5: LTEM Images of FeGd80Pt8 as a Magnetic Field is Applied
a) Underfocused, background-subtracted LTEM images of FeGd80Pt8 as a magnetic field is applied parallel to the optic axis. b) The calculated in-plane magnetic field from each image (direction and magnitude are indicated by the hue and saturation respectively). c) The FFT of each LTEM image. Arrows in the field label on each image indicate that the applied field strength is being increased.

peaks appears as the field is increased. Close to saturation, the original higher-frequency set of peaks disappears and only the low-frequency set of peaks remain. To study this further, a small area of images of FeGd80Pt8 from the same experiment is shown in Figure 6. The bottom row of each image set is the same sub-area of the sample in the series of LTEM images. A line profile through the center of the sub area, summed in the *y* direction between the red lines on the LTEM image, is shown below each image. From image to image, every other trough in the line profile is raised until the neighboring peaks merge (an example is highlighted by a red arrow). In the images of the reconstructed magnetic field (top images), this appears to be the result of every other Bloch wall pointing in the +*y* direction (red stripes) being swallowed by its neighboring Bloch walls pointing in the -*y* direction (blue stripes), while the remaining +*y* Bloch walls expand.

If one assumes that every apparent Bloch wall initially divides domains that point out of or into the page (in the +*z* and -*z* directions, respectively), this suggests that two neighboring domains are flipping to combine with their in-plane domain walls as a magnetic field is applied perpendicular to the film. However, full-field transmission X-ray microscopy, which is sensitive to the out-of-plane magnetic field, shows no change in the domain frequency (S. Montoya, unpublished observations). The domain spacing measured by X-ray microscopy in the FeGd80Pt16 film is 153 ± 7 nm (S. Montoya, unpublished observations). The average domain spacing in LTEM images of all the samples under a weak applied field is 81 ± 1 nm, found from images with only a high-frequency arc in the image's FFT. The average domain spacing in higher applied fields is 172 ± 7 nm, found from images with only a low-frequency arc in the image's FFT. While this differs slightly from the spacing measured in the X-ray experiment, the value at

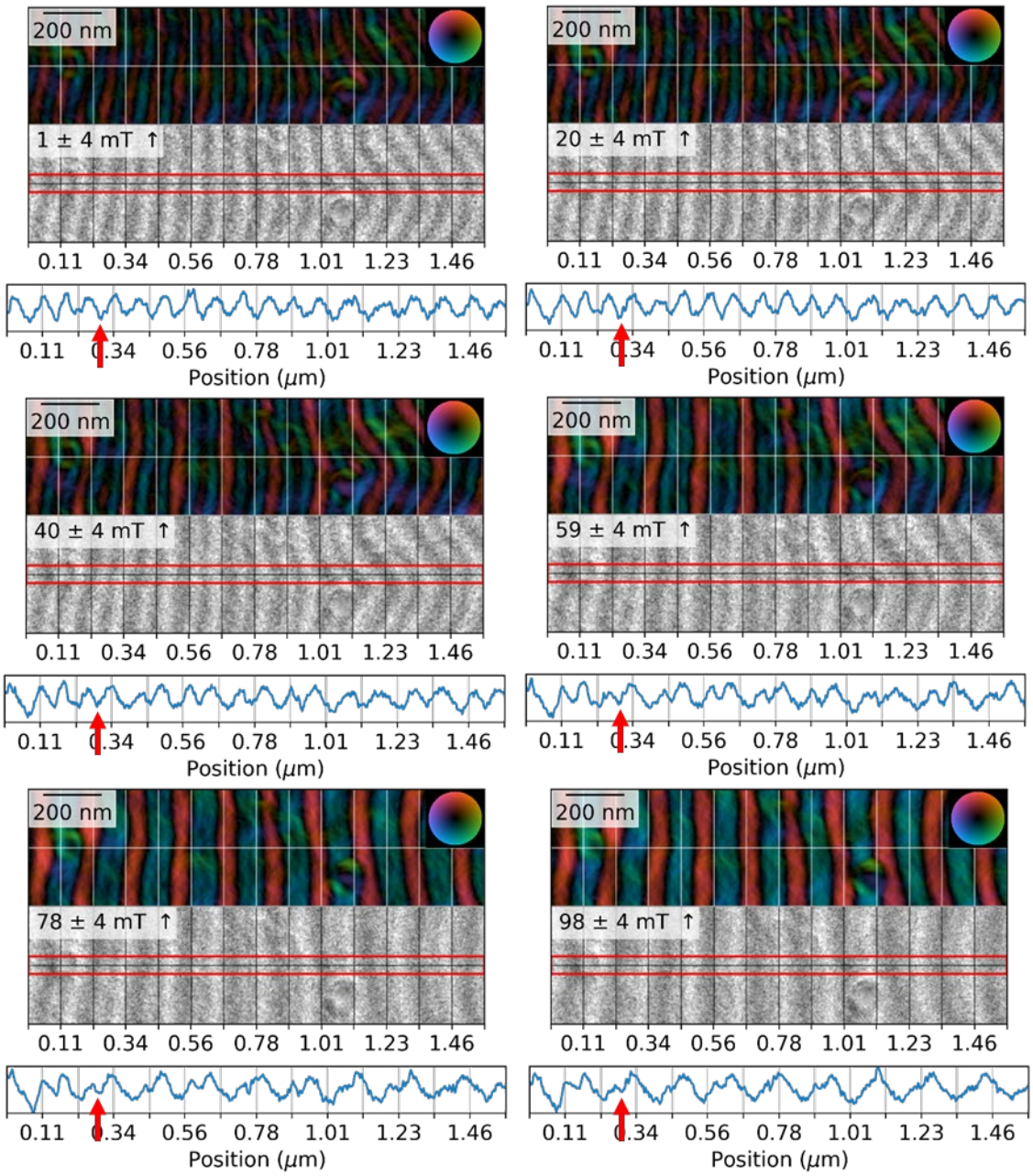

Figure 6: Stripe Domain Spatial Frequency Halving with Applied Magnetic Field
A small area of LTEM images of FeGd80Pt8 under a weak applied magnetic field (saturation image subtracted to reduce defects in the supporting SiN membrane) and the in-plane magnetic field calculated from the images (direction and magnitude are indicated by the hue and saturation respectively) as a magnetic field is applied parallel to the optic axis. The images are ordered left to right and top to bottom. Arrows in the field label indicate the field is being increased.

higher applied fields is much closer than that in weak applied field. This suggests the

doubled frequency in LTEM images at low applied field is not actually due to a finer,

doubled set of uniform Bloch walls, but is instead a result of a projection through a domain wall with a more complicated 3D structure that varies asymmetrically through the thickness. As a field is applied, a small in-plane component could be removing this

Previous studies on other material systems have indicated that the domain walls have a hybrid structure varying from Néel-type at the surfaces to Bloch-type within the film thickness, narrowing at the center [5], [35]–[37]. In purely Fe/Gd films these Néel caps are symmetric [38]–[42]. With the Pt layers, the Néel caps become asymmetric [5], [36], [37], as shown in Figure 7. Through the middle of the domain wall the integrated signal is dominated by the Bloch center. However, through the edges of the domain wall, the integrated signal is dominated by the Bloch component of the larger asymmetric Néel cap. If the magnetic spin varied from purely Néel-type at the surfaces to the Bloch-center (Figure 7ai), the entire domain wall would appear Bloch-type in LTEM (Figure 7aii). If the caps possess a Bloch component in the same direction as the Bloch-center, again the entire wall would appear as a uniform Bloch wall. However, if the Bloch component of the Néel caps varies across the domain wall or through the film thickness, the single wall could appear as multiple domain walls in an LTEM projection. For example, consider if the larger Néel cap contained a Bloch component antiparallel to the Bloch center (Figure 7bi). While the middle of the wall would appear as the Bloch center, the edges would appear antiparallel to it. The single domain wall would appear as three alternating domain walls (Figure 7bii). The apparent frequency halving under an applied field could be the result of a small in-plane component of the external field forcing the Néel caps' Bloch components to align. A Bloch component in the Néel caps is unexpected as it has not

been predicted by micromagnetic simulations of hybrid walls [5], [36], [37] nor observed experimentally [5].

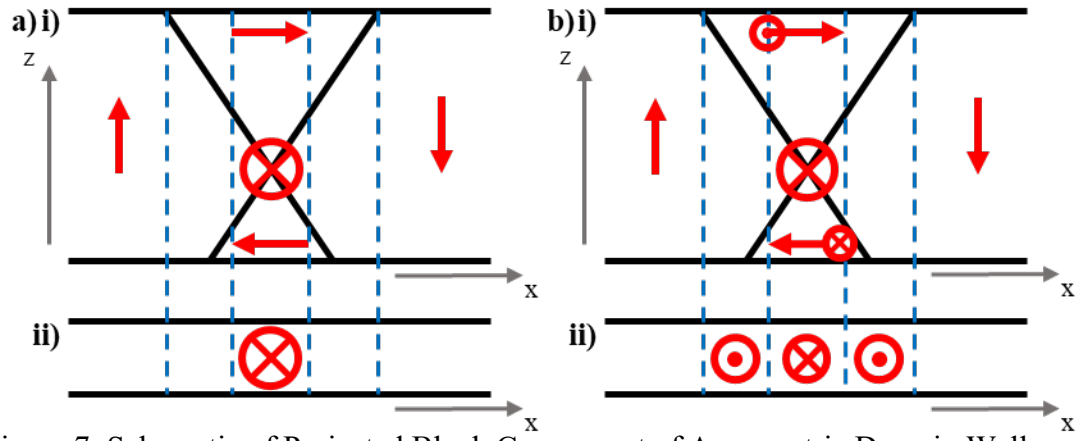

Figure 7: Schematic of Projected Bloch Component of Asymmetric Domain Walls i) *x*-*z* profile of domain wall extending in *y*-direction with a Bloch center and a) pure Néel caps or b) Néel caps with a Bloch component. The magnetization is indicated in red. The surfaces of the film and domain wall boundaries are indicated in black. ii) The Bloch component summed through the film thickness i.e. in *z*.

These results demonstrate the importance of using multiple magnetic imaging techniques, as they are frequently not sensitive to all three components of the magnetization. While the full magnetic structure cannot be determined by LTEM alone, comparing simulated LTEM images from micromagnetic calculations of the domain wall to the experimental images could further elucidate the cause of the apparent frequency halving. In addition, LTEM tomography may reveal depth-dependent detail. These results could also be combined with surface-sensitive measurements like scanning electron microscopy with polarization analysis (SEMPA) or magnetic force microscopy (MFM).

Domain Rotation

Full-field soft transmission X-ray microscopy revealed that as an external magnetic field is applied perpendicular to the film, the stripe domains rotate (S. Montoya, unpublished observations). An example of this rotation in FeGd80Pt16 is shown in

Figure 8, featuring a sequence of underfocused, background-subtracted LTEM images of the center of the film. An external magnetic field is increased until the film is saturated and then reduced back to 0 (images ordered left-to-right and top-to-bottom). A dashed red line indicates the approximate original orientation. As the field is increased, the domain patterns rotated counter-clockwise. After the film is saturated and the field is reduced the domains maintain the new orientation. This trend is observed in all three films. Similar experiments recording LTEM images of the center of the film as the external field is increased until the film saturated and then reduced to zero were conducted with the FeGd80Pt4 and FeGd80Pt8 films. By calculating the rotation as described in the Methods section, I found that the maximum rotation decreased with an increasing number of platinum layers in the film, and therefore increasing DMI strength, as summarized in Figure 9. The magnetic field value at which rotation begins also decreases with an increasing number of platinum layers in the film.

The measurements mentioned above show that if the magnetic field is applied until the film saturates and then turned off, the domains maintain their new orientation. Because the rotation occurs gradually over a range of applied field values, the next experiment conducted was to explore if the domain pattern would remain rotated if the field increased to a value below saturation. The domain morphology in the center of the FeGd80Pt8 film was recorded with LTEM as an external field was increased to a maximum value below saturation (33 ± 4 mT, 53 ± 4 mT, 65 ± 4 mT, 78 ± 4 mT, 98 ± 4 mT, 104 ± 4 mT, 117 ± 4 mT, and 130 ± 4 mT) and then reduced to zero. In between each experiment, the domain structure was reset by saturating the sample with a large

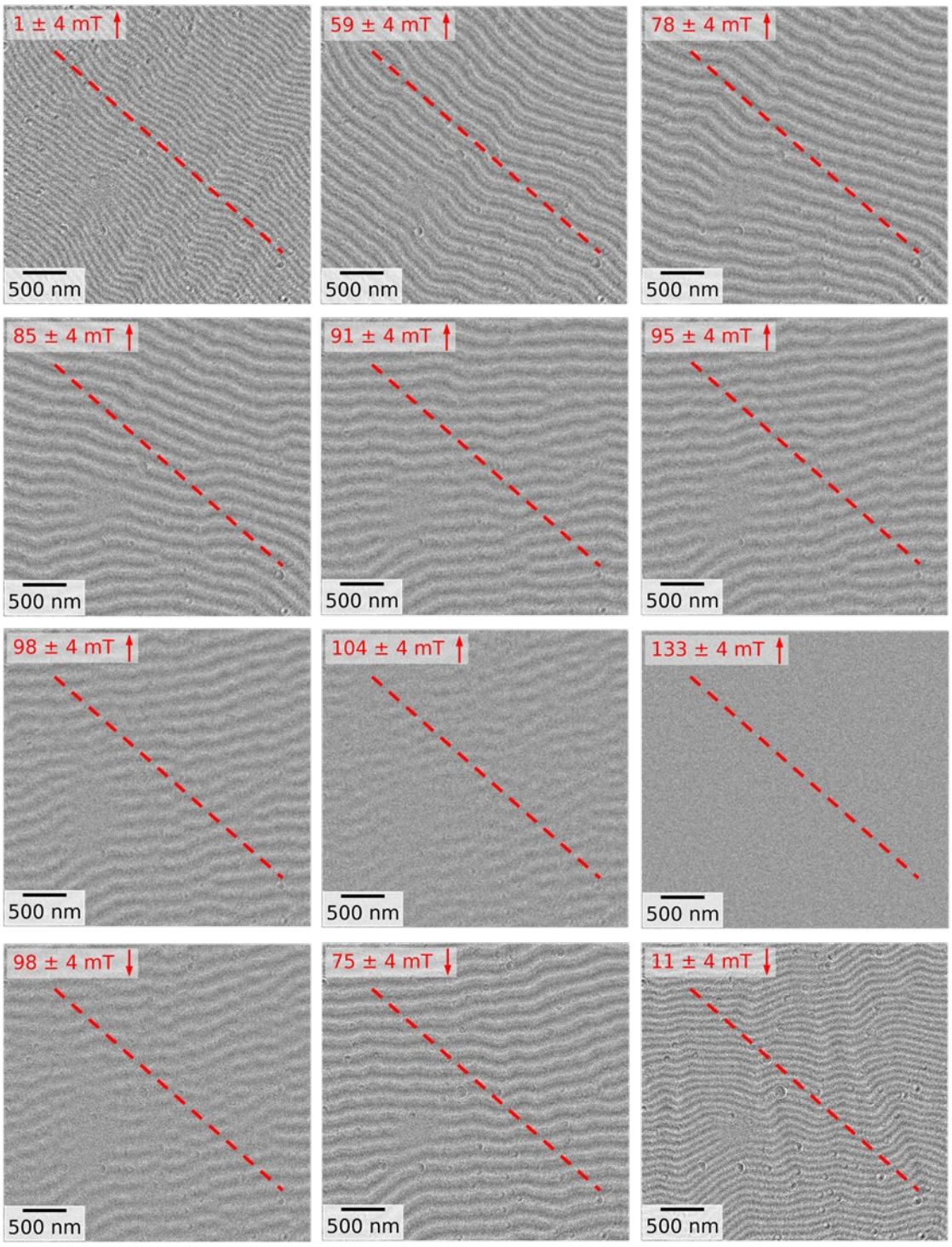

Figure 8: Domain Wall Rotation Under an Applied Magnetic Field
Underfocused, background-subtracted LTEM images of FeGd80Pt16 under an out-of-plane applied magnetic field, ordered left-to-right and top-to-bottom. The applied field strength in mT is in the top left corner of each corner. A red arrow indicates if the field is being increased or decreased. The original domain wall orientation is shown by a red dashed line.

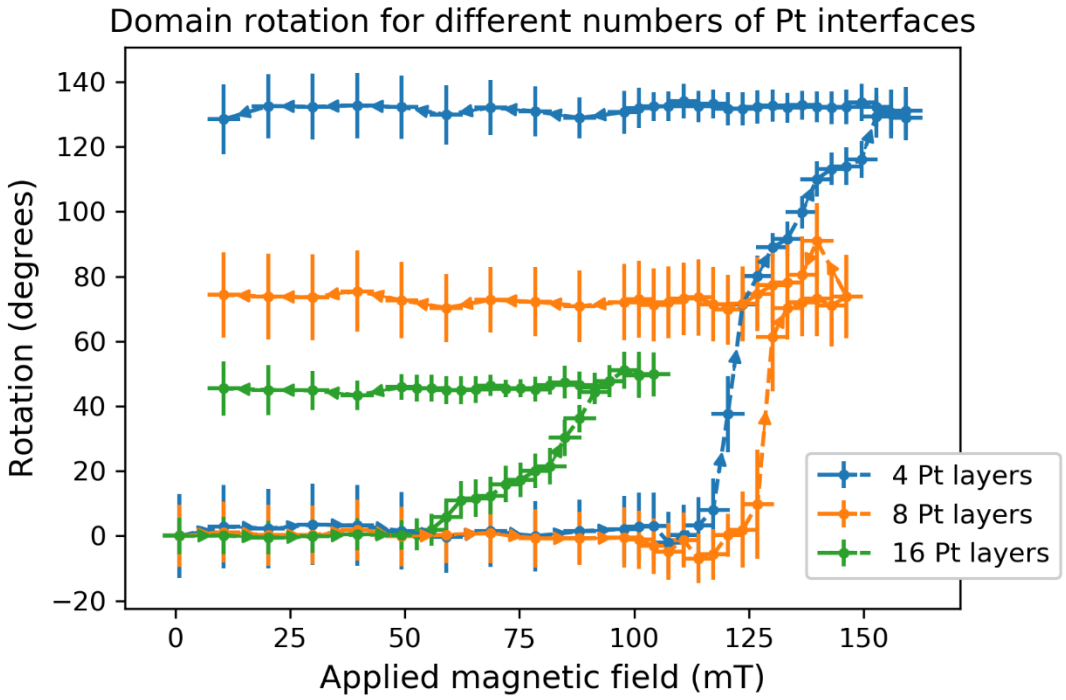

Figure 9: Domain Rotation under an Applied Magnetic Field for all Three Films
Domain rotation relative to the domain orientation in the first image of each experiment as a function of applied magnetic field. The results of this experiment conducted with FeGd80Pt4, FeGd80Pt8, and FeGd80Pt16 shown in blue, orange, and green lines respectively. Arrows indicate the order of the measurements in each experiment.

positive field, then a negative saturating field, and then returning the field to 0. The film was not moved between experiments. The domains did not rotate in the first four trials, in which the field was increased to 33 ± 4 mT, 53 ± 4 mT, 65 ± 4 mT, 78 ± 4 mT respectively, as shown in Figure 10a. The last four trials show an increasing rotation magnitude with increasing maximum applied field, (Figure 10b). However, the last two trials, with max applied magnetic fields of 117 ± 4 mT and 130 ± 4 mT respectively, show clockwise rotation (negative) whereas the previous two show counterclockwise rotation (positive). In addition, the domains begin to rotate at a lower applied magnetic field value than in the experiments summarized in Figure 8. Clearly something about the local magnetic structure has changed. While, as described above, a large positive field

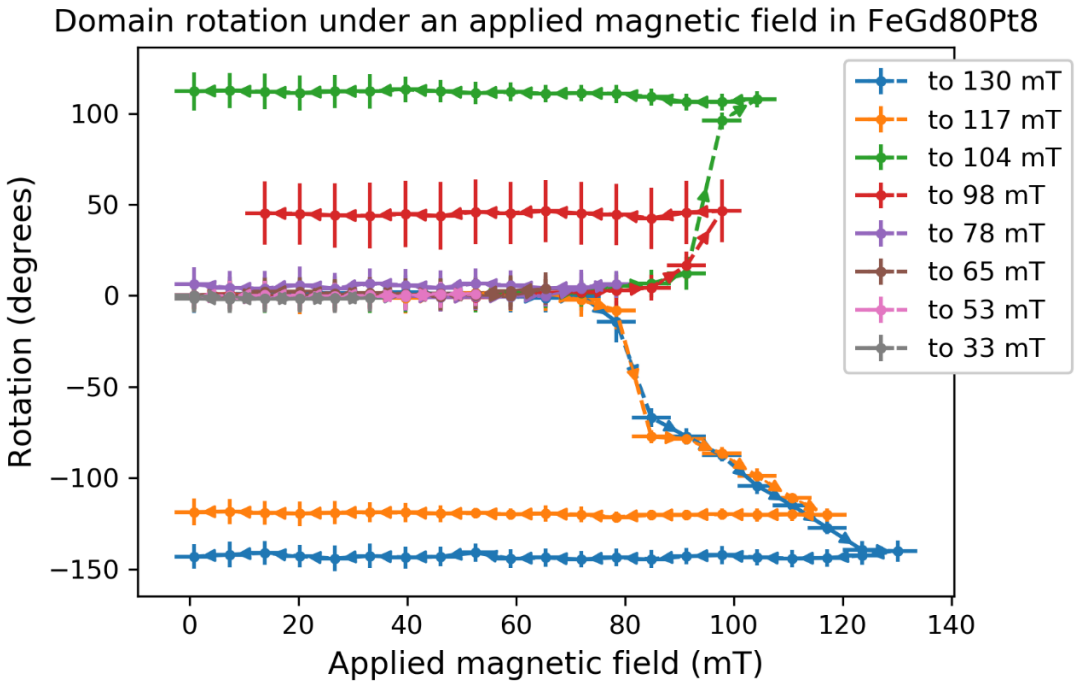

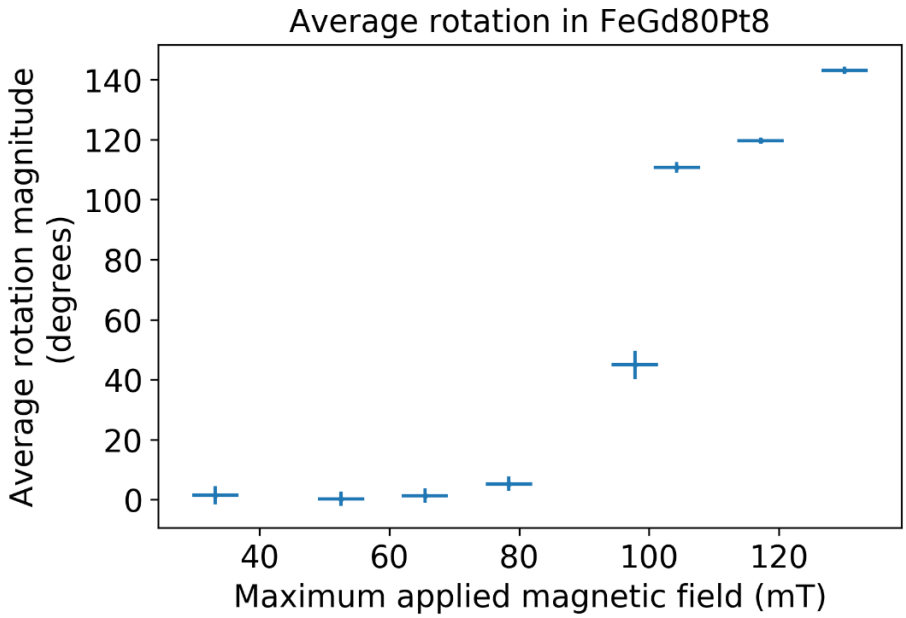

Figure 10: Domain Rotation Stability
a) Domain rotation in FeGd80Pt8 under an applied magnetic field increased to different maximum values as given in the plot legend. b) Average domain rotation magnitude as a function of maximum applied magnetic field value. The average is taken over all the images after the maximum applied field is reached.

and then large negative field was applied to the sample between each experiment to ensure the magnetic structure would begin each trial in the same state, it is possible the applied field values were not high enough to truly saturate the film and reset the field history. It is also possible the maximum applied saturating field value inadvertently differed between trials. The difference in the energy at which rotation began in the different trials could be due to the domains being pinned in some cases, requiring a larger applied field before they move In all the trials, once the domains rotated, they maintained the new orientation as the field was reduced to zero.

The next experiment conducted was to explore what happens when the field is then applied antiparallel to the original direction. An external magnetic field applied to the FeGd80Pt8 film was increased to just before domain rotation, reduced to zero, and then applied antiparallel to the initial field until the film was saturated (the blue line in Figure 11). After resetting the magnetic history, the field was applied to saturation, decreased back to 0 and then applied antiparallel to saturation (the orange line in Figure 11). These experiments are summarized in Figure 11, in which the domain orientation relative to that of the first image in each experiment is plotted against the applied magnetic field. Arrows along each line indicate the image order. In the first case, the domains did not rotate over the course of the trial. In second case, the domains rotated, maintained the new orientation as the field was reduced, and rotated back to the original orientation as the field is applied in the opposite direction.

This trend did not hold when the film was moved to a new imaging area after the field is reduced to zero, as shown in Figure 12. A positive field was applied to FeGd80Pt8 through saturation and then reduced to zero, over which the domains in the

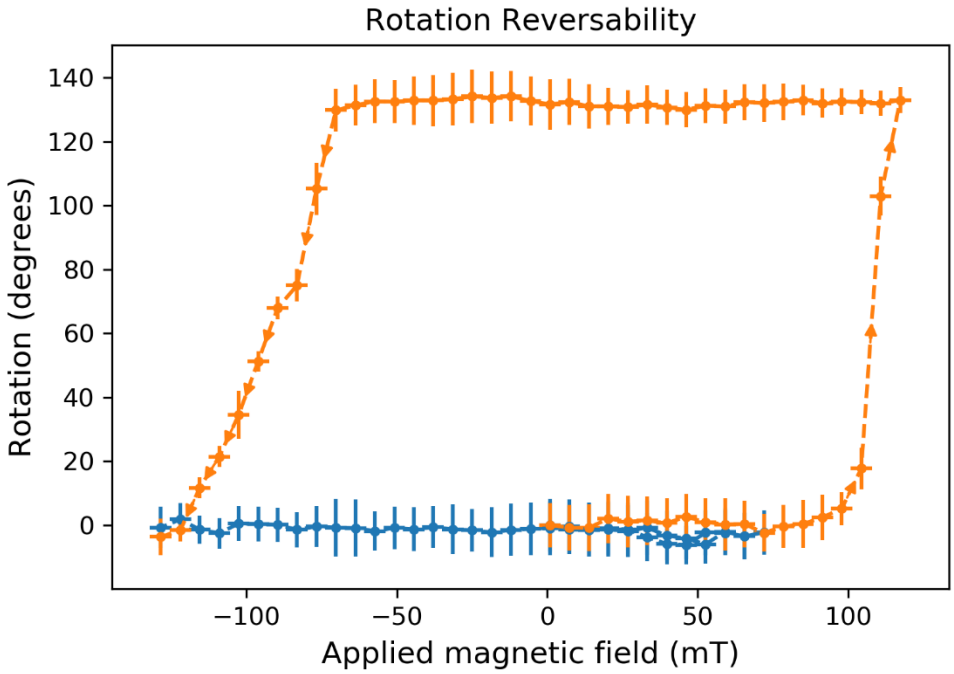

Figure 11: Rotation Reversibility with Opposite Magnetic Field
Plot of domain rotation as a function of applied magnetic field showing 1) in blue an experiment where the field was increased up to before domain rotation and then decreased to negative saturation and 2) in orange an experiment where the field was increased to positive saturation and then reduced to negative saturation.

center of the film rotated counterclockwise (orange line in Figure 12). The film was then moved 140 µms away from the center, where a negative field was applied through saturation and increased to zero (yellow line in Figure 12). The new location showed a different domain orientation before the negative field was applied. While it rotated clockwise as expected, given the domains rotated counterclockwise under a positive field, the rotation magnitude was not the same. When the same experiment was conducted in FeGd80Pt16 (dark blue and light blue lines in Figure 12), not only did the rotation magnitude change in the new imaging area, but it rotated the same direction rather than the opposite. These results imply the rotation is not uniform across the film. This could be connected to changes in strain across the window. Depending on the tension in the supporting silicon nitride membrane, the window may bow out. This could be

exacerbated as a magnetic field is applied, such that a bowed membrane could give rise to an in-plane magnetic field component. Varying strain across the film can also affect the local magnetic domain morphology and microstructure [73], [74]. In order to minimize these effects during the experiments, the first area imaged was roughly in the center of the chip window, found by locating two opposite corners of the square window and then moving to the middle point between them.

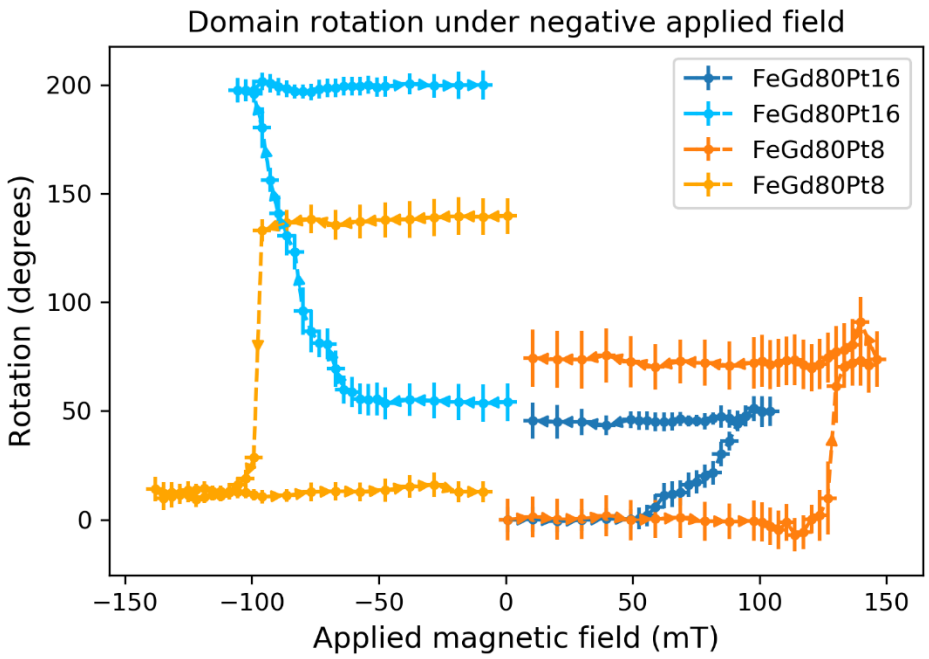

Figure 12: Rotation of Stripe Domains in Different Regions Across the Film
Domain rotation as a function of applied magnetic field for FeGd80Pt8 (orange lines) and FeGd80Pt16 (blue lines). Dark blue and dark orange lines correspond to measurements taken in the center of the film. Light blue and light orange lines correspond to measurements taken after the dark line measurements after first moving the sample to a new imaging region.

The Barkhausen effect, in which magnetic domains in a ferromagnetic material move suddenly under an applied field due to the existence of pinned configurations [75], was also observed. Some of the experiments showed that the domains did not rotate uniformly in the field of view. Instead the domains bent as they rotated, as shown in

Figure 13 and Figure 14. Figure 13 shows LTEM images of FeGd80Pt16 as a positive field is increased to saturation and then decreased to 0, ordered left-to-right and top-to-bottom. The domains in the top left corner, highlighted by a red box, maintain their initial orientation as the rest of the field of view rotates, causing the domains to bend sharply until -87 ± 4 mT, at which point the stubborn domains rotate and align with the rest of the

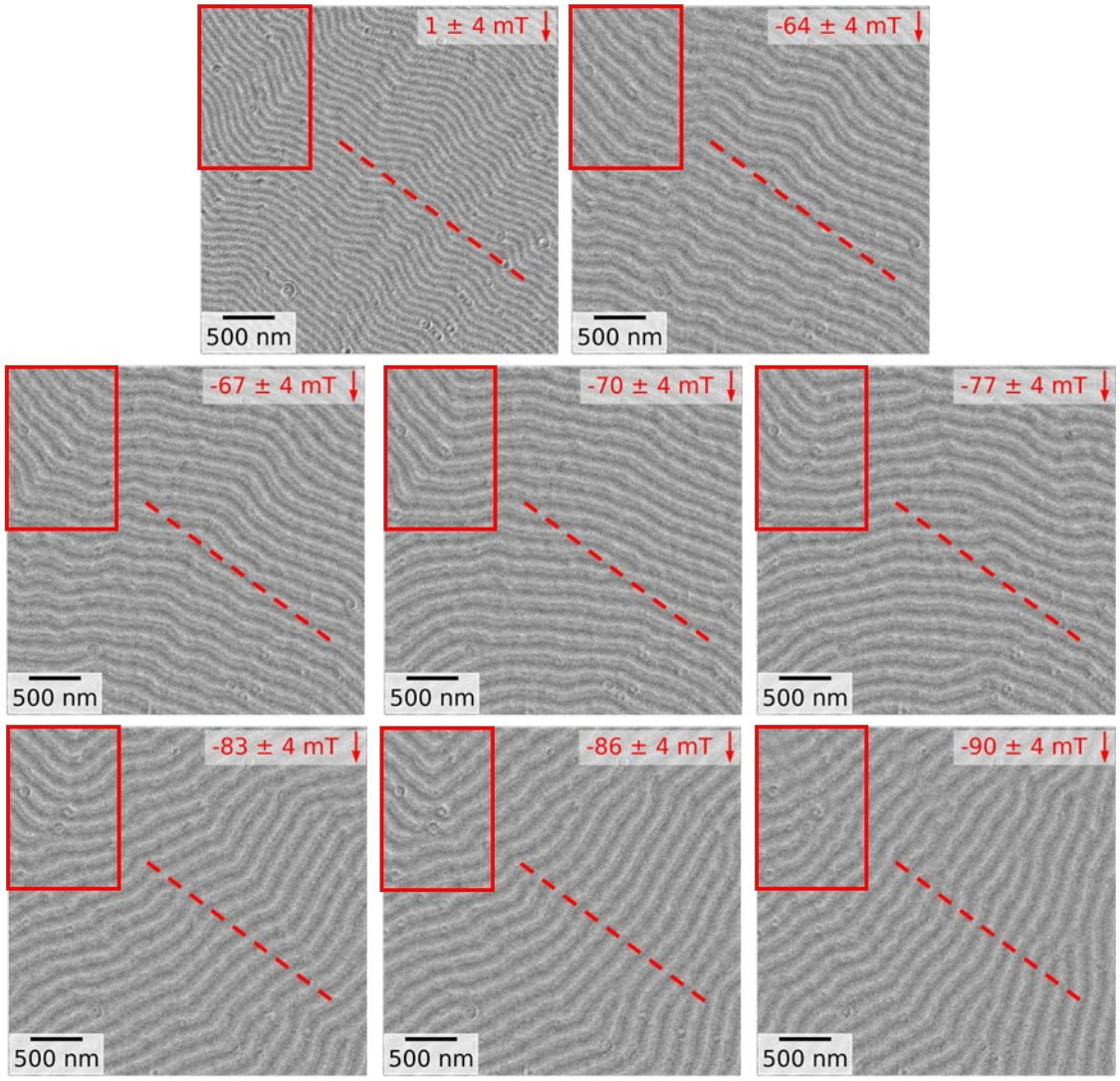

Figure 13: Non-Uniform Rotation Under an Applied Magnetic Field
Underfocused, background-subtracted LTEM images of FeGd80Pt16 under an out-of-plane applied magnetic field, ordered left-to-right and top-to-bottom. The applied field strength in mT is in the top right corner. A red arrow indicates if the field is being increased or decreased. The original domain wall orientation is shown by a red dashed line. An area of the sample that does not initially rotate with the rest of the field of view is indicated by a red square.

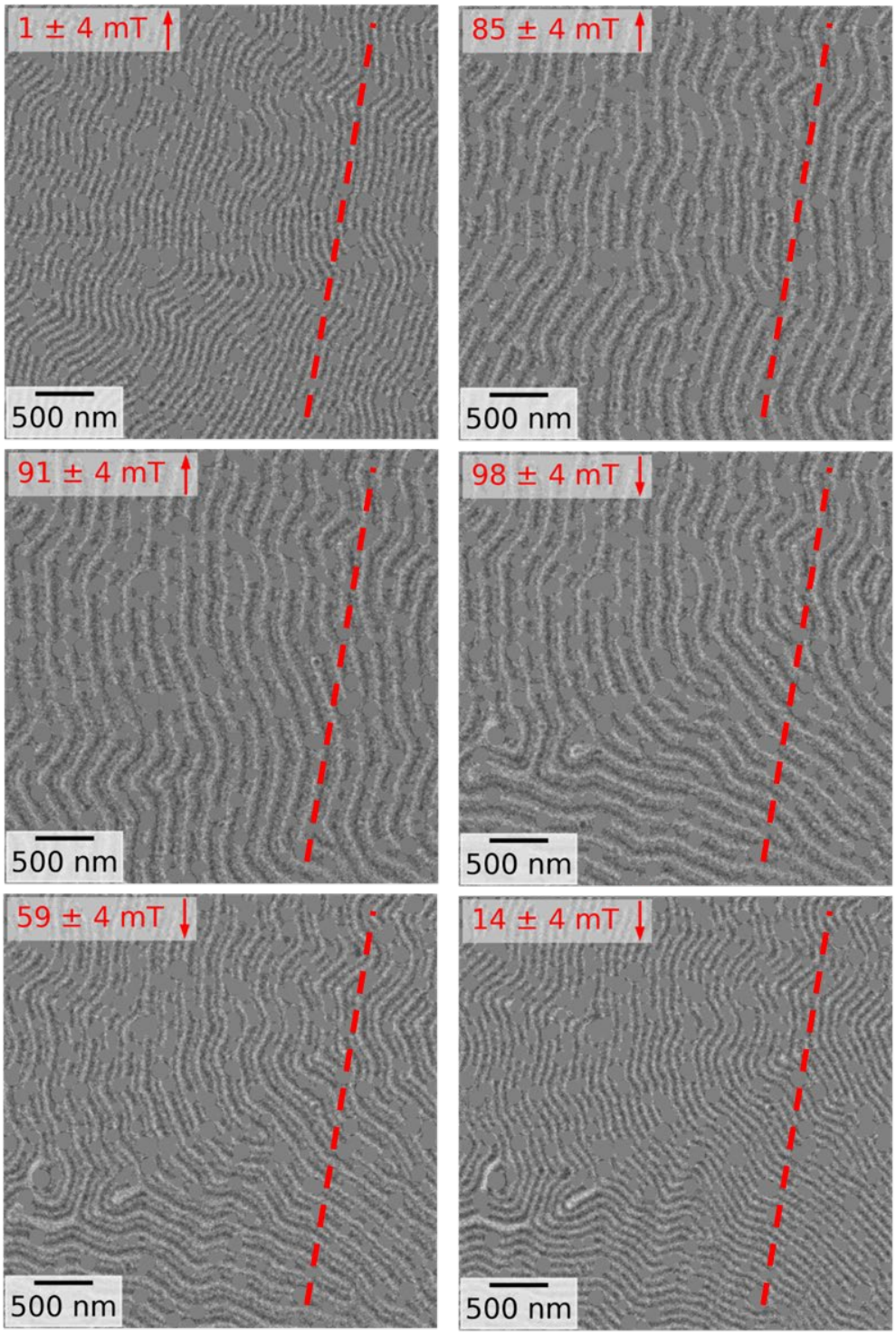

Figure 14: Non-Uniform Domain Wall Rotation under an Applied Magnetic Field Underfocused, background-subtracted LTEM images of FeGd80Pt8 under an out-of-plane applied magnetic field, ordered left-to-right and top-to-bottom. The applied field strength in mT is in the top left corner. A red arrow indicates if the field is being increased or decreased. The original domain wall orientation is shown by a red dashed line.

field of view. Figure 14 shows LTEM images of FeGd80Pt8 as the external magnetic field was increased up to the beginning of rotation and then reduced. The original orientation is indicated by a red dashed line. Once the applied field reaches 98 ± 4 mT, the domains in the bottom half of the field of view rotate. As the field is reduced to zero, the domains in the top half maintain the original orientation while the domains in the bottom half maintain their new orientation.

As a field is applied, the magnetic system will rearrange into the lowest energetic configuration possible, which causes the domain wall motion. Varying the relative number of Pt interfaces introduces different strengths of DMI, causing the material to have asymmetric Néel caps and to favor one chirality. Under positive and negative applied fields, the chirality distribution will be the same. The rotation is connected to the film reorienting to preserve the chirality distribution while also occupying the ground state. The discrepancies in rotation in different areas of the film could be due to local variation in the film structure or in the strain. If it is due to strain, it should be symmetric about the center of the window, where the substrate curvature is minimized. Repeating this experiment with more areas of the film could further clarify the source of the rotation variation. The change in rotation direction in the same area of the film (Figure 10) could be due to experimental error, either because the saturating fields used to reset the magnetic history between trials was not strong enough or the saturating field strength was changed. Attempting to reproduce the effect by varying the saturating field strength and observing the rotation direction could improve future experimental procedure. A full understanding of this behavior is the subject of ongoing research.

Conclusion

Fe/Gd/Pt films with varying numbers of Fe/Gd and Platinum layers were grown to explore the magnetic structure in broken symmetry films where ferromagnetic layers are interfaced with high spin-orbit coupling transition metals. We recorded the domain wall morphology as a function of applied magnetic field. We found that the domain walls rotate in-plane over a finite range of the applied field strength and stay in the new orientation when the field is brought back to zero. This rotation was found to be symmetric; if after bringing the applied field back to zero the field was then applied in the opposite direction, the domain walls rotated in the opposite direction and returned to their original orientation. However, while this rotation was observed across the film, it was not uniform, suggesting strain in the film or local variation in the film structure is affecting the magnetization.

An aspect of these films that this study did not explore is the emergence of a domain wall chirality preference. To determine the chirality of a domain wall, the out-of-plane component of the magnetization must be known. This typically cannot be measured by LTEM, but in studies of the evolution of magnetic domains in a film with perpendicular magnetic anisotropy under an applied magnetic field, the field history can be used to determine the out-of-plane component of the magnetization [76]. This was one of the goals of the experiment presented. However, rather than some domains obviously growing as a field was applied, the domains broke up into biskyrmions near saturation, making the identification of domains aligned with the applied field and those antiparallel to the applied field unclear. This issue might be resolved by imaging the sample at non-

normal incidence, yet this will require a modified specimen holder that can maintain a perpendicular field at the sample.

This study demonstrates the power of LTEM to drive theoretical understanding of micromagnetics. As one of only a few recent studies of materials with both dipolar interactions and DMI determining the magnetic structure, the measurements of unexpected variation within the domain wall and observation of the domain wall rotation are new pieces to this puzzle. These results also highlight that LTEM is complementary to other micromagnetic imaging techniques. X-ray measurements could not reveal variation within the domain wall Bloch component. At the same time, without X-ray measurements the LTEM results could have been misleading. Yet while Lorentz TEM is a useful technique and the simplest way to image magnetic materials in a TEM, it is an indirect measurement of the magnetic phase. There are two direct phase measurement techniques also used to image magnetic materials; differential phase contrast and off-axis electron holography. In the next chapter, I present the first use of diffraction-grating-based STEM holography, a direct phase measurement technique, to image magnetic materials. As discussed in the previous chapter, STEM holography could combine the pros of both direct-phase measurement techniques and be a new tool in the TEM magnetic imaging kit.

CHAPTER III

MAGNETIC PHASE IMAGING VIA STEM HOLOGRAPHY

Introduction

While electron microscopy has been able to directly image the atomic structure of materials since 1970 [46], the ability to image magnetic and electric fields at nanometer length scales has lagged far behind. There are two reasons for this. First, in typical high-resolution TEM imaging modes, the sample sits within the high magnetic field of the objective lens, and this alters the magnetic structure. A large segment of TEM development has focused on improving the objective lens and correcting for its aberrations as it contributes the highest aberrations to the optical system. As discussed in Chapter II, the objective lens is turned off to image magnetic materials. Without the objective lens, it is difficult to form a high-resolution TEM image or a high-resolution STEM probe at the sample. The second limitation to high resolution TEM imaging of magnetic fields is determined by the contrast mechanism. The most common magnetic TEM imaging modes, LTEM and DPC, are sensitive to gradients in the electron phase induced by internal fields within the sample. On short length scales, phase gradients can be quite small, resulting in low signal-to-noise. The resolution gap of TEM imaging set by these two factors limits the understanding and characterization of a magnetic material's physical and magnetic structure.

The first atomic resolution image of a sample in a magnetic-field free environment was accomplished in a STEM instrument using differential phase contrast (DPC) with a new objective lens design in 2019, although they did not report measurement of the magnetic field of the sample [24]. DPC measures the phase gradient

across the sample [13], [22], [23]. Because of this, DPC is inherently more sensitive to the larger and more rapidly varying changes in material structure than the comparatively smaller and more slowly varying changes in magnetic structure. In addition, the phase sensitivity worsens with higher spatial resolution [13], [77]. The other direct phase measurement technique used to image magnetic materials, off-axis electron holography [25]–[27], measures the phase of the sample, meaning it is sensitive to the electric and magnetic potentials rather than the electric and magnetic field as with DPC. However, magnetic imaging in TEM holography mode has not broken 5Å resolution [15], [18]. off-axis electron holography is also challenging to implement as it requires specialized and expensive instrumentation, extremely high coherence electron sources and very stable optics. STEM holography, on the other hand, is an interferometric probe-based technique that directly measures the phase. Unlike DPC, the phase sensitivity does not worsen with improved spatial resolution. Unlike TEM holography, STEM holography can be implemented using a modified aperture featuring a grating beamsplitter [32]–[34], [78], has loosened requirements on spatial resolution and optical stability, and has the additional advantage that it can be used simultaneously with other imaging modalities such as high-angle annular dark field, DPC, and energy dispersive spectroscopy imaging. Therefore, STEM holography could be the best of both worlds: a high resolution imaging technique for magnetic materials that measures the phase directly rather than the phase gradient, and thus the electromagnetic potentials instead of the fields. STEM holography was originally theorized and experimentally realized in the late 1980s through the early 1990s [28]–[31] using an electrostatic biprism to divide the electron beam. In this chapter

I present the first measurements of magnetic materials using STEM holography implemented with an amplitude-dividing diffraction grating.

Scanning Transmission Election Holography

In STEM holography, the electron beam is coherently divided into two beams by a diffraction grating installed in the aperture just below the 2nd condenser lens (C2 aperture) [32]–[34], as shown in Figure 15. The 1st and 2nd condenser lenses (C1 and C2 lenses) are represented by the first lens in Figure 15. The portion of the electron beam that passes through the diffraction grating is shown in blue. At the sample, the beams are focused to probes by the 3rd condenser lens (C3 lens). The diffraction grating is a pattern milled into a silicon nitride membrane using a focused ion beam [79]–[82]. The entire silicon nitride membrane is transparent to the electron beam and not filled by the grating. Electrons that pass through the unpatterned membrane surrounding the grating, shown in green below the C2 aperture in Figure 15, are removed by the aperture below the 3rd condenser lens (C3 aperture). The probes are scanned such that one of the probes, referred to as the interaction probe (the rightmost probe in Figure 15), interacts with the sample while the reference probe (the leftmost probe in Figure 15), passes

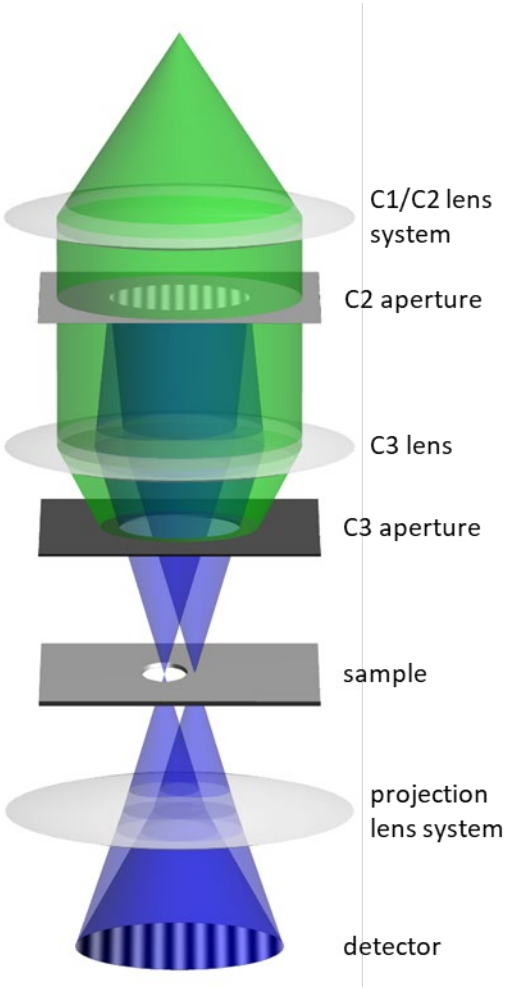

Figure 15: STEMH Optical System The lenses are indicated by grey ellipsoids. The electron beam is shown in green and blue.

through vacuum. The projection lens system defocuses the beams such that they overlap and interfere at the detector. The phase that the sample imparts on the interaction probe is determined from the image of the interference. To form an image of the sample, the probes are scanned and for each point in the scan the phase is calculated from the interference image.

The phase reconstruction from the interference images collected depends on the probe-producing grating, which creates multiple diffracted electron probe beams. The wavefunction of the electron immediately before interacting with the sample can be written as a coherent sum of each diffracted probe's wavefunction

$$\Psi_i(\vec{x};\vec{x}_0,\vec{x}_s) = \sum_m c_m a_m(\vec{x} - m\vec{x}_0 - \vec{x}_s) \tag{3.1}$$

where m is the diffraction order number, c_m is the complex amplitude of each probe, a_m is the wavefunction of each probe, $\vec{x}_0$ is the separation between probes, and $\vec{x}_s$ is the scan offset. Assuming the sample is a weak phase object, the electron wavefunction immediately after the sample is

$$\Psi_f(\vec{x};\vec{x}_0,\vec{x}_s) = \sum_m c_m a_m(\vec{x} - m\vec{x}_0 - \vec{x}_s)\, t(\vec{x}) \tag{3.2}$$

where $t(\vec{x})$ is the sample's transmission function. The interference pattern captured by the detector is written mathematically as the absolute value squared of the Fourier transform of the wavefunction after the sample:

$$I\left(\vec{k};\vec{x}_0,\vec{x}_s\right) = \widetilde{\Psi}_f^* \cdot \widetilde{\Psi}_f \tag{3.3}$$

where tilde indicates the 2D Fourier transform. The Fourier transform of this image then gives

$$\tilde{I}(\vec{u};\vec{x}_0,\vec{x}_s) = \sum_{m,n} c_m^* \, c_n [a_m^*(\vec{u} + m\vec{x}_0 + \vec{x}_s) t^*(\vec{u})] \otimes [a_n(-\vec{u} + n\vec{x}_0 + \vec{x}_s) t(-\vec{u})] \quad (3.4)$$

where $\otimes$ indicates a convolution. Assuming that the probe wavefunctions a_m are Dirac delta functions δ, this can be rewritten as

$$\tilde{I}(\vec{u};\vec{x}_0,\vec{x}_s) = \sum_{m,n} c_m^* \, c_n \delta(\vec{u} + (m-n)\vec{x}_0) \; t^*(\vec{u} - n\vec{x}_0 - \vec{x}_s) \; t(n\vec{x}_0 + \vec{x}_s) \quad (3.5)$$

Replacing $m - n$ with l so that the above equation becomes

$$\tilde{I}(\vec{u};\vec{x}_0,\vec{x}_s) = \sum_{l,n} c_{n-l}^* \, c_n \delta(\vec{u} - l\vec{x}_0) \; t^*(\vec{u} - n\vec{x}_0 - \vec{x}_s) \; t(n\vec{x}_0 + \vec{x}_s) \quad (3.6)$$

shows that the Fourier transform of the interference image produces a line of peaks at the same spacing as the probe spacing. The lth peak carries the sample transmission function information picked up by the probes that are l diffraction orders apart. The diffraction gratings used are designed to maximize amplitude in two probes and minimize any others, but more than two probes are always present. These weaker probes must be accounted for in STEMH experiments. For instance, for a grating that produces 5 diffraction orders (-2, -1, 0, +1, +2) the 1st order peak in the Fourier transform of the interference image carries the phase difference between the -2 and -1 probes, -1 and 0 probes, 0 and +1 probes, and +1 and +2 probes. Crucially, the magnitude of each contribution is controlled by the amplitude of the probes. So, if +1 and -1 are the strongest probes, the 1st order peak in the Fourier transform of the interference image will carry comparable contributions of 0/+1 and 0/-1 but the second order peak will be dominated by +1/-1. Assuming the *j*th peak is dominated by the interaction and reference probes, the sample's transfer function can be calculated via

$$t(\vec{x}_0 + \vec{x}_s) = \frac{1}{c_r c_i^*} \mathcal{FT}^{-1}\left[\frac{1}{\mathcal{FT}[|a_r|^2]}\right] \otimes \left[\int_\Omega a_r^*(\vec{u})\tilde{I}_j(\vec{u}; x_s) d\vec{u}\right] \quad (3.7)$$

where $c_r a_r(\vec{x})$ and $c_i a_i(\vec{x})$ are the reference and interaction probes respectively and $\int_\Omega$ indicates integrating around $\tilde{I}_j$, the jth peak in the Fourier transform of the interference image [32]–[34], [78], [83]. This calculation finds the transfer function for a given scan point x_s. To form a phase image, the interference image must be collected for each scan location. In this chapter, I will discuss applying this STEM holography technique to phase imaging magnetic domains within thin films.

Adapting STEM Holography to Image Magnetic Domains

The first demonstration of STEMH imaged a gold nanoparticle on amorphous carbon with 2.4 Å resolution [33]. To image magnetic materials, the objective lens must be turned off to minimize the magnetic field at the sample, a mode referred to as Low Mag STEM. This affects the optical system and experimental procedure in several ways. First, the beam forms a much smaller convergence angle at the sample, which places limits on spatial resolution. However, the TEAM I microscope at the Molecular Foundry, Lawrence Berkeley National Lab, the instrument used here and by Yasin et al, still achieves 8-10 nm resolution in this mode, estimated from the smallest features visible in the simultaneously-collected high-angle annular dark field image (HAADF). In addition, for a given diffraction grating periodicity, decreasing the strength of the main objective lens favorably creates a much larger probe spacing at the sample. In standard STEMH experiments using a full strength objective lens setting, a probe separation of 10s of nms is possible [33]. In Low Mag STEMH the probe separation can be as large as 2 μms. This allows larger scans of the sample to be taken. The width of the scan in the direction along

the line of the beams is limited by the probe separation because the phase reconstruction requires that while the interaction probe passes through the sample the reference probe must pass through vacuum.

In standard STEM operation, the selected area aperture below the sample is in an image plane of the sample. The aperture can be used to block probes before the interference is formed at the detector. Yasin et al. used this to block high-order probes and high-angle scattering to reduce noise. In principle, the aperture could be used to limit the probes to only the interaction probe and one reference probe, eliminating concerns of multiple interferometer paths contributing to the reconstructed phase. However, in Low Mag STEM the selected area aperture is in a Fourier plane of the sample. An image of the interference is formed at the aperture, and it cannot be used to block some of the probes selectively.

The inability to remove unwanted probes with an intermediate aperture requires the use of tailored phase gratings that produce just two diffraction orders. A focused ion beam provides a way to fabricate nanoscale diffraction gratings with engineered phase profiles [79], [80], [82], [84]. However, various factors of the milling process result in a tradeoff between lateral feature size and control over the depth of the feature. In many STEMH applications, the smallest possible grating period is desired to allow for a larger probe spacing and hence larger possible scan area, and this prioritization comes with the cost of reduced diffraction efficiency set by the depth of grooves in the grating. In Low Mag STEMH the prioritization is reversed – probe spacing is inherently so much larger that a larger grating periodicity can be used, allowing the fabrication of grating features

with tailored depths. This allows for more accurate gratings to be produced, especially when used in combination with gas-assisted etching [82].

Imaging Landau States in a Permalloy Square

The first magnetic sample imaged with STEMH was a permalloy square. Permalloy is a nickel-iron magnetic alloy composed of approximately 80% nickel and 20% iron invented in 1914 [85]. Due to its high magnetic permeability, low coercive force and low magnetic loss, it is useful in many applications, such as electrical current sensors, magnetic shields and cores of magnetic heads for card readers. The magnetic structures in nanoscale patterned Permalloy elements and their dynamics is a long-standing and still active area of research [86]–[89]. In addition, Permalloy has become a frequent test subject for the demonstration of developments in magnetic imaging in a TEM [13], [53], [90], [91].

The sample was fabricated by first depositing approximately 20 nm of permalloy composed of 80% nickel, 15% iron, and 5% molybdenum onto a 100 nm thick silicon nitride membrane via thermal evaporation. Isolated squares approximately 1-1.5 μm wide attached to the surrounding membrane by 100-200 nm wide tethers at its corners were created by milling out the surrounding holes via focused ion beam, as shown in Figure 16a and b. Isolated micron-scale squares of permalloy form Landau domains; Domain walls along the diagonals of the square break up four triangular domains in which the magnetization is parallel to the square edge [92]. Micromagnetic simulation using the Object Oriented Micromagnetic Framework [93] shows that in the tethered square, the domain walls do not follow the diagonals of the square but instead are offset to the side of the tether, as shown in Figure 16c. The magnetic phase, given by the integral over the

magnetic vector potential component parallel to the optic axis, can be written in terms of the magnetization using the following relation between the 3D Fourier transform of the vector potential and the magnetization [94]–[96]:

$$\mathcal{F}_{3D}[A_z](k_x, k_y, k_z) = -\frac{i\mu_0 M_s}{2\pi} \frac{\mathcal{F}_{3D}[m_x(x,y,z)]k_y - \mathcal{F}_{3D}[m_y(x,y,z)]k_x}{k_x^2 + k_y^2 + k_z^2} \tag{3.8}$$

where μ_0 is the permeability of free space, M_s is the saturation magnetization of the sample, and m_x and m_y are the normalized magnetization vector components. The 2D Fourier transform of the phase is then

$$\tilde{\phi}(k_x, k_y) = -\frac{i\mu_0 e M_s}{2\pi\hbar} \frac{k_y \widetilde{\overline{m_x}} - k_x \widetilde{\overline{m_y}}}{k_x^2 + k_y^2} \tag{3.9}$$

where $\widetilde{\overline{m_x}}(x,y)$ and $\widetilde{\overline{m_y}}(x,y)$ are the Fourier transform of the integrals of $m_x(x,y,z)$ and $m_y(x,y,z)$ over z. Assuming the magnetization is uniform in z and the sample thickness is t, this is simplified to

$$\tilde{\phi}(k_x, k_y) = -\frac{i\mu_0 e t M_s}{2\pi\hbar} \frac{k_y \tilde{m}_x - k_x \tilde{m}_y}{k_x^2 + k_y^2} \tag{3.10}$$

where $\overline{m_x} = t m_x(x,y)$ and $\overline{m_y} = t m_y(x,y)$. The magnetic phase calculated from the magnetization simulation is shown in Figure 16d. The phase increases linearly from each edge to the crossing point of the magnetic domain walls. When a counter-clockwise-winding Landau domain is imaged by LTEM in an underfocused condition, bright lines appear along the domain walls with a brighter spot at their crossing point, as shown by the simulated LTEM image in Figure 16e. If the magnetization winds clockwise instead, the phase decreases towards the center and dark lines are formed in an underfocused LTEM image.

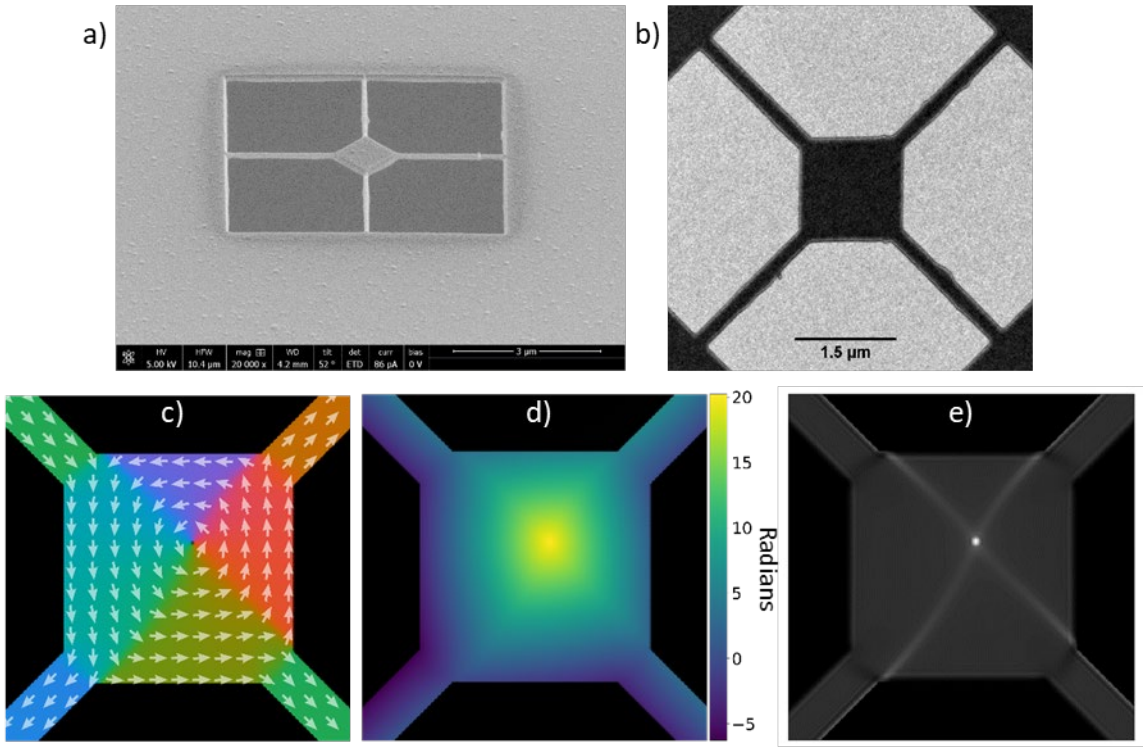

Figure 16: Tethered Permalloy Squares
a) Scanning Electron Microscope image of a tethered square milled into a permalloy-coated silicon nitride membrane viewed at an angle. The darker regions are areas where the film has been completely removed. b) An in-focus LTEM image of a tethered square. The lighter regions indicate holes in the sample. c) The magnetization in the tethered permalloy square calculated via OOMMF (direction and magnitude are indicated by the hue and saturation respectively). d) The electron phase imparted on the beam by the calculated magnetization. e) A simulated underfocused LTEM image of the calculated magnetization.

The magnetic structure of the fabricated tethered squares was confirmed by LTEM. The characteristic bright spot formed by a counter-clockwise-winding Landau domain (Figure 17a) can be seen in the experimental images of three different tethered squares (Figure 17b-d). The fainter domain walls are more difficult to see in the experimental images. Interestingly, while the center of the Landau domain appears off-center as predicted by the micromagnetic calculation in two of the images (Figure 17b and d), it appears centered in the third (Figure 17c). This serves as an example that even simple magnetic systems can display many different metastable configurations.

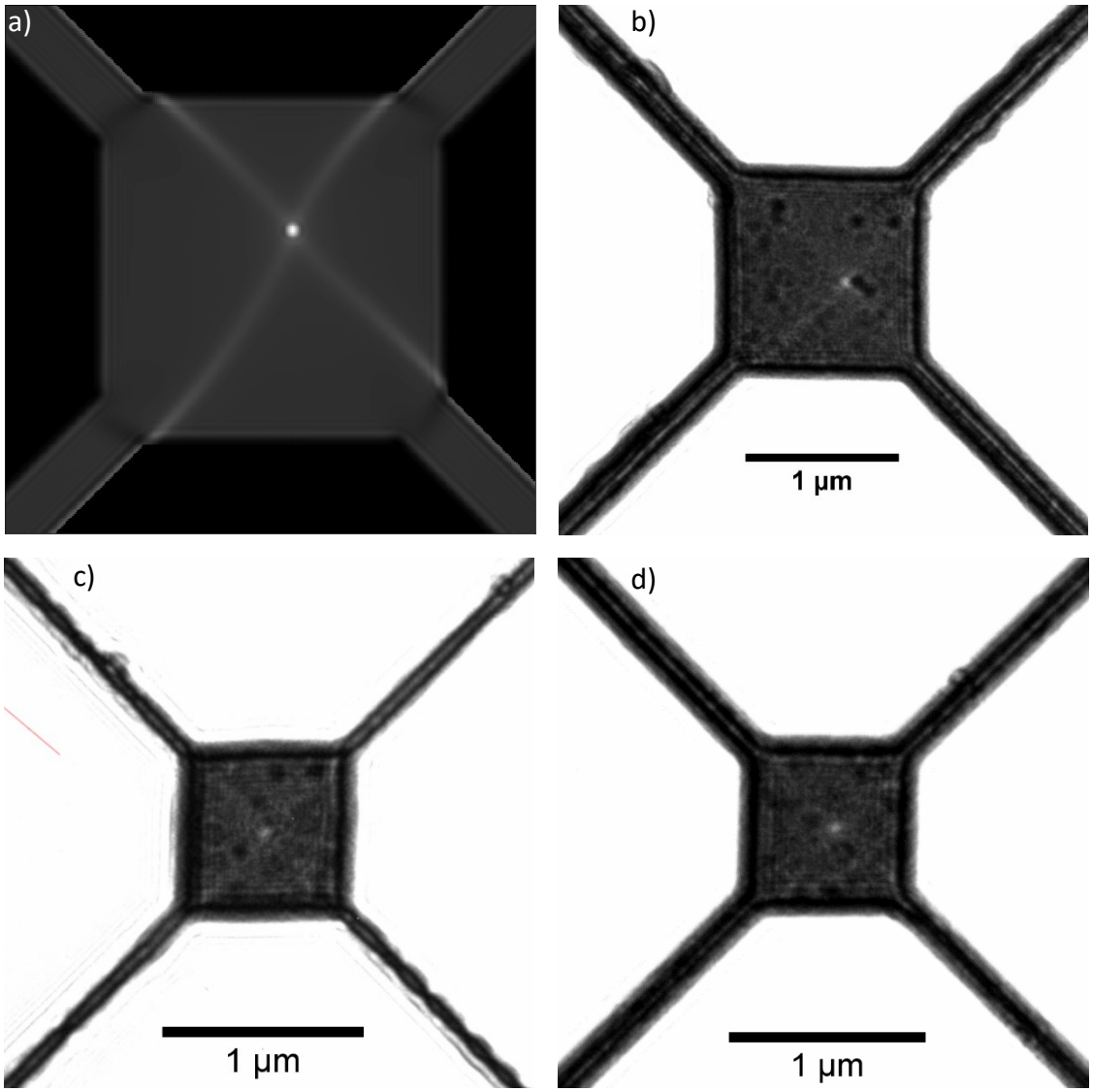

Figure 17: LTEM images of Tethered Permalloy Squares
a) A simulated LTEM image of a Landau domain in a tethered square. b)-d) Experimental underfocused LTEM images of three different tethered permalloy squares showing contrast corresponding to a Landau domain.

The first STEMH measurement of a permalloy tethered square used a sinusoidal grating that produced three probes of almost equal intensity, shown in an image of the probe pattern (Figure 18a) and the intensity profile through the center of the probes (Figure 18b). A HAADF image (Figure 18c) shows the overlapping images formed by the three probes. (Unlike TEM images, brighter regions of a HAADF image correspond

to the beam interacting with the film and darker regions indicate it passing through vacuum.) The HAADF image is formed by scanning the probes left to right across the field of view. Therefore, the rightmost probe interacts with sample first and forms the leftmost image. While the +1 probe is interacting with the square, forming the leftmost image, the -1 probe is still interacting with the surrounding membrane, as shown by the edges of the rightmost image. Because of this the STEMH measurement was instead performed with the 0^{th} order probe interacting with the sample while the +1 and -1 probes passed through vacuum. The scan area corresponding to this measurement is indicated by a red box in Figure 18c.

The STEMH measurement of the phase of a tethered permalloy square is shown in Figure 19a. Because the ± 2 probes are negligible, the phase was calculated using the +1 peak in the FFT of the interference images. A line profile through the center of the measured phase (Figure 19b) shows that the phase decreases towards the center of the square, as expected from a Landau domain configuration that winds clockwise.

Note that the magnetic phase appears to be stepped instead of continuous. A simulated LTEM image (Figure 19c) shows that this stepped phase would produce concentric bright and dark rings about the center of the square. This contrast could be formed by in-plane domain walls separating out-of-plane domains or the in-plane magnetization varying from pointing parallel to the square edge to pointing perpendicular to it. However, both scenarios would cost more energy than the Landau-domains observed by LTEM and are probably not physical. The SEM (Figure 16a) and simultaneously-collected HAADF (Figure 19e) images do not show any stepped variations in the thickness of the material, so it is unlikely that it is due to any

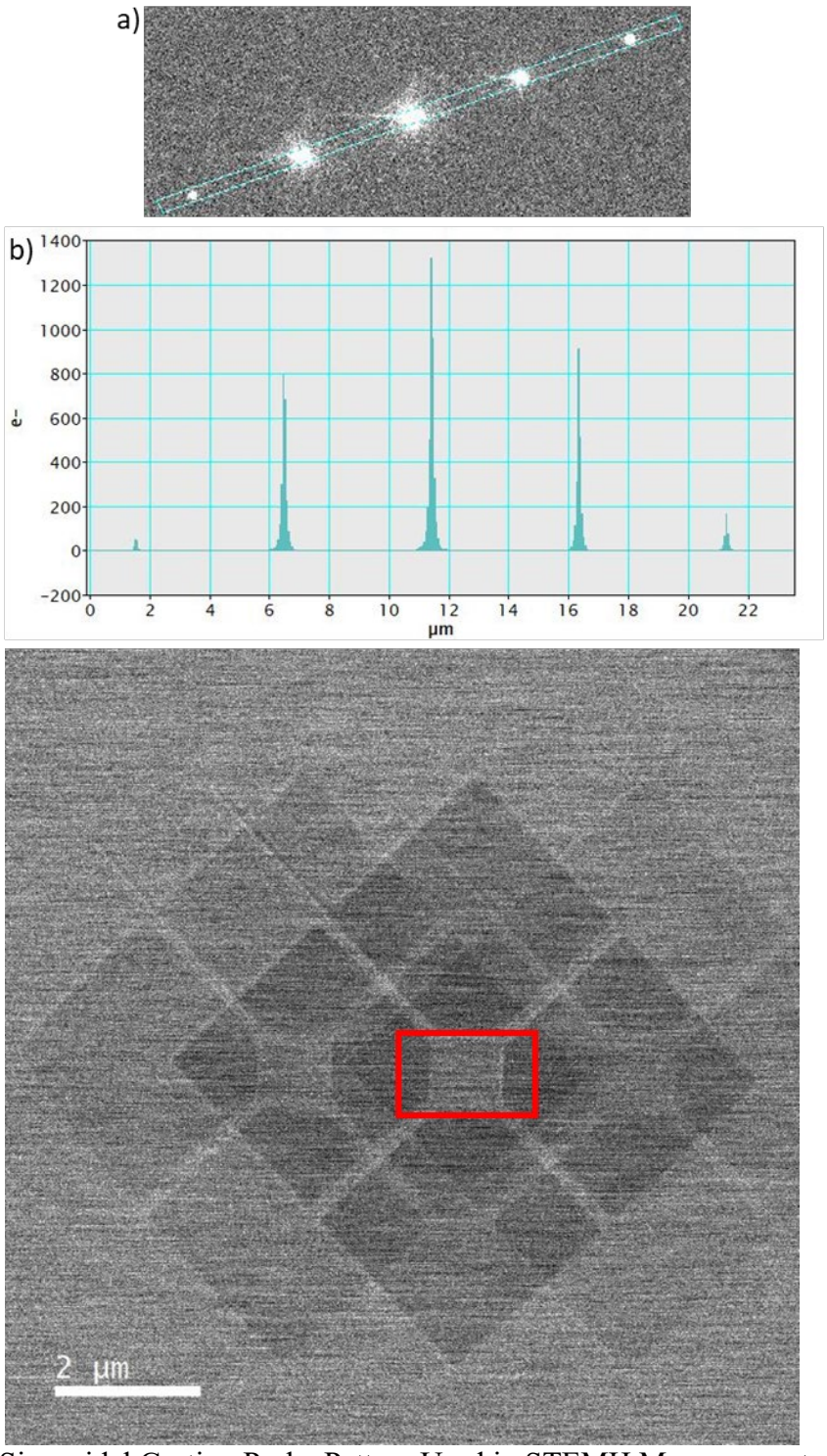

Figure 18: Sinusoidal Grating Probe Pattern Used in STEMH Measurement of a Tethered Permalloy Square

a) A TEM image of the probes. The blue box indicates the area used to produce a line profile (b) of the intensity summed over the width of the box. c) A HAADF image showing the overlapping images formed by the three most prominent probes. The red box indicates the area over which a STEMH measurement was performed.

electrostatic phase variation. The stepped phase is likely an artifact caused by using the 0^{th} order beam as the interaction probe. The +1 and -1 probes could not be used in this instance due to insufficient vacuum space for the reference probes. The phase was calculated from the +1 peak in the FFT of the interference images, which contains contributions from both the +1/0 probe phase difference and the -1/0 probe phase difference. These are almost exactly equal and opposite, resulting in flat regions in the measured phase when the contributions cancel. If the phase is smoothed to reduce the step-like appearance, the calculated magnetic field appears to be a clockwise Landau domain (Figure 19d).

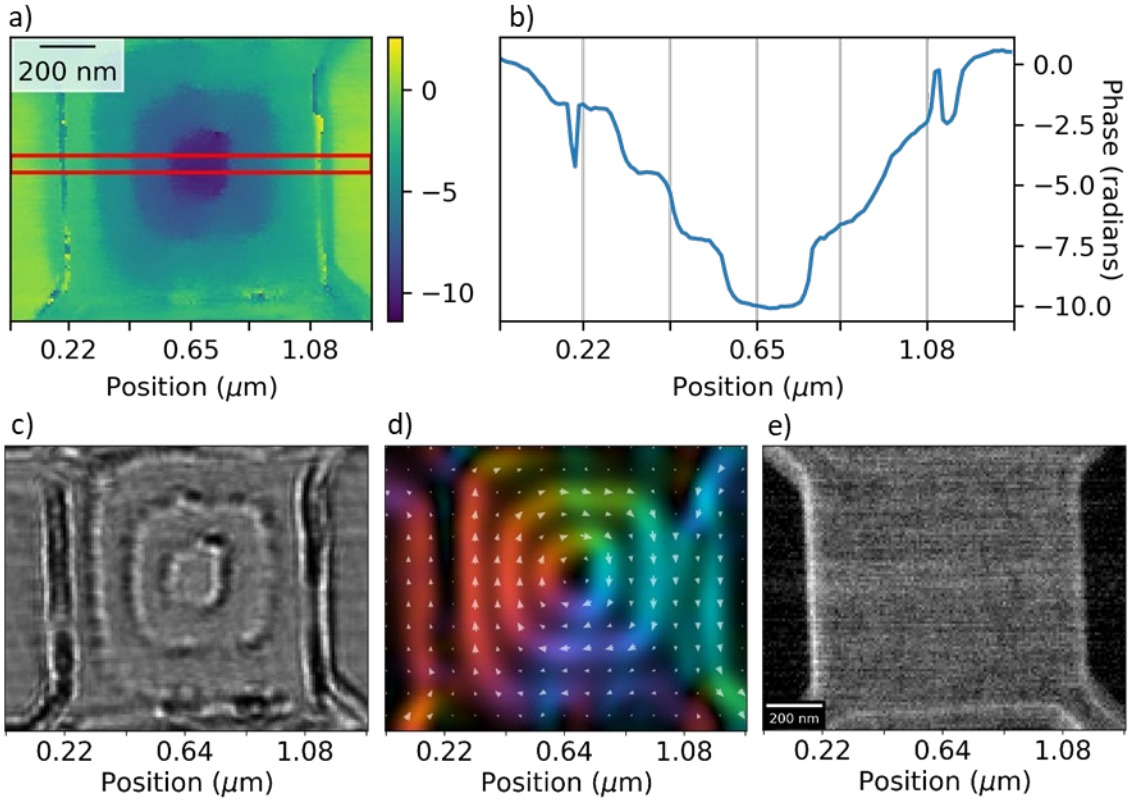

Figure 19: STEMH Phase Measurement of a Tethered Permalloy Square
a) The phase measured via STEMH in radians. b) The phase profile through the center of the phase pyramid, averaged in the *y*-direction between the red lines on the phase image. c) A simulated under-focused LTEM image of the measured phase. d) The magnetic field calculated from the measured phase after Gaussian smoothing (direction and magnitude are indicated by the hue and saturation respectively). e) Simultaneously acquired HAADF image.

A second STEMH measurement of a permalloy tethered square was performed using a binary grating that produced just two primary probes. Larger channels were cut out of the permalloy-coated membrane via FIB, extending the vacuum region around the tethered squares as shown in Figure 20c. The use of a binary phase grating caused the +1 and -1 probes to have the largest intensity, as shown in an image of the probes (Figure 20a) and the intensity profile through the center of the beams (Figure 20b). While the 0, ±2, and ±3 probes are still visible in the image of the probes (Figure 20a), the +2 peak in the FFT of the interference images will be dominated by the +1/-1 probe phase difference, allowing for the calculation of the phase of the sample. The relative intensity difference is clear in the overlapping HAADF image (Figure 20c), in which the images formed by the ±1 probes are most clearly visible. The STEMH measurement was performed with the -1 probe interacting with the sample (indicated by a red box in Figure 20c). The expanded holes in the film allowed for the 0, +1, ±2, and ±3 probes to pass through vacuum during the scan.

The flat intensity across the square in the simultaneously acquired HAADF image (Figure 21c) confirms that the permalloy square has uniform thickness and composition. Therefore, any phase variation in the square is assumed to be magnetic. The phase increases towards the center, shown in the phase image (Figure 21a) and the phase profile through the center of the square averaged between the red lines on the phase image (Figure 21b). This is expected from a counter-clockwise-winding Landau domain. However, there are less-than-2π discontinuities, visible as concentric lines in the phase image (Figure 21a). The concurrently-collected HAADF image shows small features on the order of 10 nm across that are visible in the STEMH phase image (highlighted by a

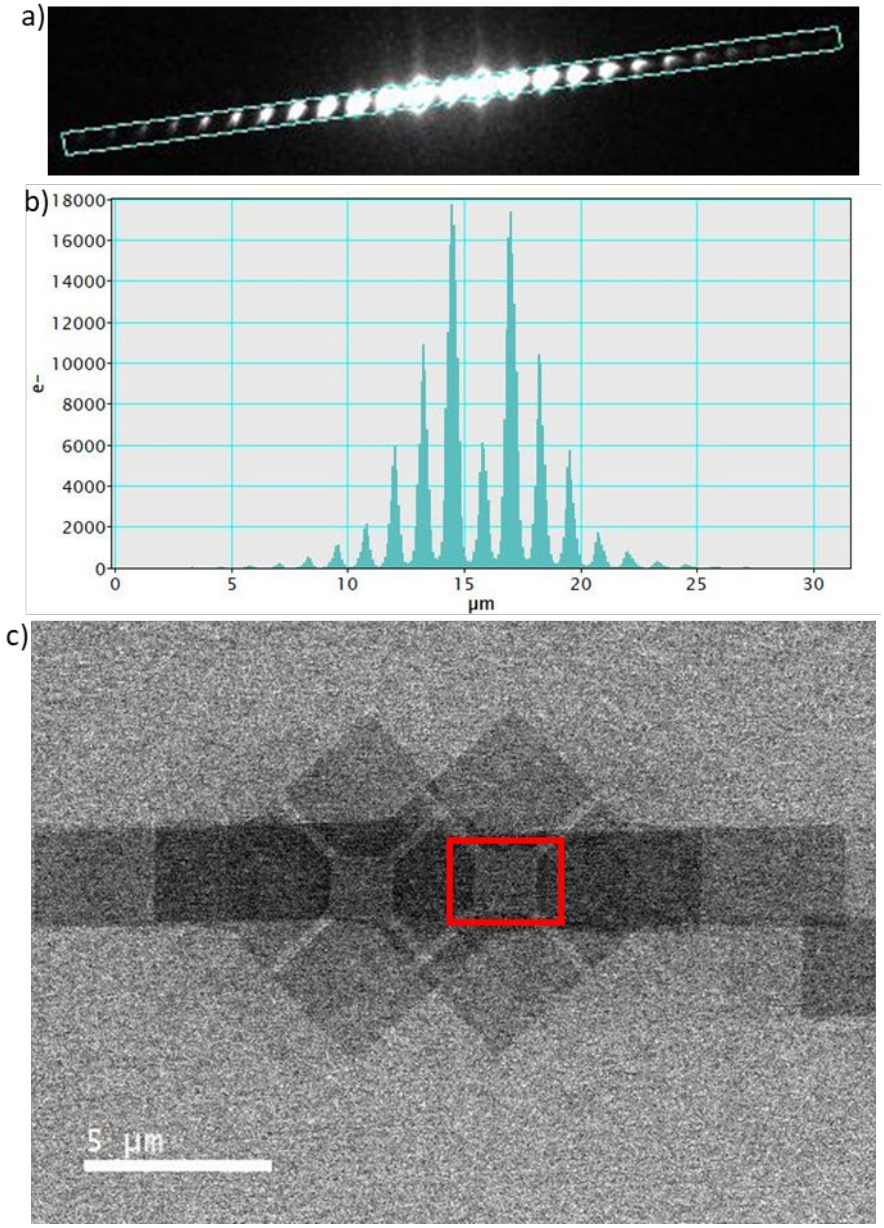

Figure 20: Binary Grating Probe Pattern Used in STEMH Measurement of a Tethered Permalloy Square
a) A TEM image of the probes. The blue box indicates the area used to produce a line plot (b) of the intensity summed over the width of the box. c) A HAADF image showing the overlapping images formed by the probes. The red box indicates the area over which a STEMH measurement was performed.

red circle in Figure 21a and c but these do not appear to correlate spatially with the small discontinuities in the measured phase. The phase discontinuities are most likely artifacts due to the 0/+2 and 0/-2 phase differences interfering with the +1/-1 phase measurement.

If the phase is smoothed to reduce these discontinuities, the calculated magnetic field appears to be a counter-clockwise Landau domain (Figure 21d). Further optimization of the beamsplitting gratings is required to eliminate these discontinuities.

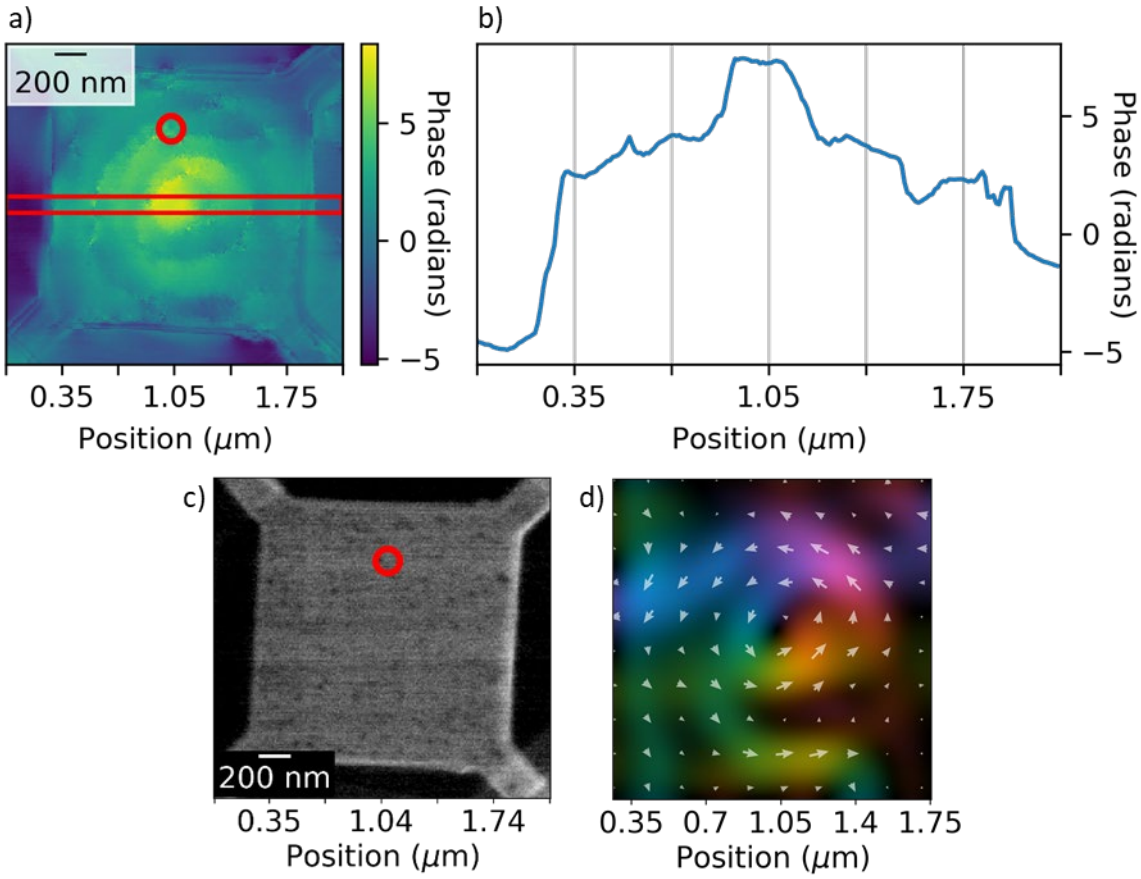

Figure 21: STEMH Phase Measurement of a Tethered Permalloy Square
a) The phase measured via STEMH in radians. b) The phase profile through the center of the phase pyramid, averaged in the *y*-direction between the red lines on the phase image. c) Simultaneously acquired HAADF image. d) The magnetic field calculated from the measured phase after Gaussian smoothing (direction and magnitude are indicated by the hue and saturation respectively).

These STEMH measurements of tethered permalloy squares serve as the first demonstration of an interferometric STEM image of the magnetic structure in a thin film. However, they also highlight how multiple reference probes can create artifacts in the reconstructed phase. The issue of ambiguity in the phase measured by STEMH will be further discussed later in the chapter.

Imaging Skyrmions in Fe/Gd Multilayer Thin Films

Magnetic skyrmions are donut-shaped magnetic domains. An example of a Bloch-type skyrmion, which has magnetization that points azimuthally in a circle, is shown in Figure 22a. This imparts a bump in the phase of the electron wave, as shown in Figure 22b. The sign of this bump depends on which way the Bloch skyrmion winds, i.e. the handedness. In underfocused LTEM images this phase creates a dark spot surrounded by a bright ring, as shown in Figure 22c. If the Bloch skyrmion wound counterclockwise, the spot would be bright instead. Skrymions are topological solitons; they move and interact like particles. Because of this, their topological stability, and the low current threshold needed to move them through a material, there is interest in using skyrmions as nanoscale information carriers [2]–[4]. Subsequently, producing materials that support skyrmions and understanding their behavior has become a popular field of research. They also serve as an example for the need for improved spatial resolution and contrast in magnetic imaging as they can be as small as 1nm [97]. One of the materials that supports magnetic skyrmions is a thin film composed of 120 bilayers of iron and gadolinium. This multilayer thin film has been previously shown to produce a lattice of skyrmions under an

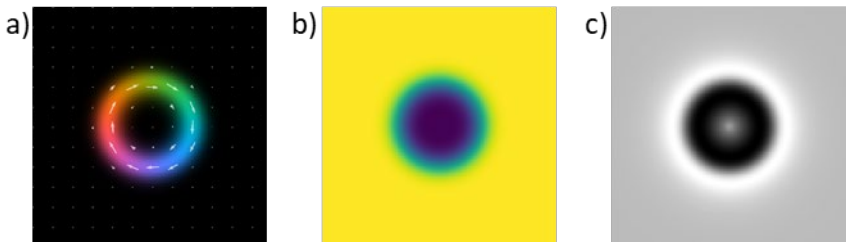

Figure 22: Bloch-type Magnetic Skyrmion
a) Visualization of the in-plane magnetization of a Bloch-type skyrmion (direction and magnitude are indicated by the hue and saturation respectively). b) The simulated phase imparted on an electron beam in a TEM by a Bloch-type skyrmion. c) A simulated underfocused LTEM image of a Bloch-type skyrmion.

applied magnetic field perpendicular to the film [39]. Here we image skyrmions in an Fe/Gd film via STEMH.

To perform STEMH there must be a hole in the sample for the reference beam to pass through. To provide this, an Fe/Gd multilayer film with composition [Pt (3nm)\ [Fe(3.4A)/Gd(4A)]x120\ Pt (3nm)], with a nominal total thickness of 89 nm, was deposited on a 50 nm thick silicon nitride membrane pre-patterned with a grid of 20 μm holes by Sergio Montoya at UCSD using sputter deposition. These membranes, commonly used as electron-transparent support films for imaging TEM samples, are referred to as "holey" silicon nitride, and the hole-patterning process likely adds non-uniform stress within the thin film. Lorentz TEM images of the Fe/Gd film deposited on these membranes show that the film forms stripe domains with no magnetic field applied. These remanent stripe domains tend to line up with local edges of the holes, likely due to surface effects and internal stress, and in between the holes these stripe domains meet and become frustrated. An example is shown in Figure 23a. The clearer white lines indicate there is an in-plane component of the magnetization. This is most likely due to the magnetic material being under strain as the nonuniform holey silicon nitride relaxed during the deposition process. Under an applied field, a mixture of skyrmions and other magnetic bubbles forms rather than a skyrmion lattice, as shown in Figure 23b. The low contrast makes these features difficult to identify. Near the edge of the holes, these magnetic domains become more sparse, as shown in a LTEM image of the film under an applied field next to an edge (Figure 23c). The edge is just outside the top left corner of the field of view.

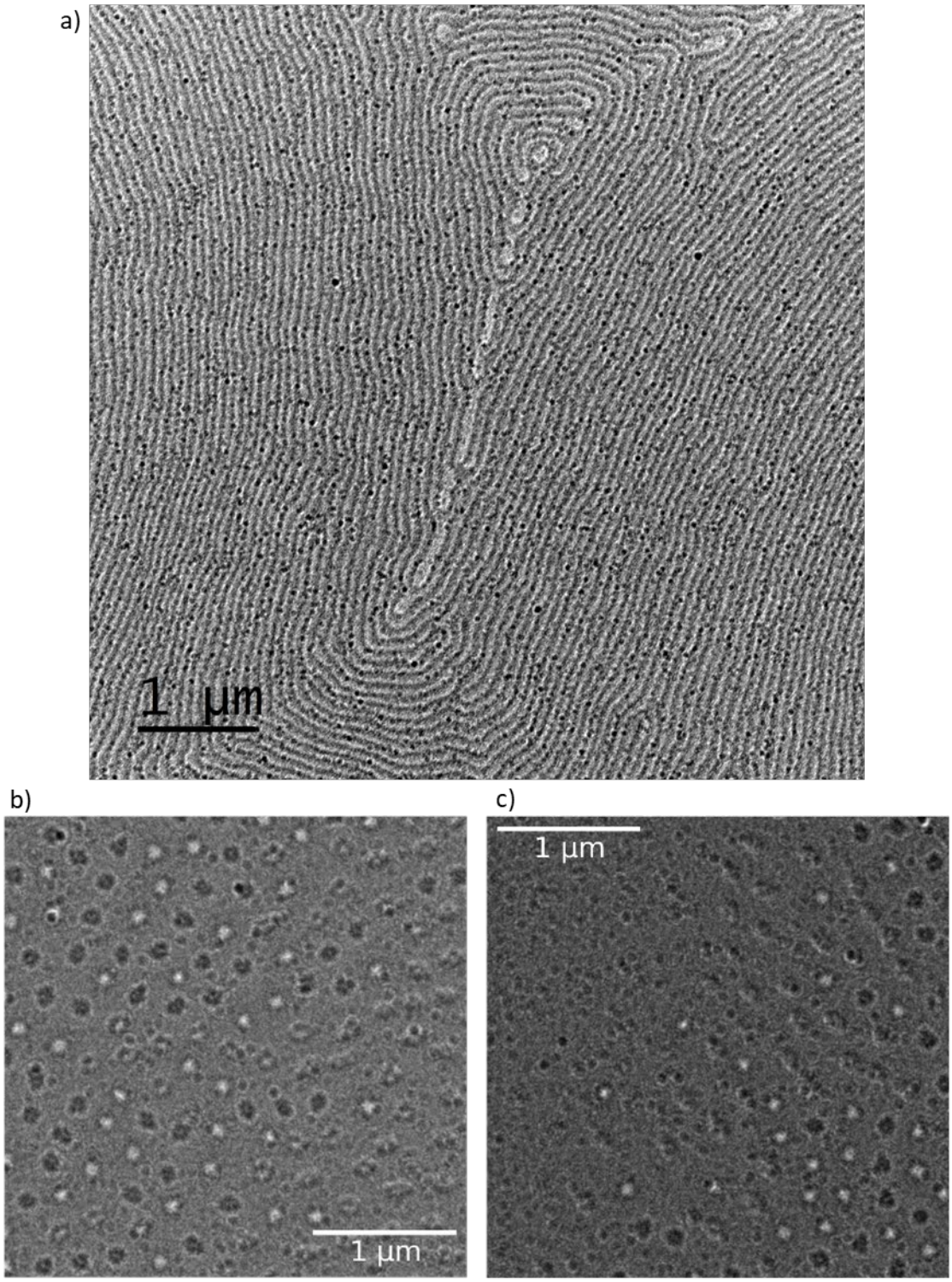

Figure 23: LTEM images of Fe/Gd film Grown on Holey Membrane
a) LTEM image of an area between 4 holes with no applied field. b) LTEM image of skyrmions, bubbles, and biskyrmions under an applied field. c) LTEM image of mixed states under an applied field close to an edge (just outside the top left corner of the field of view).

The interaction probe must be scanned along one edge of the sample so that the reference can pass through vacuum. A blazed phase grating producing an asymmetric diffraction pattern was used as a beamsplitter. This eliminated the +1, +2 and +3 probes, as shown in the image of the probes (Figure 24a) and the intensity profile through the center of the probes (Figure 24b), making it possible to scan the sample with the most intense probe, the 0^{th} order, while all other significant probes pass through vacuum. Unfortunately, imperfections in this grating aperture produced more than two distinctly predominant probes, which can lead to artifacts in the recorded phase as discussed above. The phase of the sample was measured using the +1 peak in the Fourier transform of the interference image, which is dominated by the -1/0 probe phase difference. The HAADF image (Figure 25a) shows the thickness varies at the film edge, but it does not appear to vary across the rest of the field of view. The sample was imaged under a magnetic field created by weakly exciting the objective lens to produce skyrmions. The formation of skyrmions was confirmed by defocusing the probe and forming an LTEM-like image.

STEMH phase measurements of two different areas of the film are shown in Figure 25b. Both show a large-scale phase variation. This is potentially due to there being a remaining in-plane magnetization component, as discussed earlier. In both phase measurements there are also smaller features that are the size we expect of skyrmions in this sample. Subtracting out the large-scale variation to isolate these smaller features, as shown in Figure 25c, they appear to be phase bumps due to skyrmions. Calculating the magnetic field from these phase features, they have the skyrmion vortex-like Bloch structure, as shown in Figure 25d. We attribute the elongated shape of the structures to the effects of local stress in the membrane. While structural defects in the patterned

silicon nitride membrane are visible in the LTEM images as small dots (Figure 23), they are all 20-50 nm across so it is unlikely the phase variations in the STEMH measurement are electrostatic.

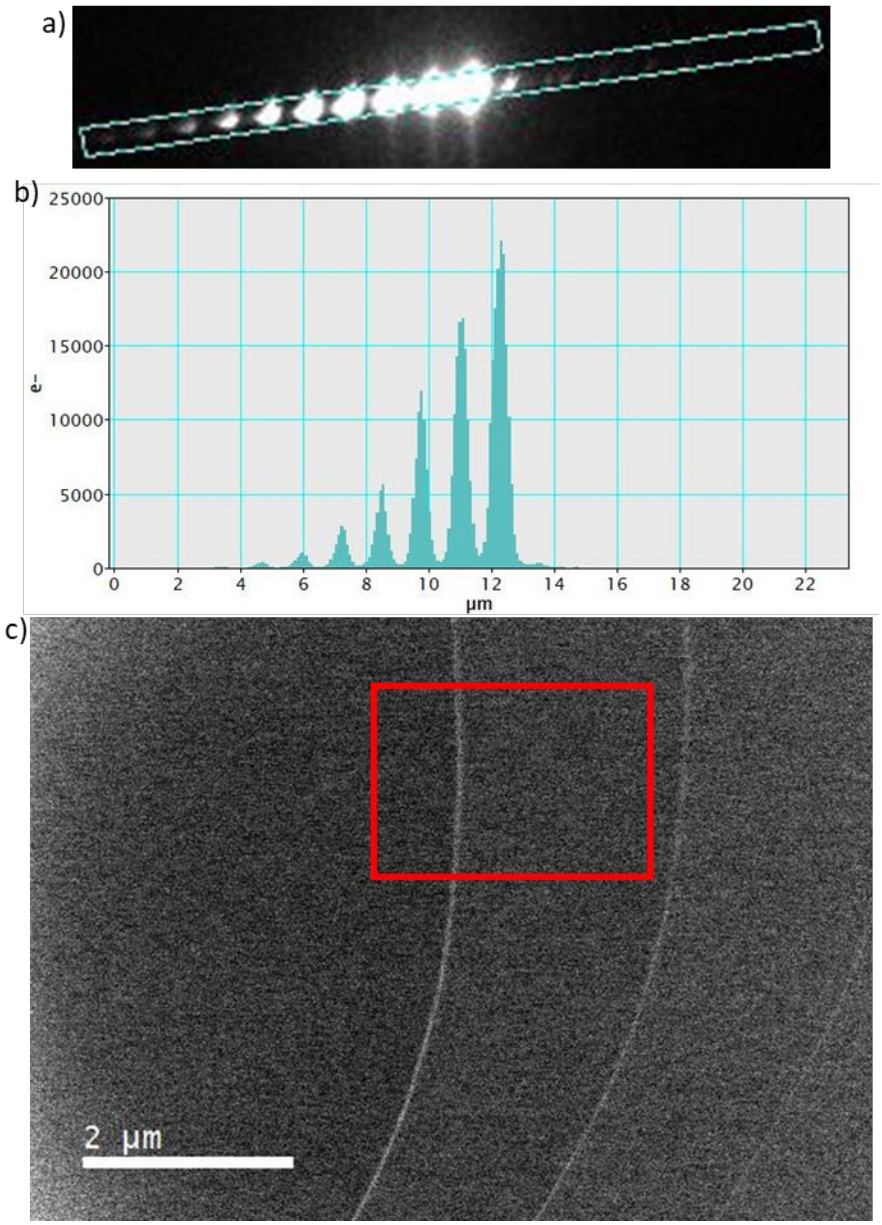

Figure 24: Blazed Grating Probe Pattern Used in STEMH Measurement of a FeGd thin film
a) A TEM image of the probes. The blue box indicates the area used to produce a line profile (b) of the intensity summed over the width of the box. c) A HAADF image showing the overlapping images of the edges of a hole in the film formed by the three most prominent probes. The red box indicates the area over which a STEMH measurement was performed.

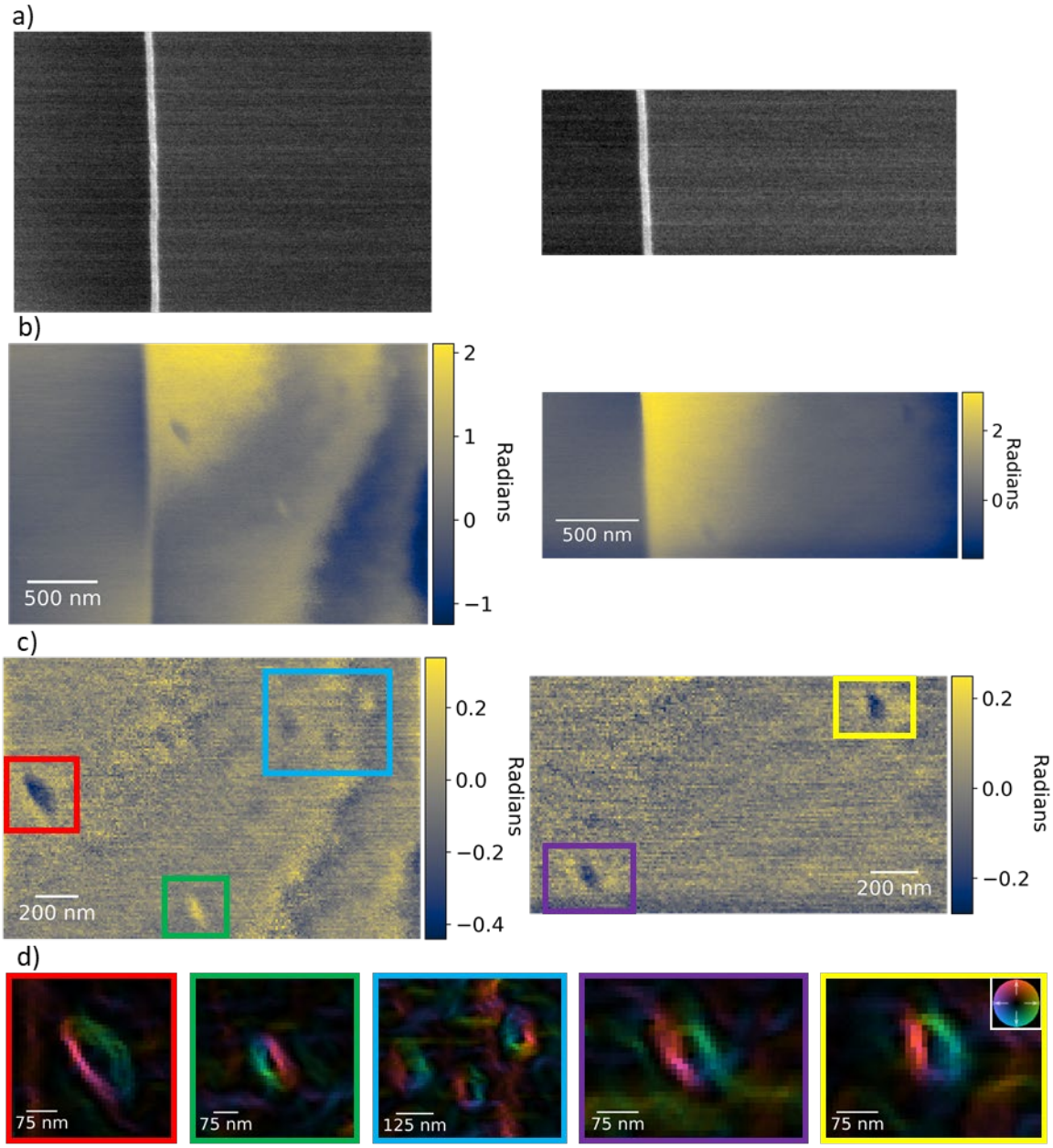

Figure 25: STEMH measurement of Skyrmions in Fe/Gd film
a) HAADF images collected concurrently with two STEMH scans. b) Phase measured by STEMH of two different regions. The line on the left in both images is the edge of the sample. c) Background subtracted phase cut to within the material. d) Magnetic field calculated from the background subtracted phase (direction and magnitude are indicated by the hue and saturation respectively). Outline colors indicate corresponding region of the phase image.

Accounting for Phase Ambiguity

With any phase measurement, the cause of the phase shift can be ambiguous. In TEM, magnetic materials will impart both the magnetic phase of interest and an electrostatic component from the atoms that make up the material. In addition, aberrations in the optical system could add a phase to the beam. As the beams are scanned to perform STEM holography, the path length changes, resulting in a geometric phase background. The sample phase must be isolated from the geometric phase and any aberration phase. Then the magnetic phase must be separated from the electrostatic phase.

In the STEMH phase measurements above, the geometrical phase was removed by fitting a linear function to the area of the image where all the probes are in vacuum and then subtracting that fit. It is assumed that the optical system's aberrations are not contributing significantly. In principle, these two sources of phase can be measured by removing the sample and performing the same scan. As discussed above, in these experiments the electrostatic phase is assumed to be flat and any phase variation is due to the magnetization of the sample. However, the two can be separated quantitatively by flipping the sample and performing the same scan. When the sample is flipped, the sign of the magnetic phase changes but the sign of electrostatic phase does not. The magnetic phase can then be extracted from the difference of the two whereas the electrostatic phase is given by the sum. This adds experimental complexity because the sample state cannot change and the two phase measurements must be aligned. In particular, this would be difficult with the Fe/Gd film, which has magnetic domains that are metastable under an applied field. In a standard TEM holder, the sample must be removed from the microscope (and the applied field) to flip it. A tomography sample holder would allow

for inverting the sample without removing it from the microscope. Alternatively, the electrostatic phase can be isolated by increasing perpendicular applied magnetic field until the sample's magnetization is saturated. This adds its own experimental complexity because the applied field is created by the objective lens. As the strength of the objective lens increases, it affects the optical system and requires realignment.

The last source of ambiguity in the STEMH measurement is the presence of more than two probes. As demonstrated earlier, the lth peak in the Fourier transform of the interference image carries the phase difference between each set of probes l diffraction orders apart. To calculate the phase above, the peak dominated by the interaction/reference probes was used and the other contributions were assumed to be negligible. However, this assumption appears to be false in the permalloy square STEMH measurement. In all the experiments presented here, all but the interaction probe passed through vacuum. Collecting a background-phase measurement with the sample removed would include the phase accumulated by unwanted probes that create artifacts in the STEMH measurement. However, there may be fringing-fields around the sample that the probes passing through vacuum interact with that the background-phase measurement will not be able to identify. There may be a more complete method to separate each probe's contribution.

Assume there are 5 probes contributing, -2 through +2, and only the +1 probe interacts with the sample. At any point in the scan each probe acquires a phase ϕ_n and the +1 probe may also acquire an amplitude change A_1, such that there are 6 unknowns. Each of the +1, +2, and +3 peaks in the Fourier transform of the interference image represents two equations, the real and imaginary components of the integral around that peak.

Therefore, for each scan point, there are 6 equations and 6 unknowns. Using all three peaks in the Fourier transform of the interference image, it should be possible to solve for the phase acquired by each probe as well as the amplitude loss of the interaction probe at each point in the scan.

Conclusion

This chapter presented the first application of diffraction-grating-based STEM holography to magnetic materials. The magnetic phase of two samples, a Landau domain in a permalloy square and skyrmions in an Fe/Gd multilayer thin film, was measured. The issue of multiple potential sources of the measured phase and how to separate those experimentally in the future was discussed. One of the limitations of imaging magnetic materials in a TEM is that the beam is only sensitive to the component of the magnetic vector potential parallel to the optic axis, and consequently only the in-plane components of the magnetic field. In the next chapter, I will discuss how STEM holography can be used to elucidate the 3D structure of a skyrmion. In this chapter, the STEMH phase measurements were compared to Lorentz TEM images to establish accuracy. The next chapter is an example of a measurement that STEMH can make where Lorentz TEM falls short.

CHAPTER IV

PROPOSAL OF STEM HOLOGRAPHY TOMOGRAPHY OF MAGNETIC SOLITONS

Introduction

Magnetic skyrmions are circular magnetic structures in which an in-plane domain wall separates two out-of-plane domains at the periphery and core of the skyrmion. Magnetic skyrmions were first observed in 2009 [62] and since then many systems that support them at room temperature have been found. They can be formed by long-ranged magnetic dipolar interactions [39]–[42], [98]–[101], the Dzyaloshinksii-Moriya Interaction (DMI) [62]–[65], frustrated exchange interactions [102], or four-spin exchange interactions[103]. Skyrmions are inherently stable because of their geometry; the magnetization cannot be unwound without breaking the continuity of the field. Because of this there has been interest in using skyrmions as information carriers in racetrack memory [2]–[4].

In this chapter I discuss the possibility that dipole skyrmions in multilayer thin films composed of iron and gadolinium [38]–[42] are in fact magnetic hopfions, which are 3D solitons. The magnetic structure in these materials is stabilized by dipolar interactions and so is referred to as a "dipole skyrmion." Like skyrmions, hopfions have topological stability and are therefore of interest in memory applications [104]. While stable magnetic hopfions were first theoretically predicted in 1988 [105], [106], they have not been observed experimentally. Since 2017, the search for and theoretical study of magnetic hopfions has grown with micromagnetic simulation studies [107]–[109], simulations of their response to current or applied magnetic field [104], [109], [110], and

material parameter searches [1]. Hopfions are characterized by a nonzero topological number referred to as the Hopf index [111]. Micromagnetic simulations informed by bulk physical measurements of dipole skyrmions in an Fe/Gd film are best fit by a hopfion model with a Hopf index of $1/2$ [112]. Interestingly, the studies mentioned above have assumed an integer Hopf index, but fractional hopfion models are theoretically supported [113]–[115]. The dipole skyrmions in Fe/Gd films have been imaged using LTEM [38], [40] and transmission X-ray microscopy [39], [41], [42]. Both techniques measure the magnetic structure integrated through the thickness of the film and neither can confirm the 3D magnetic structure calculated by micromagnetic simulation. Experimentally confirming the 3D structure of dipole skyrmions would be the first observation of a magnetic hopfion.

3D micromagnetic structure information can be accessed in a few different ways. Recently, resonant elastic X-ray scattering (REXS) has been used to study the depth dependence of magnetic spins near the surface of a bulk material [116]–[118]. Transmissive techniques like S/TEM can be combined with surface sensitive measurements like scanning electron microscopy with polarization analysis (SEMPA) [119] for some added insight. To form a 3D reconstruction of a magnetic structure using transmissive techniques, tomography is used. In tomography, the reconstruction is computed from a set of 2D projections of the object viewed from different angles [120]. This method has been employed to image magnetic materials with neutron [121]–[123], X-ray [124]–[131], and electron microscopy techniques [22], [132]–[146] since 2008, 2015, 1994 respectively. Electron microscopy leads the three in resolution, reaching sub-10 nm, while the X-ray studies demonstrated 50 – 100s of nms resolution and the neutron

studies did not reach sub-micron resolution. After the first report of tomographic electron microscopy measuring the 3D distribution of one component of the magnetic field using electron holography [136], further progress was slow due to instrumental and computational limitations. Between 1994 and 2010, there were several demonstrations of tomographic differential phase contrast [143]–[146] and theoretical developments [147], [148]. The first use of LTEM for a tomographic reconstruction of a material's magnetic field was published in 2010 [139]. These tomographic studies using either LTEM [140]–[142] or off-axis electron holography [22], [132]–[135], [137], [138] started to become more common in 2014 along with further theoretical development [149]–[152]. Here, a combination of SEMPA, tomographic LTEM, and tomographic S/TEM is proposed to study the 3D structure of dipole skyrmions.

SEMPA of the magnetization at the surface of an Fe/Gd film supports the 3D structure calculated by micromagnetic simulation [112]. Attempted tomographic Lorentz TEM studies of the film were inconclusive [112]. In this chapter, I present a simulation of tomographic STEM holography, which can be used to distinguish between a standard skyrmion (uniform through the thin film thickness) and the fractional hopfion. One of the distinguishing traits of the hopfion is a much lower average phase projected through the sample. I compare experimental STEMH measurements of dipole skyrmions in an Fe/Gd thin film to the phase of the hopfion and show they agree.

Micromagnetic Simulation and Hopfion Model

Skyrmions are often assumed to be essentially two-dimensional structures and uniform through the thickness of the magnetic material but in many cases this may not be true. The first experimental probe of the 3D structure of a magnetic skyrmion measured

the magnetic phase of DMI-stabilized skyrmions in a step-shaped sample using off-axis electron holography in 2014 [153]. They found that the phase varied linearly with the sample thickness and concluded the skyrmion was uniform throughout. Since 2018, several studies have further explored this question. Schneider et al. found that when imaging Bloch skyrmions in a magnetic thin film via LTEM, the reconstructed magnetic field was much lower than expected and proposed this was due to variations in the structure through the film thickness. Zhang et al. used REXS to show that skyrmions in different bulk materials can be uniform [118] or nonuniform [116], [117]. Most of these studies commented that their experimental observations could not be explained by preexisting spin structure models, highlighting the important of probing the 3D micromagnetic structure [116], [118], [140]. There has been no measurement of the 3D structure of a dipole skyrmion.

Micromagnetic modeling of the Fe/Gd film shows that the magnetic structure changes through the film thickness [39]–[42], as shown in Figure 26. A micromagnetic simulation of a 4 μm^2 area of an 89 nm thick film shows dipole skyrmions are formed, shown in Figure 26a. In the center of the film, the in-plane magnetization of these structures winds azimuthally, as in a Bloch-type skyrmion (Figure 26d). The magnetization changes through the thickness of the film to point radially at the surfaces, as in Néel-type skyrmions, shown in Figure 26c and e. These are referred to as Néel caps. A cross-section shows that both the magnetization orientation and domain wall width change through the film thickness (Figure 26b).

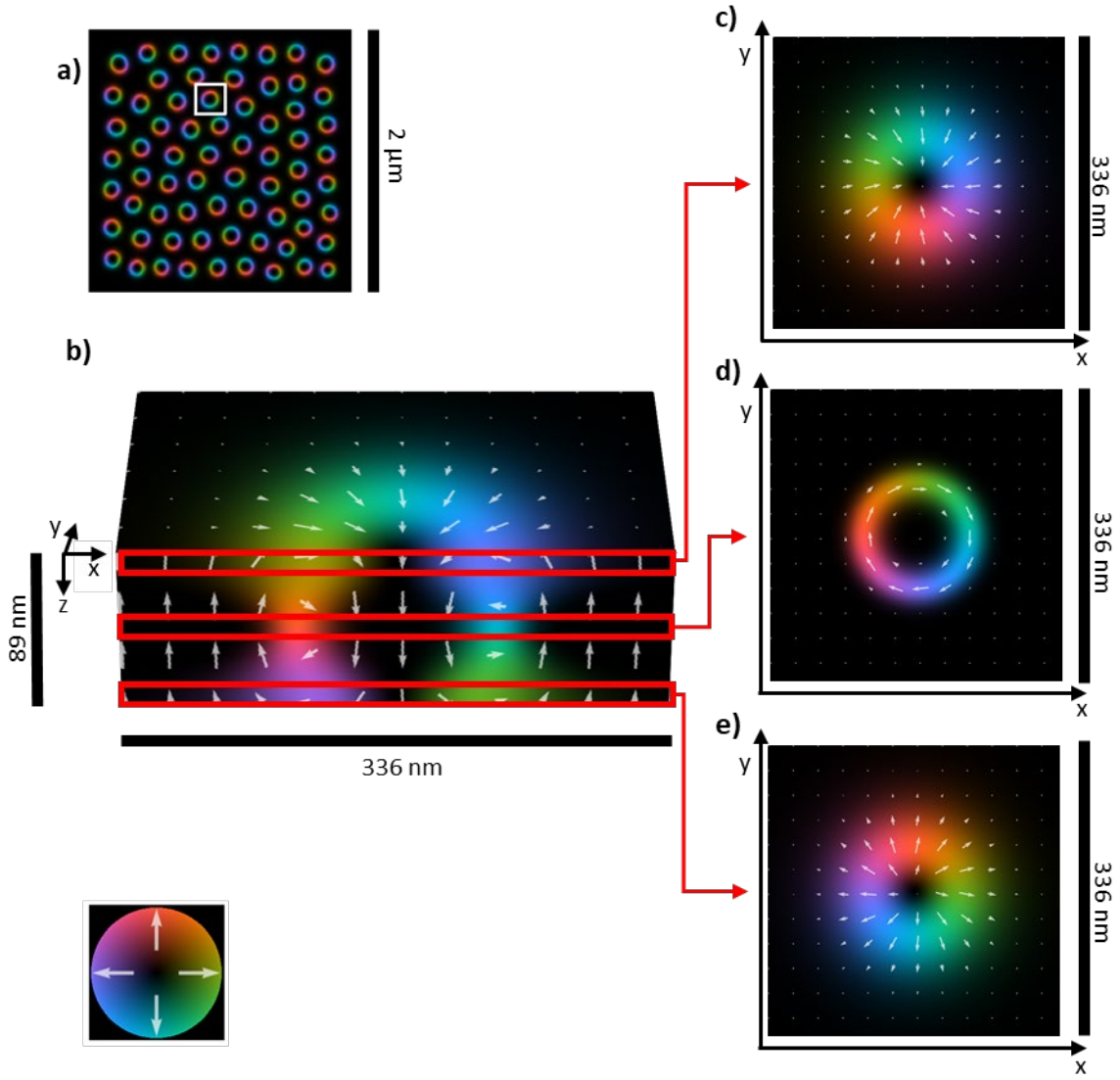

Figure 26: Micromagnetic Simulation of Dipole Skyrmions in Fe/Gd Film
Colorplot of the magnetization in a) the *xy*-plane through the center of the micromagnetic simulation, b) the *xz* plane through the center of one of the skyrmions (indicated in a) by a white square), & the *xy* plane c) at the top of, d) in the center of and e) at the bottom of the skyrmion. Magnetization *x* and *y* components direction and magnitude are indicated by the hue and saturation respectively.

Chess fit the model:

$$m(\rho,\phi,z) = \{\sin[\Theta(\rho,z)]\cos[\phi-\gamma(z)], \sin[\Theta(\rho,z)]\sin[\phi-\gamma(z)], \cos[\Theta(\rho,z)]\}$$

$$\Theta(\rho,z) = 2\tan^{-1}\left[k(z)\rho^{\alpha(z)}\right]$$

$$\gamma(z) = \frac{\pi}{2}\tanh(b_\gamma z) + c_\gamma \qquad (4.1)$$

$$k(z) = \alpha_k e^{-b_k z^2} + c_k$$

$$\alpha(z) = a_\alpha e^{-b_\alpha z^2} + c_\alpha$$

to the micromagnetic simulation [112]. Here the function $\gamma(z)$ determines the helicity through the material thickness and produces the Néel caps and Bloch center. The size of inner core and domain wall thickness are set by $k(z)$ and $\alpha(z)$ respectively. Hopfions are characterized by a nonzero Hopf index, which is calculated from

$$H = -\frac{1}{(8\pi)^2}\int d^3x\, \vec{F}\cdot\vec{A}$$

$$F_i = \epsilon_{ijk}\vec{m}\cdot\left(\partial_{x_j}\vec{m}\times\partial_{x_k}\vec{m}\right) \tag{4.2}$$

$$\nabla\times\vec{\mathrm{A}} = \vec{F}$$

where $\vec{m}$ is the magnetization unit vector. Using the parameterization described above, this simplifies to

$$H = \frac{Q}{4\pi}\int_{-\infty}^{\infty}\int_{0}^{\infty}\sin(\Theta)\,(\,\partial_\rho\Theta\,\partial_z\phi - \partial_z\Theta\partial_\rho\phi)\,d\rho dz\,. \tag{4.3}$$

Chess found that using the parameter values determined by fitting the model to the micromagnetic simulation gives a hopf index of

$$H = \frac{\tanh(112.613)}{2} \approx \frac{1}{2}. \tag{4.4}$$

The non-zero hopf index indicates that this magnetic structure is a hopfion.

Previous Measurements

When observing this structure in TEM, the Bloch center is visible, but the Néel caps are not. This is because the phase imparted on the electron beam is an integral over the out-of-plane component of the magnetic vector potential, which is an integral over the out-of-plane component of the curl of the magnetization [94]. In Néel-type skyrmions,

the magnetization is radial and therefore there is no out-of-plane component of the curl of the magnetization. As such, Néel-type skyrmions do not impart a phase on the electron beam and are not visible in a TEM unless the sample is tilted [154], [155]. Therefore, when imaged with LTEM at normal incidence to the thin film, the projection of the hopfion appears as a Bloch-type skyrmion. Experimental LTEM measurements of dipole skyrmions meet this expectation [40].

The McMorran lab previously attempted to probe the thickness dependence of dipole skyrmions via two methods: SEMPA and tomographic LTEM [112]. SEMPA measures a material's magnetization at the surface. With no applied field the Fe/Gd films form stripe domains, which micromagnetic simulations show have Néel caps and a Bloch center like the dipole skyrmion. The SEMPA measurements show that the stripe domains have Néel caps, as expected. While this supports the accuracy of the micromagnetic modeling, it is only a surface sensitive measurement. This also is not a measurement of the dipole skyrmion of interest. Chess recorded Tomographic LTEM measurements of the dipole skyrmion in an Fe/Gd film from zero tilt to 30° tilt in 5° increments, shown in the center column of Figure 27 [112]. Chess simulated tilt-series measurements of a hopfion and a standard uniform skyrmion, shown in the left and right columns of Figure 27 respectively, in hopes that the experimental data could be clearly distinguished as one or the other. However, the differences in LTEM images are too subtle to clearly differentiate [112]. Here I show that the same tilt series imaged using STEM holography could distinguish between a standard skyrmion and a hopfion.

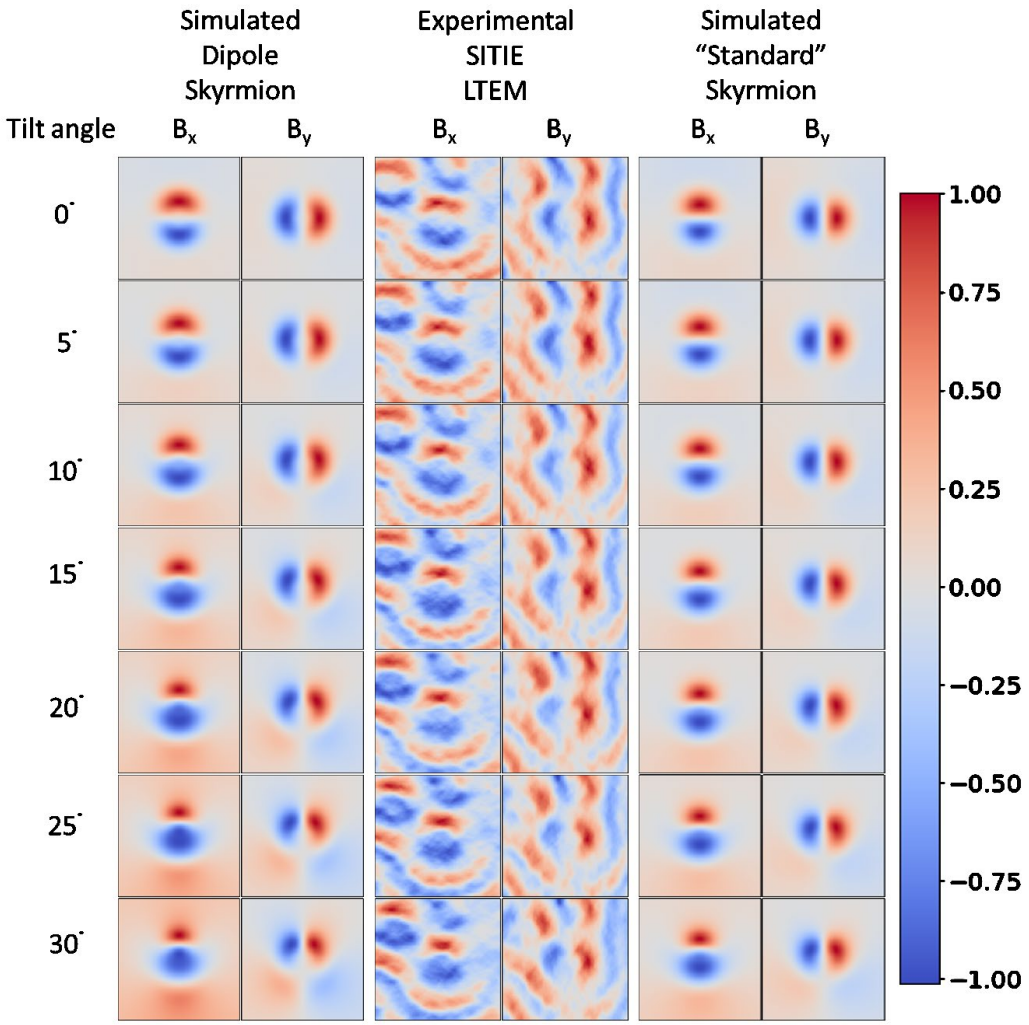

Figure 27: Simulated and Experimental Tomographic LTEM
This figure incorporates Figure 35 in "Mapping Topological Magnetization and Magnetic Skyrmions" by Jordan Chess, used under CC BY.

Tomographic STEM Holography Simulation Methods

A diagram of the ideal STEM holography optical system is shown in Figure 28a. A diffraction grating creates two probes at the sample plane. The +1 order probe interacts with the sample. At the detector, the probes are defocused and overlapped so they interfere. The phase at that probe position is calculated from the image of the interference pattern. The components of the simulation are therefore the diffraction grating, magnetic sample, beam/sample interaction, and the interference image captured by the detector.

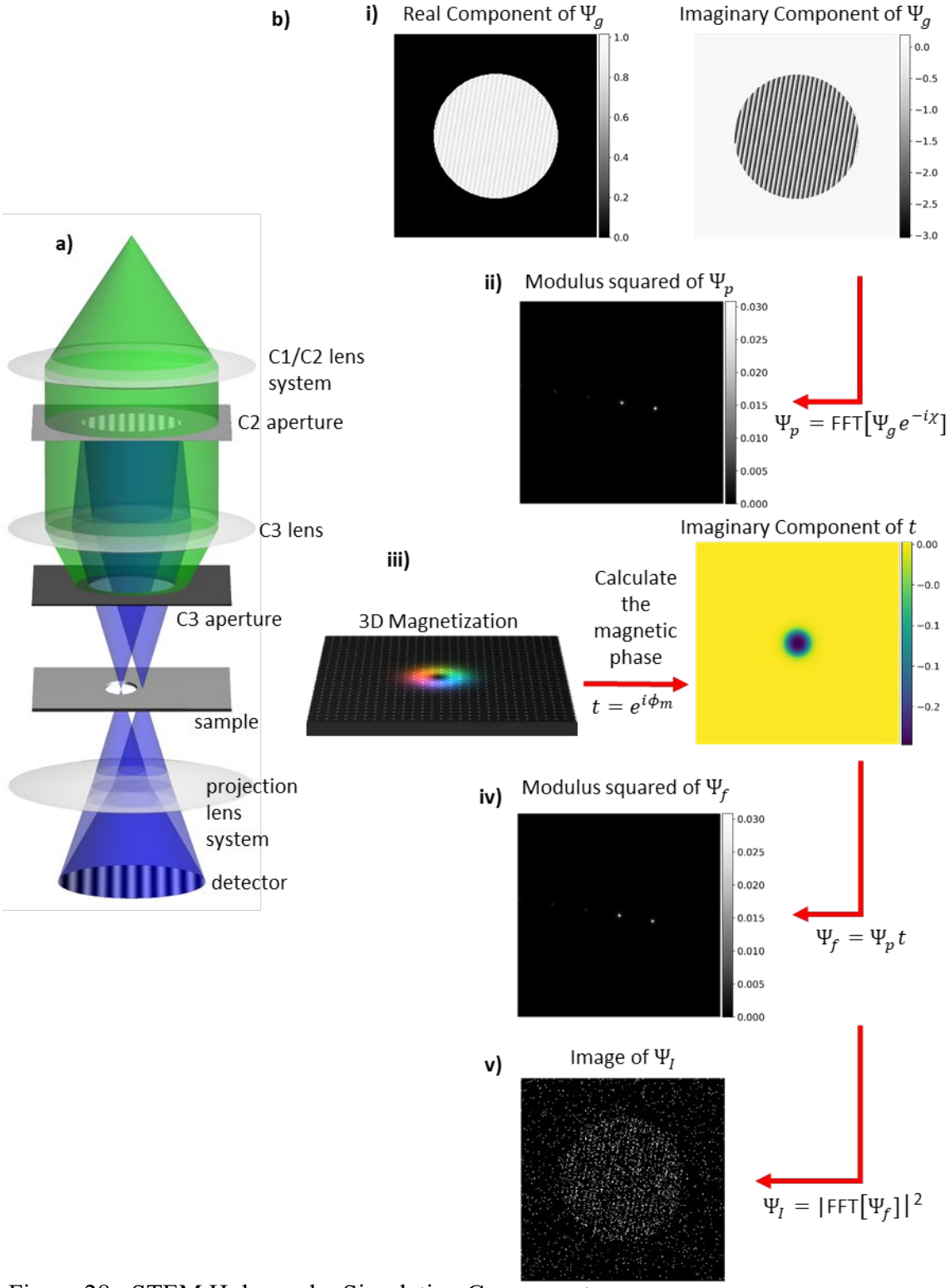

Figure 28: STEM Holography Simulation Components
a) Ideal STEMH optical system. b) STEMH simulation components including the electron wavefunction i) just after the diffraction grating, ii) just before and iv) just after the sample (iii) & v) the interference image collected.

The diffraction grating is a pattern milled into a silicon nitride membrane via focused ion beam [79]–[84]. Assuming the grating is illuminated with a plane wave, the electron wavefunction after interacting with the grating is

$$\Psi_g(\vec{k}) = e^{i\tilde{\eta}T(\vec{k})} \tag{4.5}$$

where $\tilde{\eta}$, which is complex valued, gives the longitudinal phase shift and amplitude attenuation per unit length of the material and $T(\vec{r})$ is the longitudinal thickness profile of the grating. The wavefunction is written in terms of Fourier space coordinates $\vec{k}$ because this is the Fourier plane of the sample plane. A blazed grating (sawtooth groove profile) with 29.9 nm maximum mill depth in a silicon nitride membrane is simulated and the resulting electron wavefunction is calculated using $\tilde{\eta} = \frac{\pi}{33\ nm}(0.08i - 1)$, the value for silicon nitride and a 300keV electron beam [81]. Electrons that pass through the silicon nitride membrane outside the diffraction grating pattern are removed experimentally by an aperture between the grating and the sample. In the simulation this is accounted for by setting the electron wavefunction amplitude to 0 outside the radius of the grating. Assuming only spherical aberration and defocus are significant, the probes formed at the sample are given by

$$\Psi_p(\vec{r}) = FFT\left[e^{i\chi(\vec{k})}e^{i\tilde{\eta}T(\vec{k})}\right]$$

$$\chi(\vec{k}) = \frac{\pi}{2}C_s\lambda^3k^4 - \pi\Delta f\lambda k^2 \tag{4.6}$$

where FFT indicates the 2D fast Fourier transform, C_s is the spherical aberration coefficient and Δf is the defocus. The grating produces two significant probes: the 0th and 1st order. The values of C_s and Δf were tuned so the probe diameter is approximately 8nm. To determine the probe size, the diameter of the circle around the peak containing

50% of the probe intensity was found [156]. This was done for a 94nm by 94nm square around the interaction peak, shown in Figure 29a. The fractional intensity as a function of distance from the peak center is shown in Figure 29b. This probe size is comparable to what we have already achieved experimentally, approximately 10nm. This value is estimated from the smallest features visible in experimental images.

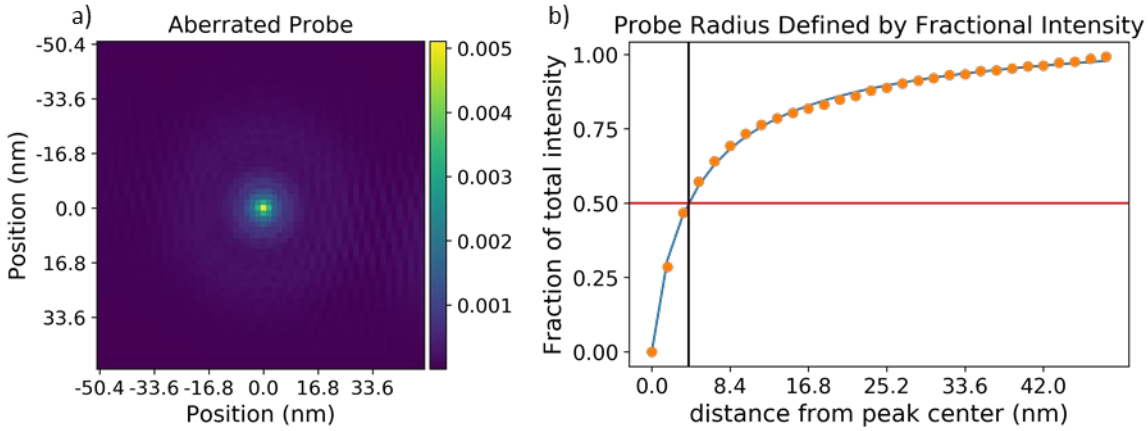

Figure 29: Simulated Interaction Probe
a) Simulated interaction probe. b) Fractional intensity as a function of the distance from the peak in orange. The blue line is a hyperbolic fit. The horizontal red line indicates 0.5, the threshold which is used to define the size of the probe. The vertical black line indicates at what radius the hyperbolic fit reaches 0.5.

The next piece of the simulation is the sample. To simulate the hopfion, the 3D analytical fit to the Fe/Gd micromagnetic simulation summarized in Equation 4.1 was constructed as a 3D array with voxel size 1.68 nm, extent 1 μm, and depth 89 nm. To simulate a 3D array of identical size featuring the standard uniform skyrmion, the Bloch-type structure in the center of the simulated hopfion was assumed to be uniform throughout the entire thickness of the simulated film. As discussed in Chapter III, the magnetic phase can be calculated from the magnetization via the expression

$$\tilde{\phi}_m(k_x, k_y) = -\frac{i\mu_0 e M_s}{2\pi\hbar}\frac{k_y\widetilde{m_x} - k_x\widetilde{m_y}}{k_x^2 + k_y^2} \tag{4.7}$$

where $\overline{m_x}(x,y)$ and $\overline{m_y}(x,y)$ are the integrals of $m_x(x,y,z)$ and $m_y(x,y,z)$ over z and the tilde indicates the 2D Fourier transform. From the simulated magnetization of the standard skyrmion and hopfion, the magnetic phase is calculated, shown in Figure 33a and Figure 34a respectively. Only the magnetic phase is included in the sample's transmission function, i.e.

$$t(\vec{r}) = e^{i\phi_m}. \tag{4.8}$$

As discussed in Chapter III there are other potential sources of phase but the magnetic phase can be isolated experimentally. The wavefunction of the electron beam after interacting with the sample is

$$\Psi_f(\vec{r};\vec{x}_p) = \Psi_p(\vec{r};\vec{x}_s)t(\vec{r}) \tag{4.9}$$

where $\Psi_p(\vec{r};\vec{x}_s)$ is the electron wavefunction just before the sample and $\vec{x}_s$ is the scan offset. In the simulation, the area surrounding the 1st order probe is multiplied by a corresponding area of the transmission function.

The interference image Ψ_I is calculated by taking the modulus squared of the Fourier transform of Ψ_f, the electron wavefunction after interacting with the sample. The STEMH experiments reported in Chapter III were performed using the Gatan K2, a direct electron detector which produces much less noise than the standard scintillator-based cameras [157]. In actual experiments, the collected interference images are thresholded to find pixels with single electron events, creating a binary image from which the phase is calculated [158]. To simulate this process, the interference image was filled in probabilistically by choosing pixels using Ψ_I as a discrete probability distribution [159], [160]. The number of pixels filled in was calculated using the average count per pixel in the grating and surrounding vacuum area in the experimental STEMH images. In the

simulated images, the grating was filled in first. Then random pixels were added as given by the average count per pixel in the vacuum region of the experimental images. Finally, the phase for that location in the simulated scan is calculated from the interference image as is done with experimental data. The 1st order probe is interacting with sample and the 0th order probe is the reference, so the phase is calculated from the +1 peak in the FFT of the interference images. To form the complete phase image, this is repeated for an array of points across the sample.

To simulate the tomographic experiment, the magnetization simulations for both the standard skyrmion model and the hopfion model are rotated about the *y*-axis using spline interpolation from 0° to 5° in 1° increments and from 10° to 40° in 10° increments [161]. A simulated STEMH scan is done for each rotation angle.

Tomographic STEM Holography Simulation Results

The first distinction that can be made between the standard skyrmion and the hopfion is the phase peak amplitude at zero tilt; the phase amplitude of the standard skyrmion is 0.39 ± 0.03 radians whereas in the hopfion case it is 0.29 ± 0.03 radians, found by averaging along the phase profiles shown in Figure 30b over 6 pixels, or 9.6 nm. Each layer of the standard skyrmion is Bloch-type and contributes to the magnetic phase. In the hopfion, the Bloch-type center contributes most to the magnetic phase. However, the magnetization reorients into Néel caps at the surfaces, which do not contribute to the magnetic phase, resulting in a lower phase peak amplitude. These simulated measurements of the two models can then be compared to the experimental STEMH measurements of dipole skyrmions in an 89 nm thick Fe/Gd film deposited on a

silicon nitride membrane with a grid of 20um circular holes (Figure 24) originally presented in Chapter III.

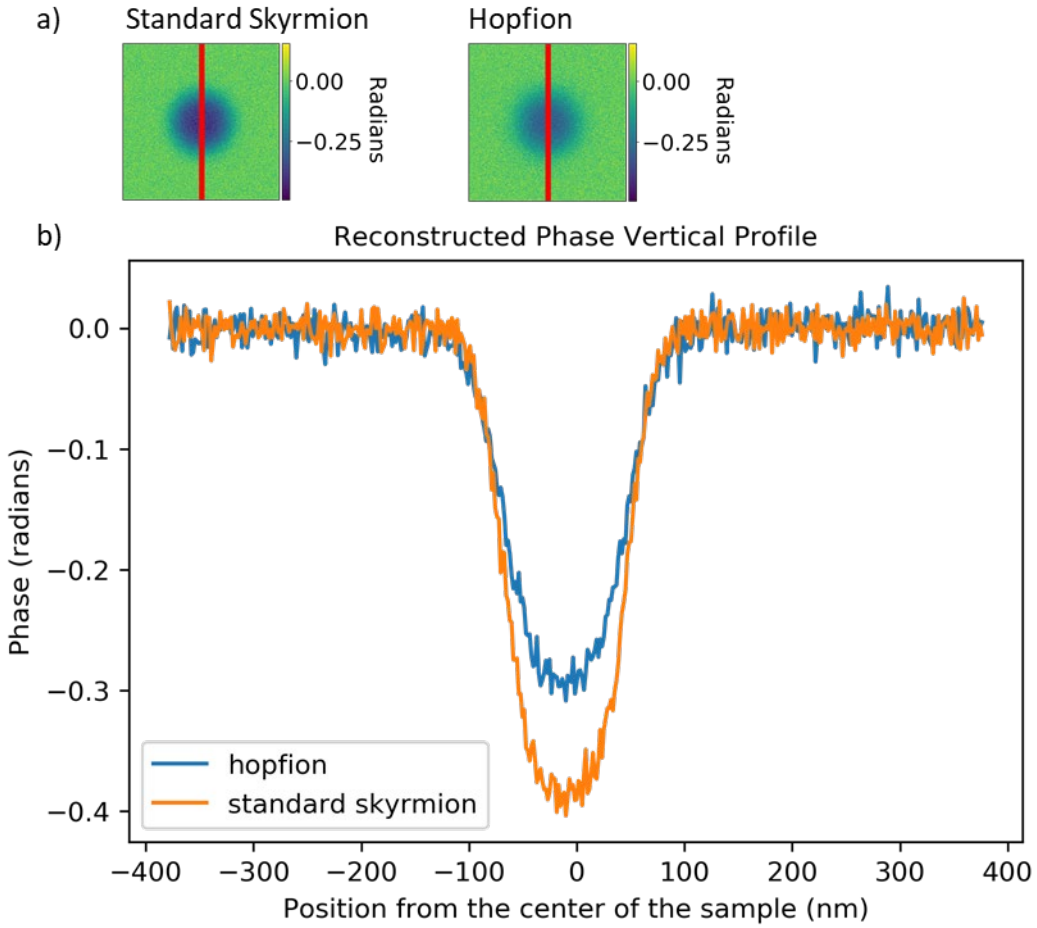

Figure 30: Simulated STEMH Reconstruction of a Standard Skyrmion and a Hopfion at Zero Tilt
a) Magnetic phase of a standard skyrmion and a hopfion reconstructed by a simulated STEMH experiment. The red lines indicate the columns averaged together to form b) a vertical phase profile through the center of each magnetic texture.

Each isolated phase feature and a phase profile through its center averaged over 3 pixel columns, or 30 nm, are shown in Figure 32 and Figure 31. The measured phase profiles are plotted with the predicted hopfion and standard skyrmion phase profiles for comparison. The phase profiles in Figure 32a-c.ii. and Figure 31d agree more closely with the hopfion model than the standard skyrmion model. However, the phase profiles in

Figure 31b and Figure 31c have lower amplitudes than both models and the phase profile in Figure 32d.ii. has a larger amplitude than the hopfion model. This variation could be due to electrostatic phase contributions from the sample, which was not removed experimentally and was assumed to not contribute significantly. This variation could also be due to the geometry of the substrate altering the micromagnetic structure. As mentioned in Chapter III, this effect may also explain why some of the dipole skyrmions in the STEMH measurements appear elongated, as in Figure 32b-d.i. The dipole

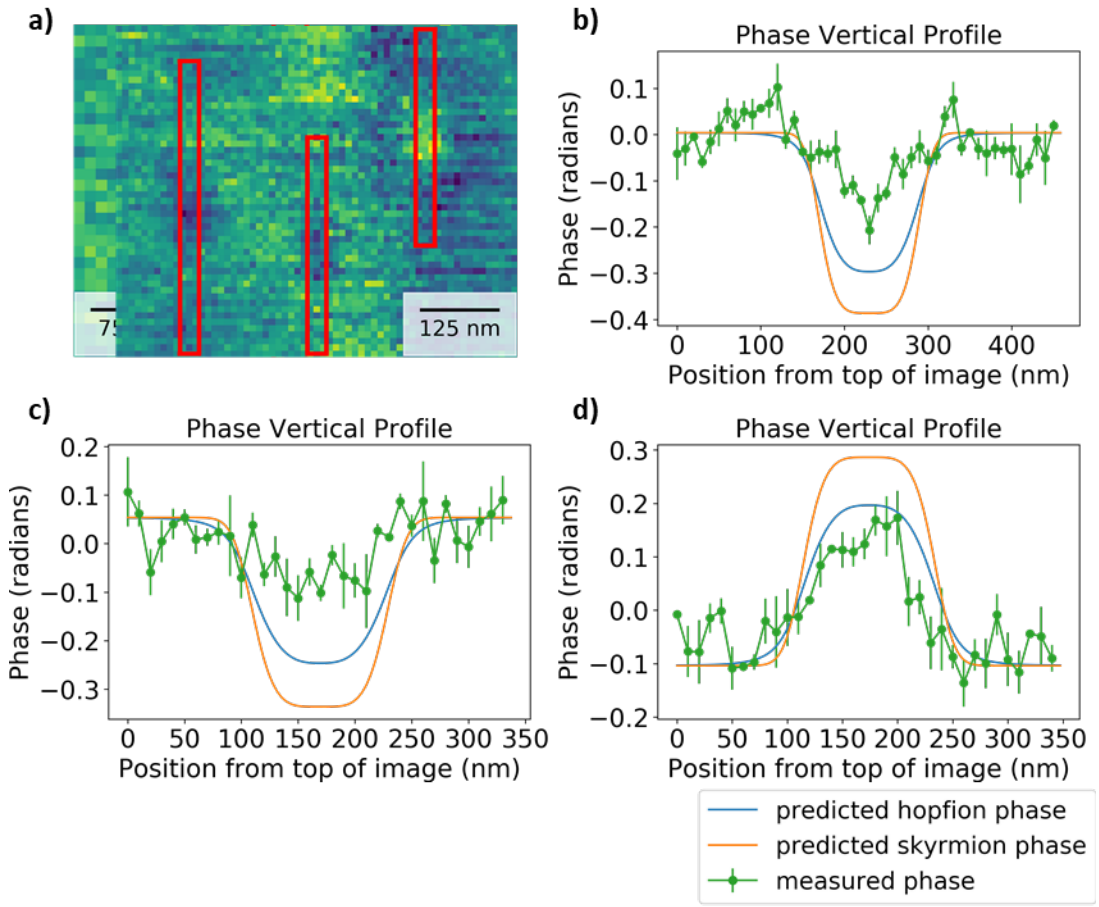

Figure 31: STEMH Measured Phase of Dipole Skyrmions
a) The phase of dipole skyrmions measured via STEMH. A phase profile through the center of b) the leftmost skyrmion, c) the the central skyrmion, and d) the rightmost skyrmion averaged over the columns enclosed in each corresponding red box in the phase image. The predicted phase profiles for a hopfion and a standard skyrmion are shown in blue and orange respectively.

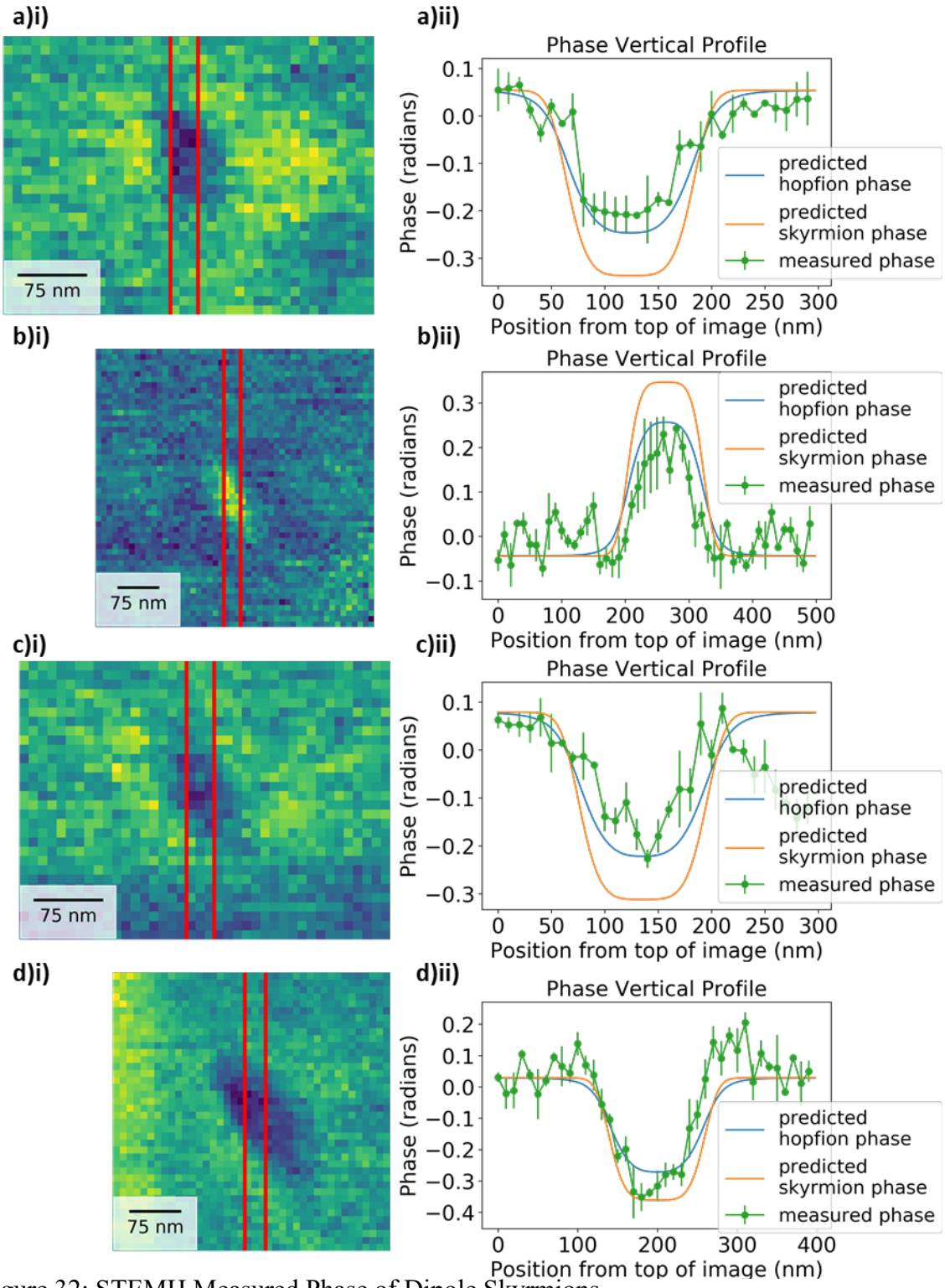

Figure 32: STEMH Measured Phase of Dipole Skyrmions
a-d)i) The phase of dipole skyrmions measured via STEMH. a-d)ii) A phase profile through the center of the dipole skyrmions averaged between the red lines in the phase image. The predicted phase profiles for a hopfion and a standard skyrmion are shown as blue and orange lines respectively.

skyrmions in Figure 31a appear more circular and were farther from the edge of the sample. The initial experimental STEMH measurements appear to be better fit by the hopfion model but further experiments could provide more conclusive evidence.

In the simulated STEMH measurements, the scan pixel size is 1.68 nm and the simulated probe size is 8.4 nm. Neighboring pixels were then averaged together to reduce noise. In the experimental STEMH measurements, the scan pixel size is 10 nm, the same as our estimate of the probe size. By replicating the process of oversampling the phase by setting the scan pixel size to less than the probe size, the noise in our experimental measurements could be reduced. In addition, further measurements could elucidate if there is a relationship between the location of the dipole skyrmion relative to the 20-um hole grid of the supporting membrane and the phase amplitude at zero tilt. Lastly, the electrostatic phase can be removed experimentally as described in Chapter III.

A second distinction between the two models can be made as they are tilted. The reconstructed phase of the standard skyrmion and the hopfion at 0°, 10°, 20°, 30°, and 40° are shown in Figure 33a and Figure 34a respectively. To further elucidate differences between the two cases, the phase profile in y through the center of the magnetic textures for each rotation is shown in Figure 33b and Figure 34b. To reduce noise, the phase profiles are averaged over 9 columns of pixels, or 15 nm. As the standard skyrmion and hopfion are tilted, the phase of both forms two lobes, as shown in Figure 33 and Figure 34. The two trends look similar but the peak-to-peak height between the two lobes grows more relative to the initial amplitude in the hopfion case. In the hopfion case, at 40° the ratio of the peak-to-peak height to the amplitude at zero tilt is 2.8 ± 0.3. In the standard skyrmion case, this ratio is 2.2 ± 0.2. When both models are imaged at a tilt, the electron

beam passes through more material, creating a larger phase gradient across the domain wall. But, when the standard skyrmion is tilted, each Bloch-type layer contributes less phase. As the hopfion is tilted the Bloch-type center imparts less phase but the rest of the structure imparts more phase. This results in a measurably different amplitude change.

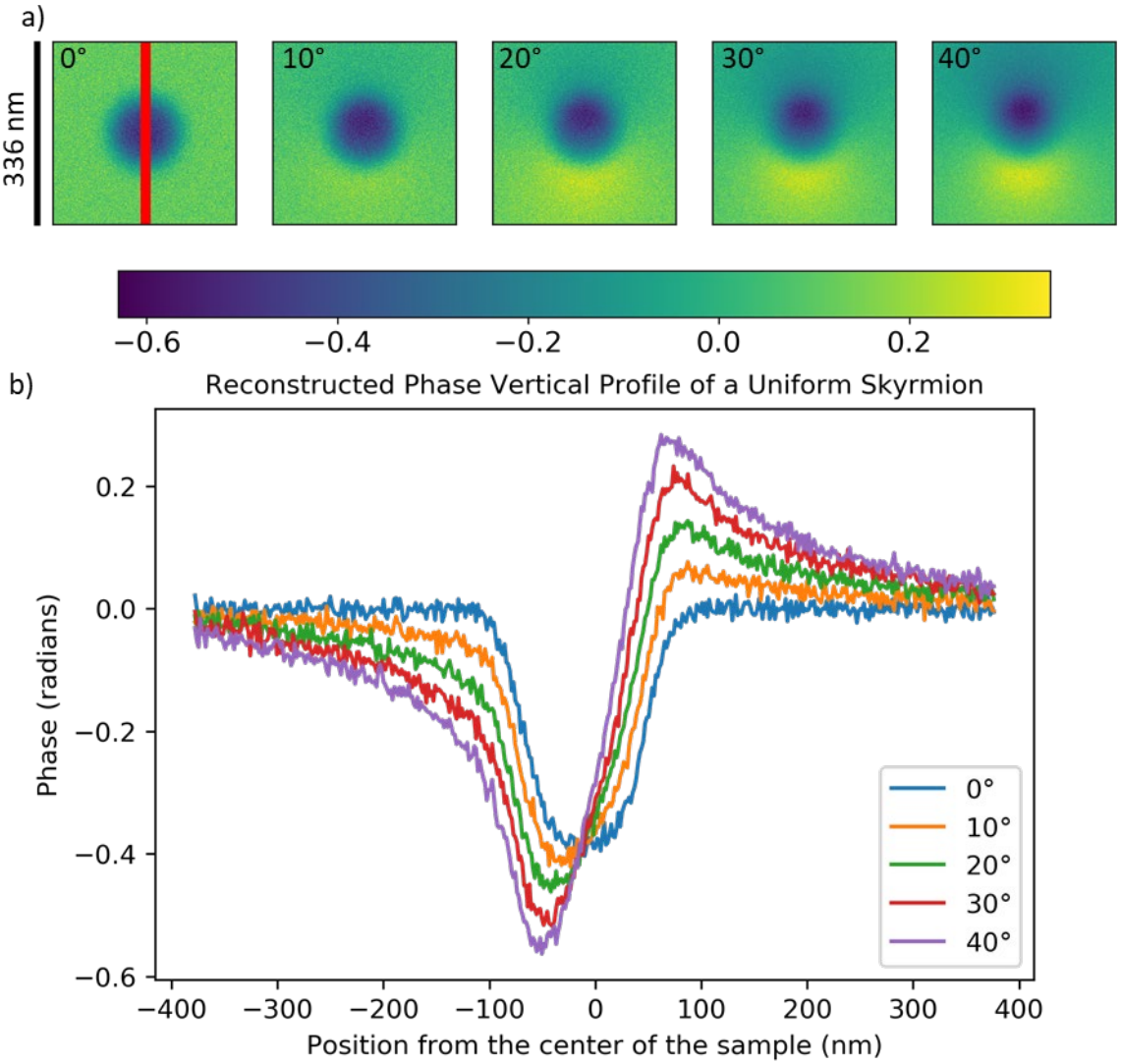

Figure 33: STEMH Tomography of a Standard Skyrmion Simulation
a) Magnetic phase of a simulated standard skyrmion for 0° to 30° tilt. b) The phase measured by STEMH at each tilt. c) The phase profile through the center of the skyrmion parallel to the axis of rotation.

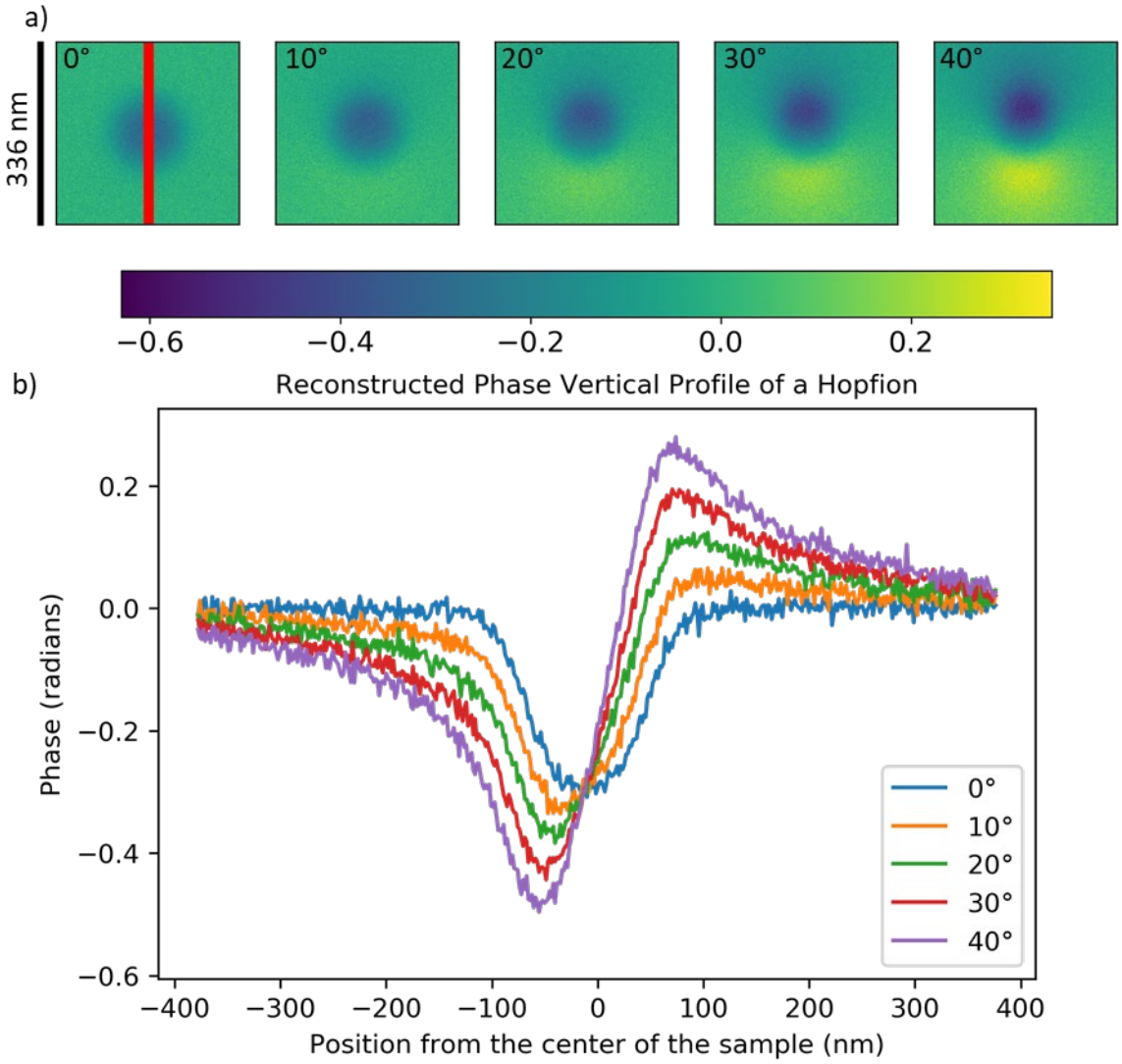

Figure 34: STEMH Tomography of a Hopfion Simulation
a) Magnetic phase of a simulated hopfion for 0° to 30° tilt. b) The phase measured by STEMH at each tilt. c) The phase profile through the center of the hopfion parallel to the axis of rotation.

A third distinction can be made between the magnetic phase of the standard skyrmion and hopfion as they are tilted between 0° and 5°, shown in Figure 35a and b. A phase profile through the center of the standard skyrmion model (green lines in Figure 35c where increasing saturation indicates a higher tilt angle) shows that the peak in the phase flattens in the middle. This is further demonstrated by the curvature of the phase profile (green lines in Figure 35d), which goes to zero in the middle of the phase peak.

The gradient of the phase is proportional to the in-plane magnetic field. In the standard skyrmion model, there is a wide area within the skyrmion where the magnetization points out-of-the-plane of the film throughout the thickness. Over that area the gradient of the magnetic phase must be zero, creating the flat phase peak at zero tilt. As the standard skyrmion is tilted, the curvature at the center of the phase peak remains zero. In the hopfion model, there is a much smaller region where the magnetization points out-of-the-plane of the film throughout the thickness because the domain wall width varies, resulting in a more rounded phase peak. The curvature of the hopfion phase profile does not go to zero, as shown in Figure 35d in red. While this distinction was not clearly distinguishable

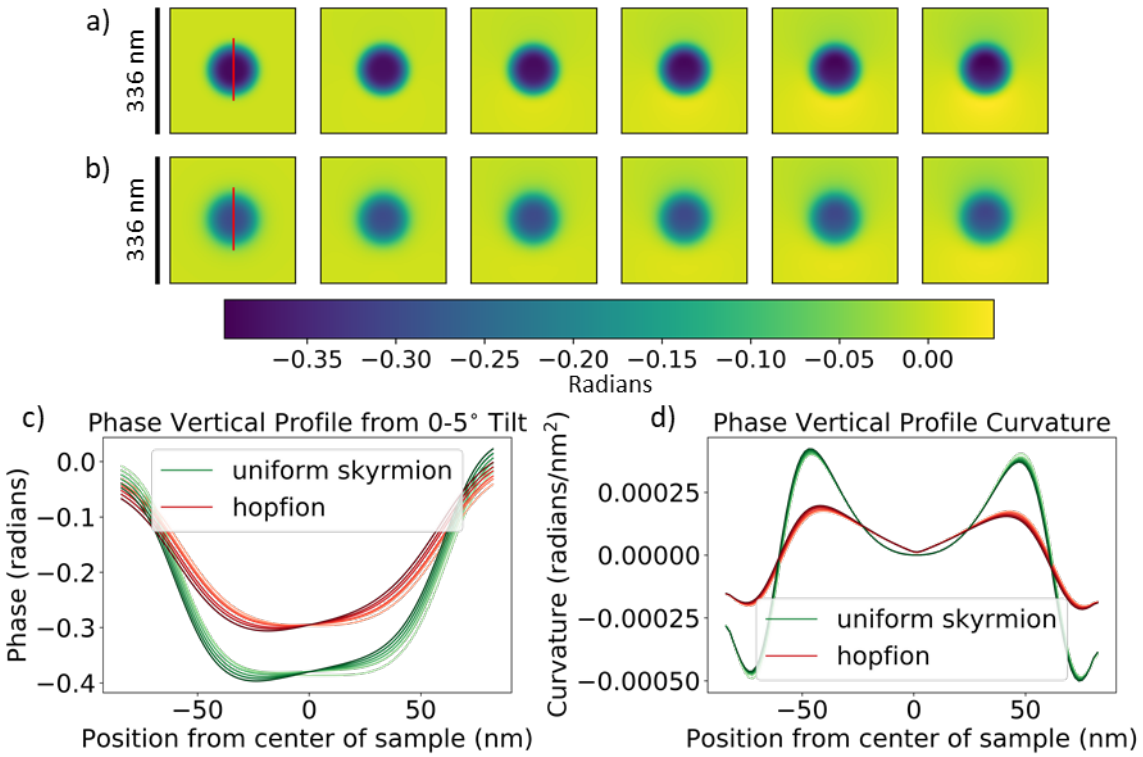

Figure 35: Predicted Phase of a Standard Skyrmion and Hopfion at Small Tilt Angles a) Predicted phase of a standard skyrmion and b) of a hopfion at 0° - 5° tilt. c) Phase profile through the center of the standard skyrmion and hopfion shown in red and green respectively. Increasing saturation indicates a higher tilt angle. d) The curvature of the phase profiles in c).

in simulated STEMH reconstructions of the phase of the two models with a 8.4 nm probe, it was in reconstructions with a 3.0 nm probe, shown in Figure 36.

When reconstructing the phase via STEMH, features at or below the length-scale of the probe size are not visible. Because of this, the difference in phase peak curvature was not detectable in simulated STEMH reconstructions of the phase of the two models with a 8.4 nm probe. However, the difference is visible in reconstructions with a 3.0 nm probe, shown in Figure 36. The phase profiles through the centers of the reconstructed uniform skyrmion (Figure 36a) and hopfion (Figure 36b) are shown in Figure 36c in blue and orange respectively. A curve was fit to the reconstructed phase profiles by univariate spline interpolation [161]. The curvature of the curves fit to the reconstructed phase

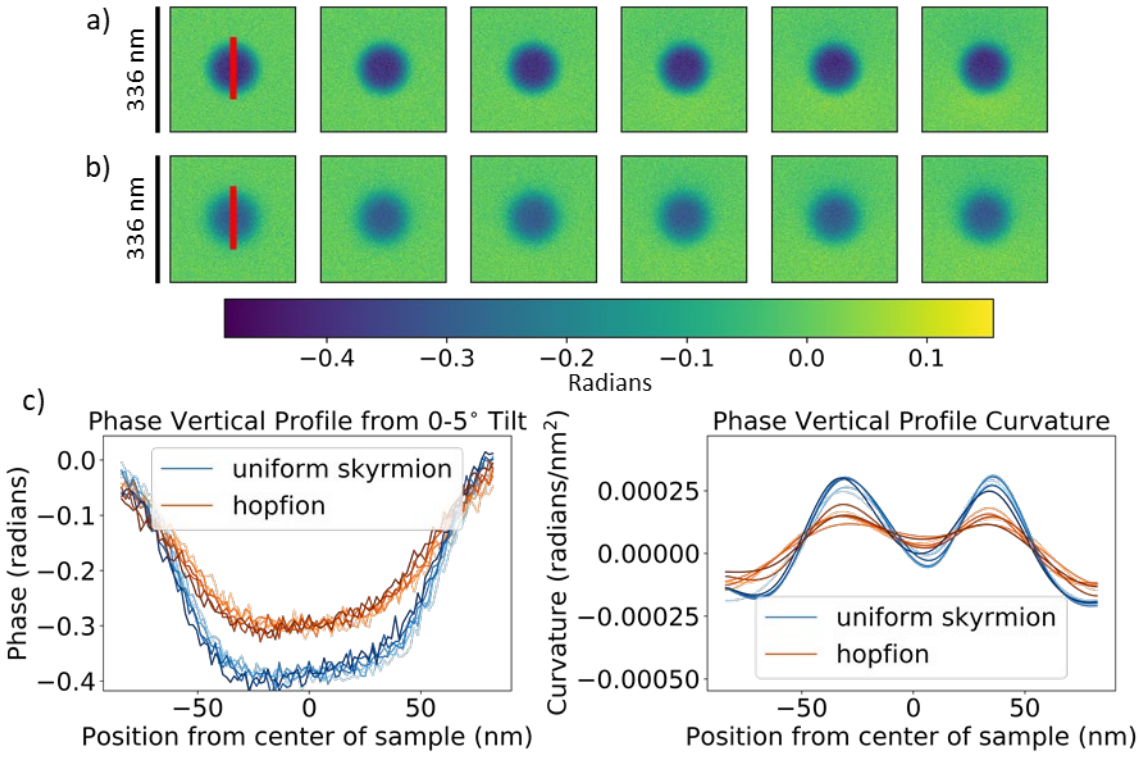

Figure 36: STEMH Reconstructed Phase of a Standard Skyrmion and Hopfion at Small Tilt Angles

a) Reconstructed phase of a standard skyrmion and b) of a hopfion at 0° - 5° tilt by a STEMH simulation. c) Phase profile through the center of the standard skyrmion and hopfion shown in red and green respectively. Increasing saturation indicates a higher tilt angle. d) The curvature of the spline-interpolated fits to the phase profiles in c).

profiles are shown in Figure 36d. Due to noise in the STEMH measurements and the finite probe size, the curvature of the predicted phase profiles are not exactly reconstructed. But the curvature at the center of the phase peaks is measurably different between the two models. Future experimental data can be comparted to these simulated results to further elucidate which model, the uniform skyrmion or the hopfion, better describes a dipole skyrmion in an Fe/Gd film.

By simulating a tomographic STEMH experiment of a uniform skyrmion and a hopfion, three distinctions between the two models have been identified: at zero tilt, the hopfion has a smaller phase peak amplitude; over small tilt angles, the curvature at the center of the phase peak of a uniform skyrmion is lower; at larger tilt angles, the peak-to-peak difference between the two lobes in the phase grows more relative to the initial amplitude in the hopfion model. Initial experimental measurements of dipole skyrmions suggest they are better fit by the hopfion model, but further investigation is needed. In addition to more experimental measurements of the phase through a dipole skyrmion at zero tilt, experimental STEMH measurements as the Fe/Gd film is tilted can be comparted to the simulated results for each model to demonstrate which is a better fit.

Conclusion

Tomographic STEMH, in concert with LTEM and SEMPA [112], can be used to confirm that “dipole skyrmions” in Fe/Gd films have the depth-dependent structure predicted by micromagnetic simulation [39]–[42], which has a non-zero Hopf index, indicating they are in fact hopfions. Tomographic STEMH reconstructions of a uniform skyrmion and a hopfion were simulated. Three distinct trends in the measured phase as the sample is tilted can distinguish between a hopfion and a standard uniform skyrmion,

though sufficiently fine probe size is required. One of those trends is a lower phase amplitude at zero tilt; most of the experimental STEMH measurements of dipole skyrmions in an Fe/Gd thin film presented in Chapter III agree with the hopfion model more closely, but there are some outliers. The cause of this variation is the subject of further investigation. By comparing experimental STEMH reconstructions of dipole skyrmions in an Fe/Gd film to the simulated reconstructions of the two models, it can be determined which is a better description. Confirming that Fe/Gd dipole skyrmions are in fact hopfions would constitute the first experimental observation of a magnetic hopfion. This experiment is also an example of a situation in which Lorentz TEM, which makes an indirect phase measurement, is not sensitive enough. STEMH, which measures the phase directly, is much more effective in addressing this question.

CHAPTER V

CONCLUSION AND FUTURE DIRECTIONS

Transmission electron microscopy is a powerful tool for studying micromagnetics. We used Lorentz TEM to study the evolution of the in-plane magnetic domains in a multilayer thin film composed of ferromagnetic and normal metal layers, revealing unexpected behavior and demonstrating the importance of combining nanomagnetic imaging techniques that can access different components of the material's magnetic structure. We then demonstrated the first application of diffraction-grating-based scanning TEM holography, a new probe-based phase measurement technique, to magnetic materials. Finally, we discussed how this technique could be used to confirm the first observation of a magnetic hopfion and presented initial results.

Topological magnetic domains like skyrmions and hopfions are of interest as information carriers in racetrack memory [2]–[4], [104]. The dynamics of these magnetic textures depends on their 3D structure, which has only recently been explored experimentally [116]–[118], [140], [153]. One way to do this is electron tomography using a direct phase measurement technique like off-axis electron holography or STEM holography. STEMH has fewer instrument requirements for implementation and is therefore more accessible. The small tilt series described in Chapter IV is the first step towards implementing scanning holographic vector field electron tomography.

In vector field electron tomography, the phase is measured at multiple tilt angles to reconstruct the 3D vector field [134], [136], [148]. However, a tilt along a single axis only allows the magnetic field along that axis to be reconstructed; two tilt series must be collected along two orthogonal axes. Additionally, to separate the electrostatic phase

from the magnetic phase, for each tilt series one must also collect a complementary tilt series with the sample flipped. For all four tilt series the images collected must be aligned. This technique adds a huge amount of experimental difficulty. However, that is not the main obstacle to implementing this tomographic reconstruction with STEM holography. As described in Chapter III, for each point in the scan the phase is calculated from a recorded image of the interference pattern formed by the probes, forming a 2D scan of 2D datasets. A typical STEMH measurement can therefore require a few hundred gigabytes of data. A full 3D tomographic reconstruction of a magnetic feature would require a 4D dataset for each angle, and the 3D resolution is determined by the number of discrete angles in the tilt series. The amount of memory required to store all of the raw data for a full 3D tomographic STEMH image could quickly become untenable. Currently the images are collected on TEAM I at the National Center for Electron Microscopy and then transferred to TALAPAS, University of Oregon's computing cluster, where the phase at each scan point is calculated. The bottleneck in this process is the memory limit of the TEAM I PC, which requires that all the data be moved intermittently. While this adds time to any STEMH experiment, this is particularly inconvenient for experiments requiring many images of the same sample region in which beam and sample drift are a concern. The second inconvenience of requiring a computing cluster to form the phase image is that the microscopist does not know the image they took until several days after it was recorded. Whereas HAADF can provide an image of electrostatic features and an LTEM image of the sample can be displayed immediately to help guide an imaging experiment, the success of a STEMH measurement currently cannot be known until days or weeks later.

To make STEMH a much more user-friendly technique, and in particular to implement scanning holographic vector field electron tomography, the phase calculation must be integrated into the image collection. Efforts are underway to implement edge computing architecture into the data acquisition process of next-generation TEMs. For instance, the 4D Camera, developed at Lawrence Berkeley National Lab for STEM experiments that require 4D datasets like STEMH, incorporates four field programmable gate arrays and sends the collected data directly to the National Energy Research Computing Center for additional analysis [162]–[164]. This would address the issue discussed above but the detector has 576x576 pixels rather than 1792x1920 pixels of the detector typically used for STEMH. To use the 4D Camera, we would need to use smaller probe-forming diffraction gratings so that the entire interference image could be recorded while also being able to discern the grating periodicity. However, this would worsen spatial resolution at the sample. The 4D Camera is not the perfect STEMH detector but shows how future detectors better suited to collecting 4D datasets are developing. Rather than still relying on a computing cluster to post-process the STEMH data, one could imagine an FPGA and/or GPU placed between the detector and host computer to extract the phase information from the raw interference images at each point in the scan, and only store the relevant data. Future iterations of the STEMH system will allow this highspeed data extraction to be robust. The work described in this dissertation has identified a new path and taken a first step along it.

REFERENCES CITED

[1] F. N. Rybakov, N. S. Kiselev, A. B. Borisov, L. Döring, C. Melcher, and S. Blügel, "Magnetic hopfions in solids," *arXiv:1904.00250 [cond-mat, physics:nlin]*, Mar. 2019.

[2] A. Fert, V. Cros, and J. Sampaio, "Skyrmions on the track," *Nat Nano*, vol. 8, no. 3, pp. 152–156, Mar. 2013.

[3] S. S. P. Parkin, M. Hayashi, and L. Thomas, "Magnetic Domain-Wall Racetrack Memory," *Science*, vol. 320, no. 5873, pp. 190–194, Apr. 2008.

[4] S. Parkin and S.-H. Yang, "Memory on the racetrack," *Nature Nanotechnology*, vol. 10, no. 3, pp. 195–198, Mar. 2015.

[5] W. Legrand *et al.*, "Hybrid chiral domain walls and skyrmions in magnetic multilayers," *Sci. Adv.*, vol. 4, no. 7, p. 0415, Jul. 2018.

[6] W. Van Winkle, "The death of disk? HDDs still have an important role to play," *VentureBeat*, Sep. 02, 2019.

[7] D. Reinsel, J. Gantz, and J. Rydning, "The Digitization of the World from Edge to Core," International Data Corporation, IDC White Paper US44413318, 2018.

[8] "The Growth in Connected IoT Devices Is Expected to Generate 79.4ZB of Data in 2025, According to a New IDC Forecast," *IDC Media Center*, Jun. 18, 2019. .

[9] Rainer W. Kaese, "Storage Trends 2019," *Toshiba Storage Solutions*. .

[10] M. D. Graef and Y. Zhu, *Magnetic imaging and its applications to materials*. Academic Press, 2001.

[11] R. Dunin-Borkowski *et al.*, "Opportunities for Chromatic Aberration Corrected High-Resolution Transmission Electron Microscopy, Lorentz Microscopy and Electron Holography of Magnetic Minerals," *Microscopy and Microanalysis*, vol. 18, no. S2, pp. 1708–1709, Jul. 2012.

[12] B. Freitag, M. Bischoff, H. Mueller, P. Hartel, and H. von Harrach, "Sub-nanometer Resolution in Field-free Imaging using a Titan 80-300 with Lorentz lens and Image Cs-Corrector at 300kV Acceleration Voltage," *Microscopy and Microanalysis*, vol. 15, no. S2, pp. 184–185, Jul. 2009.

[13] S. McVitie, D. McGrouther, S. McFadzean, D. A. MacLaren, K. J. O'Shea, and M. J. Benitez, "Aberration corrected Lorentz scanning transmission electron microscopy," *Ultramicroscopy*, vol. 152, pp. 57–62, May 2015.

[14] T. Nagai, K. Kimoto, K. Inoke, and M. Takeguchi, “Real-space observation of nanoscale magnetic phase separation in dysprosium by aberration-corrected Lorentz microscopy,” *Physical Review B*, vol. 96, no. 10, Sep. 2017.

[15] M. A. Schofield, M. Beleggia, Y. Zhu, and G. Pozzi, “Characterization of JEOL 2100F Lorentz-TEM for low-magnification electron holography and magnetic imaging,” *Ultramicroscopy*, vol. 108, no. 7, pp. 625–634, Jun. 2008.

[16] E. Snoeck *et al.*, “Off-Axial Aberration Correction using a B-COR for Lorentz and HREM Modes,” *Microscopy and Microanalysis*, vol. 20, no. S3, pp. 932–933, Aug. 2014.

[17] Y. Takahashi *et al.*, “Resolution Assessment of an Aberration Corrected 1.2-MV Field Emission Transmission Electron Microscope,” *Microscopy and Microanalysis*, vol. 21, no. S3, pp. 1865–1866, Aug. 2015.

[18] T. Tanigaki *et al.*, “Magnetic field observations in CoFeB/Ta layers with 0.67-nm resolution by electron holography,” *Scientific Reports*, vol. 7, no. 1, p. 16598, Dec. 2017.

[19] A. Hubert and R. Schäfer, *Magnetic domains: the analysis of magnetic microstructures*. Springer, 1998.

[20] H. Hopster and H. P. Oepen, *Magnetic Microscopy of Nanostructures*, 1st ed. Springer, 2004.

[21] R. Nisticò, F. Cesano, and F. Garello, “Magnetic Materials and Systems: Domain Structure Visualization and Other Characterization Techniques for the Application in the Materials Science and Biomedicine,” *Inorganics*, vol. 8, no. 1, p. 6, Jan. 2020.

[22] A. Lubk, D. Wolf, P. Simon, C. Wang, S. Sturm, and C. Felser, “Nanoscale three-dimensional reconstruction of electric and magnetic stray fields around nanowires,” *Appl. Phys. Lett.*, vol. 105, no. 17, p. 173110, Oct. 2014.

[23] M. Krajnak, D. McGrouther, D. Maneuski, V. O. Shea, and S. McVitie, “Pixelated detectors and improved efficiency for magnetic imaging in STEM differential phase contrast,” *Ultramicroscopy*, vol. 165, pp. 42–50, Jun. 2016.

[24] N. Shibata *et al.*, “Atomic resolution electron microscopy in a magnetic field free environment,” *Nature Communications*, vol. 10, no. 1, Dec. 2019.

[25] A. Tonomura, “Applications of electron holography,” *Rev. Mod. Phys.*, vol. 59, no. 3, pp. 639–669, Jul. 1987.

[26] H. Lichte, “Electron Image Plane Off-axis Holography of Atomic Structures,” in *Advances in Optical and Electron Microscopy*, vol. 12, Elsevier, 1991, pp. 25–91.

[27] E. Völkl, L. F. Allard, and D. C. Joy, *Introduction to Electron Holography*. Springer, 1999.

[28] Th. Leuthner, H. Lichte, and K.-H. Herrmann, "STEM-holography using the electron biprism," *phys. stat. sol. (a)*, vol. 116, no. 1, pp. 113–121, Nov. 1989.

[29] J. M. Cowley, "High resolution side-band holography with a STEM instrument," *Ultramicroscopy*, vol. 34, no. 4, pp. 293–297, Dec. 1990.

[30] Y. Takahashi, Y. Yajima, M. Ichikawa, and K. Kuroda, "Observation of Magnetic Induction Distribution by Scanning Interference Electron Microscopy," *Jpn. J. Appl. Phys.*, vol. 33, no. 9B, p. L1352, Sep. 1994.

[31] J. M. Cowley, "Ultra-high resolution with off-axis STEM holography," *Ultramicroscopy*, vol. 96, no. 2, pp. 163–166, Aug. 2003.

[32] F. S. Yasin, T. R. Harvey, J. J. Chess, J. S. Pierce, and B. J. McMorran, "Path-separated electron interferometry in a scanning transmission electron microscope," *J. Phys. D: Appl. Phys.*, vol. 51, no. 20, p. 205104, 2018.

[33] F. S. Yasin *et al.*, "Probing Light Atoms at Subnanometer Resolution: Realization of Scanning Transmission Electron Microscope Holography," *Nano Lett.*, vol. 18, no. 11, pp. 7118–7123, Nov. 2018.

[34] F. S. Yasin, K. Harada, D. Shindo, H. Shinada, B. J. McMorran, and T. Tanigaki, "A tunable path-separated electron interferometer with an amplitude-dividing grating beamsplitter," *Appl. Phys. Lett.*, vol. 113, no. 23, p. 233102, Dec. 2018.

[35] J. Lucassen *et al.*, "Stabilizing chiral spin structures via an alternating Dzyaloshinskii-Moriya interaction," *Physical Review B*, vol. 102, no. 1, Jul. 2020.

[36] I. Lemesh and G. S. D. Beach, "Walker Breakdown with a Twist: Dynamics of Multilayer Domain Walls and Skyrmions Driven by Spin-Orbit Torque," *Physical Review Applied*, vol. 12, no. 4, Oct. 2019.

[37] I. Lemesh and G. S. D. Beach, "Twisted domain walls and skyrmions in perpendicularly magnetized multilayers," *Physical Review B*, vol. 98, no. 10, Sep. 2018.

[38] J. J. Chess *et al.*, "Streamlined approach to mapping the magnetic induction of skyrmionic materials," *Ultramicroscopy*, vol. 177, pp. 78–83, Jun. 2017.

[39] S. A. Montoya *et al.*, "Resonant properties of dipole skyrmions in amorphous Fe/Gd multilayers," *Phys. Rev. B*, vol. 95, no. 22, p. 224405, Jun. 2017.

[40] S. A. Montoya *et al.*, "Tailoring magnetic energies to form dipole skyrmions and skyrmion lattices," *Physical Review B*, vol. 95, no. 2, p. 024415, Jan. 2017.

[41] S. A. Montoya, R. Tolley, I. Gilbert, S.-G. Je, M.-Y. Im, and E. E. Fullerton, “Spin-orbit torque induced dipole skyrmion motion at room temperature,” *Phys. Rev. B*, vol. 98, no. 10, p. 104432, Sep. 2018.

[42] R. D. Desautels *et al.*, “Realization of ordered magnetic skyrmions in thin films at ambient conditions,” *Phys. Rev. Materials*, vol. 3, no. 10, p. 104406, Oct. 2019.

[43] M. Knoll and E. Ruska, “Das Elektronenmikroskop,” *Zeitschrift für Physik*, vol. 78, no. 5–6, pp. 318–339, May 1932.

[44] E. Ruska, “The Development of the Electron Microscope and of Electron Microscopy (Nobel Lecture),” *Angewandte Chemie International Edition in English*, vol. 26, no. 7, pp. 595–605, Jul. 1987.

[45] D. Gabor, “A new microscopic principle,” *Nature*, vol. 161, no. 4098, p. 777, May 1948.

[46] A. V. Crewe, J. Wall, and J. Langmore, “Visibility of Single Atoms,” *Science*, vol. 168, no. 3937, pp. 1338–1340, Jun. 1970.

[47] R. S. Rai and S. Subramanian, “Role of transmission electron microscopy in the semiconductor industry for process development and failure analysis,” *Progress in Crystal Growth and Characterization of Materials*, vol. 55, no. 3–4, pp. 63–97, Sep. 2009.

[48] S. Prasad, V. Potdar, S. Cherian, P. Abraham, and A. Basu, “Transmission electron microscopy imaging of SARS-CoV-2,” *Indian Journal of Medical Research*,, 2020.

[49] M. E. Hale, H. W. Fuller, and H. Rubinstein, “Magnetic Domain Observations by Electron Microscopy,” *Journal of Applied Physics*, vol. 30, no. 5, pp. 789–791, May 1959.

[50] H. Boersch and H. Raith, “Elektronenmikroskopische Abbildung Weißscher Bezirke in dünnen ferromagnetischen Schichten,” *Die Naturwissenschaften*, vol. 46, no. 20, pp. 574–574, Oct. 1959.

[51] A. K. Petford-Long and J. N. Chapman, “Lorentz Microscopy,” in *Magnetic Microscopy of Nanostructures*, H. Hopster and H. P. Oepen, Eds. Berlin, Heidelberg: Springer Berlin Heidelberg, 2005, pp. 67–86.

[52] C. Phatak, A. K. Petford-Long, and M. De Graef, “Recent advances in Lorentz microscopy,” *Current Opinion in Solid State and Materials Science*, vol. 20, no. 2, pp. 107–114, Apr. 2016.

[53] M. De Graef and Y. Zhu, “Quantitative noninterferometric Lorentz microscopy,” *Journal of Applied Physics*, vol. 89, no. 11, pp. 7177–7179, Jun. 2001.

[54] K.-S. Ryu, L. Thomas, S.-H. Yang, and S. Parkin, “Chiral spin torque at magnetic domain walls,” *Nature Nanotech*, vol. 8, no. 7, pp. 527–533, Jul. 2013.

[55] S. Emori, U. Bauer, S.-M. Ahn, E. Martinez, and G. S. D. Beach, “Current-driven dynamics of chiral ferromagnetic domain walls,” *Nature Mater*, vol. 12, no. 7, pp. 611–616, Jul. 2013.

[56] A. Brataas, “Chiral domain walls move faster,” *Nature Nanotech*, vol. 8, no. 7, pp. 485–486, Jul. 2013.

[57] A. Soumyanarayanan, N. Reyren, A. Fert, and C. Panagopoulos, “Emergent phenomena induced by spin–orbit coupling at surfaces and interfaces,” *Nature*, vol. 539, no. 7630, pp. 509–517, Nov. 2016.

[58] G. Chen *et al.*, “Tailoring the chirality of magnetic domain walls by interface engineering,” *Nat Commun*, vol. 4, p. 2671, Oct. 2013.

[59] F. Bloch, “Zur Theorie des Ferromagnetismus,” *Z. Physik*, vol. 61, no. 3–4, pp. 206–219, Mar. 1930.

[60] L.D. Landau, “On The Theory Of The Dispersion Of Magnetic Permeability In Ferromagnetic Bodies,” in *Collected Papers of L.D. Landau*, Elsevier, 1965, pp. 101–114.

[61] W. Jiang, G. Chen, K. Liu, J. Zang, S. G. E. te Velthuis, and A. Hoffmann, “Skyrmions in magnetic multilayers,” *Physics Reports*, vol. 704, pp. 1–49, Aug. 2017.

[62] S. Mühlbauer *et al.*, “Skyrmion Lattice in a Chiral Magnet,” *Science*, vol. 323, no. 5916, pp. 915–919, Feb. 2009.

[63] I. Dzyaloshinsky, “A thermodynamic theory of ‘weak’ ferromagnetism of antiferromagnetics,” *Journal of Physics and Chemistry of Solids*, vol. 4, no. 4, pp. 241–255, Jan. 1958.

[64] T. Moriya, “Anisotropic Superexchange Interaction and Weak Ferromagnetism,” *Phys. Rev.*, vol. 120, no. 1, pp. 91–98, Oct. 1960.

[65] K. Shibata *et al.*, “Towards control of the size and helicity of skyrmions in helimagnetic alloys by spin-orbit coupling,” *Nat Nano*, vol. 8, no. 10, pp. 723–728, Oct. 2013.

[66] J. Lee, J. Yang, S. G. Kwon, and T. Hyeon, “Nonclassical nucleation and growth of inorganic nanoparticles,” *Nature Reviews Materials*, vol. 1, no. 8, p. 16034, Jun. 2016.

[67] J. Lau, private communication, 2012.

[68] Takeshi Kasama, Rafal Dunin-Borkowsky, and Marco Beleggia, private communication, 2012.

[69] P. Thevenaz, U. E. Ruttimann, and M. Unser, “A pyramid approach to subpixel registration based on intensity,” *IEEE Trans. on Image Process.*, vol. 7, no. 1, pp. 27–41, Jan. 1998.

[70] S. van der Walt *et al.*, “scikit-image: image processing in Python,” *PeerJ*, vol. 2, p. e453, Jun. 2014.

[71] The Astropy Collaboration *et al.*, “The Astropy Project: Building an inclusive, open-science project and status of the v2.0 core package,” *AJ*, vol. 156, no. 3, p. 123, Aug. 2018.

[72] The Astropy Collaboration *et al.*, “Astropy: A community Python package for astronomy,” *A&A*, vol. 558, p. A33, Oct. 2013.

[73] D. A. Kitchaev, I. J. Beyerlein, and A. Van der Ven, “Phenomenology of chiral Dzyaloshinskii-Moriya interactions in strained materials,” *Phys. Rev. B*, vol. 98, no. 21, p. 214414, Dec. 2018.

[74] Y. Shi and J. Wang, “Stabilizing skyrmions by nonuniform strain in ferromagnetic thin films without a magnetic field,” *Phys. Rev. B*, vol. 97, no. 22, p. 224428, Jun. 2018.

[75] J. C. McClure and K. Schroder, “The magnetic barkhausen effect,” *C R C Critical Reviews in Solid State Sciences*, vol. 6, no. 1, pp. 45–83, Jan. 1976.

[76] J. J. Chess, S. A. Montoya, E. E. Fullerton, and B. J. McMorran, “Determination of domain wall chirality using in situ Lorentz transmission electron microscopy,” *AIP Advances*, vol. 7, no. 5, p. 056807, Feb. 2017.

[77] B. Haas, D. Cooper, and J.-L. Rouvière, “Direct comparison of differential phase contrast and off-axis electron holography for the measurement of electric potentials by the examination of reverse biased Si p-n junctions and III-V samples,” in *European Microscopy Congress 2016: Proceedings*, Wiley-VCH Verlag GmbH & Co. KGaA, 2016.

[78] T. R. Harvey *et al.*, “Interpretable and Efficient Interferometric Contrast in Scanning Transmission Electron Microscopy with a Diffraction-Grating Beam Splitter,” *Phys. Rev. Applied*, vol. 10, no. 6, p. 061001, Dec. 2018.

[79] T. R. Harvey, J. S. Pierce, A. K. Agrawal, P. Ercius, M. Linck, and B. J. McMorran, “Efficient diffractive phase optics for electrons,” *New J. Phys.*, vol. 16, no. 9, p. 093039, Sep. 2014.

[80] J. S. Pierce, C. Wright, T. R. Harvey, and B. J. McMorran, “Creation of High Resolution Electron Diffraction Gratings using FIB and E-Beam Techniques,” in *EIPBN Proceedings*, Washington, DC, 2014, pp. P08-06.

[81] J. Pierce, “Holographic Sculpting of Electron Beams with Diffraction Gratings,” University of Oregon, 2019.

[82] C. W. Johnson, D. H. Bauer, and B. J. McMorran, “Improved control of electron computer-generated holographic grating groove profiles using ion beam gas-assisted etching,” *Appl. Opt.*, vol. 59, no. 6, pp. 1594–1601, Feb. 2020.

[83] F. Yasin, “Electron Interferometry Using an Amplitude Dividing Grating Beamsplitter: Development and Application,” 2019.

[84] C. W. Johnson *et al.*, “Exact design of complex amplitude holograms for producing arbitrary scalar fields,” *Opt. Express*, vol. 28, no. 12, pp. 17334–17346, Jun. 2020.

[85] H. D. Arnold and G. W. Elmen, “Permalloy, A New Magnetic Material of Very High Permeability,” *Bell System Technical Journal*, vol. 2, no. 3, pp. 101–111, Jul. 1923.

[86] R. D. Gomez, T. V. Luu, A. O. Pak, K. J. Kirk, and J. N. Chapman, “Domain configurations of nanostructured Permalloy elements,” *Journal of Applied Physics*, vol. 85, no. 8, pp. 6163–6165, Apr. 1999.

[87] K. Runge *et al.*, “High-resolution observation of magnetization processes in 2 μm × 2 μm × 0.04 μm permalloy particles,” *J. Appl. Phys.*, vol. 79, no. 8, p. 5075, 1996.

[88] H. H. Liu, X. K. Duan, R. C. Che, Z. F. Wang, and X. F. Duan, “In situ investigation of the magnetic domain wall in Permalloy thin film by Lorentz electron microscopy,” *Materials Letters*, vol. 62, no. 17–18, pp. 2654–2656, Jun. 2008.

[89] D. A. Tatarskiy, E. V. Skorokhodov, N. S. Gusev, V. Yu. Mikhailovskii, Yu. V. Petrov, and S. A. Gusev, “Lorentz transmission electron microscopy of ferromagnetic nanodisks,” Moscow, Russia, 2019, p. 020005.

[90] X. Fu, S. D. Pollard, B. Chen, B.-K. Yoo, H. Yang, and Y. Zhu, “Optical manipulation of magnetic vortices visualized in situ by Lorentz electron microscopy,” *Sci. Adv.*, vol. 4, no. 7, p. eaat3077, Jul. 2018.

[91] M. Möller, J. H. Gaida, S. Schäfer, and C. Ropers, “Few-nm tracking of current-driven magnetic vortex orbits using ultrafast Lorentz microscopy,” *Commun Phys*, vol. 3, no. 1, p. 36, Dec. 2020.

[92] W. Rave and A. Hubert, “Magnetic ground state of a thin-film element,” *IEEE Trans. Magn.*, vol. 36, no. 6, pp. 3886–3899, Nov. 2000.

[93] M. J. Donahue and D. G. Porter, “OOMMF User’s Guide, Version 1.0,” National Institute of Standards and Technology, Gaithersburg, MD, Interagency Report NISTIR 6376, Sep. 1999.

[94] M. Mansuripur, “Computation of electron diffraction patterns in Lorentz electron microscopy of thin magnetic films,” *Journal of Applied Physics*, vol. 69, no. 4, pp. 2455–2464, Feb. 1991.

[95] M. Beleggia, M. A. Schofield, Y. Zhu, M. Malac, Z. Liu, and M. Freeman, “Quantitative study of magnetic field distribution by electron holography and micromagnetic simulations,” *Applied Physics Letters*, vol. 83, no. 7, pp. 1435–1437, Aug. 2003.

[96] S. K. Walton, K. Zeissler, W. R. Branford, and S. Felton, “MALTS: A Tool to Simulate Lorentz Transmission Electron Microscopy From Micromagnetic Simulations,” *IEEE Transactions on Magnetics*, vol. 49, no. 8, pp. 4795–4800, Aug. 2013.

[97] N. Nagaosa and Y. Tokura, “Topological properties and dynamics of magnetic skyrmions,” *Nature Nanotechnology*, vol. 8, no. 12, pp. 899–911, Dec. 2013.

[98] Y. S. Lin, P. J. Grundy, and E. A. Giess, “Bubble domains in magnetostatically coupled garnet films,” *Applied Physics Letters*, vol. 23, no. 8, pp. 485–487, Oct. 1973.

[99] A. Malozemoff and J. Slonczewski, *Magnetic Domain Walls in Bubble Materials: Advances in Materials and Device Research*. Academic press, 1979.

[100] T. Garel and S. Doniach, “Phase transitions with spontaneous modulation-the dipolar Ising ferromagnet,” *Physical Review B*, vol. 26, no. 1, pp. 325–329, Jul. 1982.

[101] S. Takao, “A study of magnetization distribution of submicron bubbles in sputtered Ho-Co thin films,” *Journal of Magnetism and Magnetic Materials*, vol. 31–34, pp. 1009–1010, Feb. 1983.

[102] T. Okubo, S. Chung, and H. Kawamura, “Multiple- q States and the Skyrmion Lattice of the Triangular-Lattice Heisenberg Antiferromagnet under Magnetic Fields,” *Physical Review Letters*, vol. 108, no. 1, Jan. 2012.

[103] S. Heinze *et al.*, “Spontaneous atomic-scale magnetic skyrmion lattice in two dimensions,” *Nat Phys*, vol. 7, no. 9, pp. 713–718, Sep. 2011.

[104] B. Göbel, C. A. Akosa, G. Tatara, and I. Mertig, “Topological Hall signatures of magnetic hopfions,” *Phys. Rev. Research*, vol. 2, no. 1, p. 013315, Mar. 2020.

[105] I. L. Bogolubsky, “Three-dimensional topological solitons in the lattice model of a magnet with competing interactions,” *Physics Letters A*, vol. 126, no. 8–9, pp. 511–514, Jan. 1988.

[106] P. Sutcliffe, “Skyrmion Knots in Frustrated Magnets,” *Physical Review Letters*, vol. 118, no. 24, Jun. 2017.

[107] Y. Liu, R. K. Lake, and J. Zang, “Binding a hopfion in a chiral magnet nanodisk,” *Physical Review B*, vol. 98, no. 17, Nov. 2018.

[108] J.-S. B. Tai and I. I. Smalyukh, “Static Hopf Solitons and Knotted Emergent Fields in Solid-State Noncentrosymmetric Magnetic Nanostructures,” *Physical Review Letters*, vol. 121, no. 18, Oct. 2018.

[109] X. S. Wang, A. Qaiumzadeh, and A. Brataas, “Current-Driven Dynamics of Magnetic Hopfions,” *Physical Review Letters*, vol. 123, no. 14, Sep. 2019.

[110] Y. Liu, W. Hou, X. Han, and J. Zang, “Three-Dimensional Dynamics of a Magnetic Hopfion Driven by Spin Transfer Torque,” *Physical Review Letters*, vol. 124, no. 12, Mar. 2020.

[111] J. H. C. Whitehead, “An Expression of Hopf’s Invariant as an Integral,” *Proceedings of the National Academy of Sciences*, vol. 33, no. 5, pp. 117–123, May 1947.

[112] J. J. Chess, “Mapping Topological Magnetization and Magnetic Skyrmions,” University of Oregon, University of Oregon, Eugene, Oregon, 2017.

[113] D. Crowley and M. Grant, “The Poincaré–Hopf Theorem for line fields revisited,” *Journal of Geometry and Physics*, vol. 117, pp. 187–196, Jul. 2017.

[114] M. Ezawa, “Topological semimetals carrying arbitrary Hopf numbers: Fermi surface topologies of a Hopf link, Solomon’s knot, trefoil knot, and other linked nodal varieties,” *Physical Review B*, vol. 96, no. 4, Jul. 2017.

[115] E. Harikumar, I. Mitra, and H. S. Sharatchandra, “Half-monopoles and half-vortices in the Yang–Mills theory,” *Physics Letters B*, vol. 557, no. 3–4, pp. 303–308, Apr. 2003.

[116] S. Zhang *et al.*, “Reciprocal space tomography of 3D skyrmion lattice order in a chiral magnet,” *Proc Natl Acad Sci USA*, vol. 115, no. 25, pp. 6386–6391, Jun. 2018.

[117] S. L. Zhang, G. van der Laan, W. W. Wang, A. A. Haghighirad, and T. Hesjedal, “Direct Observation of Twisted Surface skyrmions in Bulk Crystals,” *Phys. Rev. Lett.*, vol. 120, no. 22, p. 227202, May 2018.

[118] S. Zhang *et al.*, “Robust Perpendicular Skyrmions and Their Surface Confinement,” *Nano Lett.*, vol. 20, no. 2, pp. 1428–1432, Feb. 2020.

[119] J. Unguris, “6. Scanning electron microscopy with polarization analysis (SEMPA) and its applications,” in *Experimental Methods in the Physical Sciences*, vol. 36, M. De Graef and Y. Zhu, Eds. Academic Press, 2001, pp. 167–XVI.

[120] J. Radon, “Über die Bestimmung von Funktionen durch ihre Integralwerte längs gewisserMannigfaltigkeiten,” *Ber. Verh. Sächs. Akad. Wiss. Leipzig. Math. Nat. Kl.*, vol. 69, pp. 262–277, Apr. 1917.

[121] A. Lange, M. P. Hentschel, and A. Kupsch, “Computertomographische Rekonstruktion mit DIRECTT: 2D-Modellrechnungen im Vergleich zur gefilterten Rückprojektion,” *MP*, vol. 50, no. 5, pp. 272–277, May 2008.

[122] A. Hilger, I. Manke, N. Kardjilov, M. Osenberg, H. Markötter, and J. Banhart, “Tensorial neutron tomography of three-dimensional magnetic vector fields in bulk materials,” *Nat Commun*, vol. 9, no. 1, p. 4023, Dec. 2018.

[123] I. Manke *et al.*, “Three-dimensional imaging of magnetic domains,” *Nat Commun*, vol. 1, no. 1, p. 125, Dec. 2010.

[124] K. L. Hasezaki *et al.*, “Three-dimensional visualization of dislocations in a ferromagnetic material by magnetic-field-free electron tomography,” *Ultramicroscopy*, vol. 182, pp. 249–257, Nov. 2017.

[125] C. Donnelly and V. Scagnoli, “Imaging three-dimensional magnetic systems with x-rays,” *J. Phys.: Condens. Matter*, vol. 32, no. 21, p. 213001, May 2020.

[126] C. Donnelly *et al.*, “Time-resolved imaging of three-dimensional nanoscale magnetization dynamics,” *Nat. Nanotechnol.*, vol. 15, no. 5, pp. 356–360, May 2020.

[127] C. Donnelly *et al.*, “Tomographic reconstruction of a three-dimensional magnetization vector field,” *New J. Phys.*, vol. 20, no. 8, p. 083009, Aug. 2018.

[128] C. Donnelly *et al.*, “Three-dimensional magnetization structures revealed with X-ray vector nanotomography,” *Nature*, vol. 547, no. 7663, pp. 328–331, Jul. 2017.

[129] M. Suzuki *et al.*, “Three-dimensional visualization of magnetic domain structure with strong uniaxial anisotropy via scanning hard X-ray microtomography,” *Appl. Phys. Express*, vol. 11, no. 3, p. 036601, Mar. 2018.

[130] R. Streubel, F. Kronast, P. Fischer, D. Parkinson, O. G. Schmidt, and D. Makarov, “Retrieving spin textures on curved magnetic thin films with full-field soft X-ray microscopies,” *Nat Commun*, vol. 6, no. 1, p. 7612, Nov. 2015.

[131] A. Hierro-Rodriguez *et al.*, “3D reconstruction of magnetization from dichroic soft X-ray transmission tomography,” *J Synchrotron Rad*, vol. 25, no. 4, pp. 1144–1152, Jul. 2018.

[132] T. Tanigaki *et al.*, “Three-Dimensional Observation of Magnetic Vortex Cores in Stacked Ferromagnetic Discs,” *Nano Lett.*, vol. 15, no. 2, pp. 1309–1314, Feb. 2015.

[133] D. Shindo and Z. Akase, “Direct observation of electric and magnetic fields of functional materials,” *Materials Science and Engineering: R: Reports*, vol. 142, p. 100564, Oct. 2020.

[134] D. Wolf *et al.*, “3D Magnetic Induction Maps of Nanoscale Materials Revealed by Electron Holographic Tomography,” *Chem. Mater.*, vol. 27, no. 19, pp. 6771–6778, Oct. 2015.

[135] D. Wolf *et al.*, “Holographic vector field electron tomography of three-dimensional nanomagnets,” *Commun Phys*, vol. 2, no. 1, p. 87, Dec. 2019.

[136] G. Lai, T. Hirayama, A. Fukuhara, K. Ishizuka, T. Tanji, and A. Tonomura, “Three-dimensional reconstruction of magnetic vector fields using electron-holographic interferometry,” *Journal of Applied Physics*, vol. 75, no. 9, pp. 4593–4598, May 1994.

[137] P. Simon *et al.*, “Synthesis and Three-Dimensional Magnetic Field Mapping of Co_2FeGa Heusler Nanowires at 5 nm Resolution,” *Nano Lett.*, vol. 16, no. 1, pp. 114–120, Jan. 2016.

[138] R. Tsuneta, H. Kashima, T. Iwane, K. Harada, and M. Koguchi, “Dual-axis 360° rotation specimen holder for analysis of three-dimensional magnetic structures,” *Microscopy (Tokyo)*, vol. 63, no. 6, pp. 469–473, Dec. 2014.

[139] C. Phatak, A. K. Petford-Long, and M. De Graef, “Three-Dimensional Study of the Vector Potential of Magnetic Structures,” *Phys. Rev. Lett.*, vol. 104, no. 25, p. 253901, Jun. 2010.

[140] S. Schneider *et al.*, “Induction Mapping of the 3D-Modulated Spin Texture of Skyrmions in Thin Helimagnets,” *Phys. Rev. Lett.*, vol. 120, no. 21, p. 217201, May 2018.

[141] K. A. Mohan, P. Kc, C. Phatak, M. De Graef, and C. A. Bouman, “Model-Based Iterative Reconstruction of Magnetization Using Vector Field Electron Tomography,” *IEEE Trans. Comput. Imaging*, vol. 4, no. 3, pp. 432–446, Sep. 2018.

[142] K. C. Prabhat, K. Aditya Mohan, C. Phatak, C. Bouman, and M. De Graef, “3D reconstruction of the magnetic vector potential using model based iterative reconstruction,” *Ultramicroscopy*, vol. 182, pp. 131–144, Nov. 2017.

[143] R. P. Ferrier, S. McVitie, A. Gallagher, and W. A. P. Nicholson, “Characterisation of MFM tip fields by electron tomography,” *IEEE Trans. Magn.*, vol. 33, no. 5, pp. 4062–4064, Sep. 1997.

[144] J. Scott, S. McVitie, R. P. Ferrier, and A. Gallagher, “Electrostatic charging artefacts in Lorentz electron tomography of MFM tip stray fields,” *J. Phys. D: Appl. Phys.*, vol. 34, no. 9, pp. 1326–1332, May 2001.

[145] J. Scott *et al.*, "Characterisation of FeBSiC coated MFM tips using Lorentz electron tomography and MFM," *IEEE Trans. Magn.*, vol. 35, no. 5, pp. 3986–3988, Sep. 1999.

[146] S. McVitie, R. P. Ferrier, J. Scott, G. S. White, and A. Gallagher, "Quantitative field measurements from magnetic force microscope tips and comparison with point and extended charge models," *Journal of Applied Physics*, vol. 89, no. 7, pp. 3656–3661, Apr. 2001.

[147] S. J. Lade, D. Paganin, and M. J. Morgan, "Electron tomography of electromagnetic fields, potentials and sources," *Optics Communications*, vol. 253, no. 4–6, pp. 392–400, Sep. 2005.

[148] C. Phatak, M. Beleggia, and M. De Graef, "Vector field electron tomography of magnetic materials: Theoretical development," *Ultramicroscopy*, vol. 108, no. 6, pp. 503–513, May 2008.

[149] R. P. Yu, M. J. Morgan, and D. M. Paganin, "Lorentz-electron vector tomography using two and three orthogonal tilt series," *Physical Review A*, vol. 83, no. 2, p. 023813, Feb. 2011.

[150] Z. D. C. Kemp, T. C. Petersen, D. M. Paganin, K. M. Spiers, M. Weyland, and M. J. Morgan, "Analysis of noise-induced errors in vector-field electron tomography," *Phys. Rev. A*, vol. 90, no. 2, p. 023859, Aug. 2014.

[151] C. Phatak and D. Gürsoy, "Iterative reconstruction of magnetic induction using Lorentz transmission electron tomography," *Ultramicroscopy*, vol. 150, pp. 54–64, Mar. 2015.

[152] Z. D. C. Kemp, D. M. Paganin, T. C. Petersen, and M. J. Morgan, "Effect of specimen orientation on the accuracy of vector field electron tomography," *Opt. Express*, vol. 24, no. 20, p. 22366, Oct. 2016.

[153] H. S. Park *et al.*, "Observation of the magnetic flux and three-dimensional structure of skyrmion lattices by electron holography," *Nat Nano*, vol. 9, no. 5, pp. 337–342, May 2014.

[154] M. J. Benitez *et al.*, "Magnetic microscopy and topological stability of homochiral Néel domain walls in a Pt/Co/AlOx trilayer," *Nat Commun*, vol. 6, no. 1, p. 8957, Dec. 2015.

[155] S. McVitie and M. Cushley, "Quantitative Fresnel Lorentz microscopy and the transport of intensity equation," *Ultramicroscopy*, vol. 106, no. 4–5, pp. 423–431, Mar. 2006.

[156] M. S. Bronsgeest, J. E. Barth, L. W. Swanson, and P. Kruit, “Probe current, probe size, and the practical brightness for probe forming systems,” *Journal of Vacuum Science & Technology B: Microelectronics and Nanometer Structures*, vol. 26, no. 3, p. 949, 2008.

[157] R. S. Ruskin, Z. Yu, and N. Grigorieff, “Quantitative characterization of electron detectors for transmission electron microscopy,” *Journal of Structural Biology*, vol. 184, no. 3, pp. 385–393, Dec. 2013.

[158] *OpenChemistry/stempy*. Open Chemistry, 2020.

[159] T. Ursell, “Generate Random Numbers from a 2D Discrete Distribution,” *MATLAB Central File Echange*, 2020.

[160] P. Romano, “Generate Random Numbers from a 2D Discrete Distribution,” *Github*, 2017.

[161] SciPy 1.0 Contributors *et al.*, “SciPy 1.0: fundamental algorithms for scientific computing in Python,” *Nat Methods*, vol. 17, no. 3, pp. 261–272, Mar. 2020.

[162] I. J. Johnson *et al.*, “A Next Generation Electron Microscopy Detector Aimed at Enabling New Scanning Diffraction Techniques and Online Data Reconstruction,” *Microsc Microanal*, vol. 24, no. S1, pp. 166–167, Aug. 2018.

[163] J. Ciston *et al.*, “The 4D Camera: Very High Speed Electron Counting for 4D-STEM,” *Microsc Microanal*, vol. 25, no. S2, pp. 1930–1931, Aug. 2019.

[164] P. Ercius *et al.*, “The 4D Camera – a 87 kHz Frame-rate Detector for Counted 4D-STEM Experiments,” *Microscopy and Microanalysis*, pp. 1–3, Aug. 2020.